Max-Planck-Institut
für Plasmaphysik

Free-boundary extension of the SIESTA code and its application to the Wendelstein 7-X stellarator

Hugo A. Peraza Rodriguez

a dissertation presented to
Universidad Carlos III de Madrid
in candidacy for the degree
of Doctor of Philosophy

Recommended for acceptance
by the Department of Physics

Advisor: Prof. Dr. Raul Sanchez Fernandez

Co-Advisors: Dr. Joachim Geiger
Dr. Jose M Reynolds-Barredo
Promotor: Prof. Dr. Jean-Marie Noterdaeme

Leganés, September 2017

Doctoral Thesis:

Free-boundary extension of the SIESTA code and its application to the Wendelstein 7-X stellarator

Author:
Hugo A. Peraza Rodriguez

Advisor: Prof. Dr. Raul Sanchez Fernandez

Co-Advisors: Dr. Joachim Geiger
Dr. Jose M Reynolds-Barredo
Promotor: Prof. Dr. Jean-Marie Noterdaeme

Department of Physics
Universidad Carlos III de Madrid

Leganés, September 2017

Doctoral Thesis

Free-boundary extension of the SIESTA code and its application to the Wendelstein 7-X stellarator

Author:
Hugo A. Peraza Rodriguez

Advisor: Prof. Dr. Raul Sanchez Fernandez

Co-Advisors: Dr. Joachim Geiger
Dr. Jose M Reynolds-Barredo
Promotor: Prof. Dr. Jean-Marie Noterdaeme

Signature of Evaluating Committee

President: _____ _____

Vocal: _____ _____

Secretary: _____ _____

Leganés, ___ of _____, _____

Abstract

Ideal magnetohydrodynamics (MHD) codes are of utmost importance to analyse equilibria of different experiments. The well known VMEC code (Variational Moments Equilibrium Code)[52,53,56] does the three-dimensional ideal MHD analysis assuming nested magnetic surfaces. SIESTA (Scalable Iterative Equilibrium Solver for Toroidal Applications)[54] is a code that takes a step further than VMEC, relying on VMEC's solution, it computes the ideal MHD equilibrium solution of a given problem, without the assumption of nested magnetic surfaces. This results in the possible development of magnetic islands and stochastic regions. SIESTA, as was originally conceived, has a limiting aspect: it would only solve the equilibrium inside of the last closed flux surface (LCFS) found by VMEC. This condition implies that the results obtained for equilibria where there are possible instabilities or perturbations close to the LCFS are not well computed since SIESTA leaves the LCFS untouched.

In this work a free-plasma-boundary version of SIESTA is developed in order to overcome this original limitation. The approach used consists of extending the analysis domain given by VMEC, in such a way that the vacuum region, or at least the most important part of it, is within the analysis volume of SIESTA. This requires the extension of the numerical analysis mesh guaranteeing the continuity of the metric elements on the mesh; a good approximation of the magnetic field solution in all the volume, and a pressure solution which couples with the magnetic field.

The new version of SIESTA is applied to the specific case of the Wendelstein 7-X stellarator, at the IPP Greifswald (Germany), making comparisons with previous studies of equilibria showing the development of neoclassical bootstrap currents which cause the divertor island chain to shift its position. The previous studies were carried out with the VMEC-EXTENDER code combination, which is the general tool for ideal MHD equilibrium studies used in IPP. While their method is not self consistent, in the sense that it is a combination of the results of two different codes, it has shown to be correct for the vacuum case and has been tested to be close to the experiment*.

*This has been done by comparing the images of the magnetic islands detected in the device[66].

Resumen

Los códigos de magnetohidrodinámica (MHD) ideal son de primordial importancia para realizar análisis de equilibrios de diferentes experimentos de fusión nuclear. El código VMEC (Variational Moments Equilibrium Code)[52,53,56], bien conocido en la comunidad de investigadores en física de plasmas, realiza análisis tri-dimensionales de equilibrios de MHD ideal asumiendo superficies magnéticas anidadas. SIESTA (Scalable Iterative Equilibrium Solver for Toroidal Applications)[54] es un código que va un paso más allá que VMEC, respaldándose en la solución de VMEC, SIESTA calcula la solución de equilibrio de MHD ideal para un problema dado, sin la suposición de superficies magnéticas anidadas. Esto resulta en el posible desarrollo de islas magnéticas y regiones estocásticas. SIESTA, en su versión original, posee un aspecto limitante: solo podía resolver el equilibrio dentro de la última superficie cerrada (LCFS, por sus siglas en inglés) encontrada por VMEC. Esta condición implica que los resultados obtenidos para equilibrios donde pueden existir inestabilidades o perturbaciones cerca de la LCFS no están bien calculados debido a que SIESTA no modifica la LCFS.

En este trabajo se desarrolla una versión de SIESTA con frontera de plasma libre para sobrepasar esta limitación original. El planteamiento consiste en extender el dominio de análisis dado por VMEC, de modo tal que la región de vacío —o al menos la parte más importante de ella— se encuentre dentro del volumen de análisis de SIESTA. Esto requiere la extensión de la malla de análisis numérico garantizando la continuidad de los elementos métricos de la mala; una buena aproximación del campo magnético en todo el volumen, y una solución de la presion que se acople a el campo magnético.

La nueva versión de SIESTA se aplica al caso específico del stellerator Wendelstein 7-X , en el IPP de Greifswald (Alemania), realizando comparaciones con estudios previos de equilibrios que muestran el desarrollo de corrientes neoclásicas bootstrap, las cuales causan que la cadena de islas magnéticas asociadas al divertor cambien su posición. Los estudios previos se realizaron con la combinación de códigos VMEC-EXTENDER, que es la herramienta general utilizada en el IPP Greifswald para estudios de equilibrios de MHD ideal. Si bien es cierto que su método no es auto-consistente, en cuanto a que es la combinación de los resultados de dos códigos diferentes, ha demostrado ser válido para el caso de vacío y se ha comprobado su aproximación a los resultados experimentales[†].

[†] Esto se ha realizado comparando las imágenes de las islas magnéticas detectadas en el dispositivo [66].

Overzicht

Ideale Magnetohydrodynamische (MHD) codes zijn enorm belangrijk voor de anlayse van evenwichten van verschillende experimenten. De bekende VMEC code[52,53,56] doet de driedimensionale ideale MHD analyse, gebruik makende van de aanname van in elkaar passende fluxoppervlakken. SIESTA (Scalable Iterative Equilibrium Solver for Toroidal Applications)[54] is een code die een stap verder dan VMEC neemt. De code berekent het ideale MHD evennwicht zonder deze aanname van in elkaar passende fluxoppervlakken, startende van de oplossing van VMEC. Een resultaat hiervan is de mogelijke ontwikkeling van magnetische eilanden en stochastische regio's. SIESTA, volgens het oorspronkelijke ontwerp, had echter één limitatie: De code loste enkel evenwichten op binnen het laatste gesloten fluxoppervlak ('Last Closed Flux Surface', LCFS), bepaald door VMEC. Deze voorwaarde heeft als gevolg dat de resultaten voor evenwichten met mogelijke instabiliteiten dicht bij de LCFS niet goed berekend worden aangezien SIESTA de LCFS niet kan verplaatsen.

In dit werk werd een vrije plasmawand versie van SIESTA ontwikkeld om deze limitatie te overkomen. Deze strategie die we hier gebruiken bestaat uit het uitbreiden van het analysedomein van VMEC, zodat de vacuumregio, of op zijn minst het belangrijke deel ervan, binnen het analysisvolume van SIESTA valt. Hiervoor was het nodig om het analysemaas uit te breiden om de continuiteit van de metrische elementen te garanderen en om een goede benadering van het de oplossing van het magnetische veld in het volume te bekomen, alsook voor de druk die gekoppeld is met die van het magnetische veld.

Deze nieuwe versie van SIESTA werd dan toegepast op een specifieke configuratie van de Wendelstein 7-X stellarator, gesitueerd aan het IPP Greifswald, om te kunnen vergelijken met een vorige studie. Bij deze studie werd de ontwikkeling van de 'bootstrap' stromen zichtbaar, die ervoor zorgen dat het de divertoreilandsketen van positie verschuift. Ze was uitgevoerd met de VMEC-EXTENDER codecombinatie, die een algemeen gereedschap is voor ideale MHD evenwichtsstudies. Hoewel hun methode niet zelf consistent is, waarbij bedoeld wordt dat het een combinatie is van resultaten van twee verschillende codes, werd nu aangetoond dat het toch correct is voor het vauumgeval, en dicht bij experimentele waarnemimgen ligt. [‡].

[‡]Dit werd gedaan door de vergelijking met de afbeeldingen van de experimentele resultaten van de magnetische eilanddetectie in de machine[66].

Contents

A mi querida familia.

Acknowledgments

First of all, I would like to thank my supervisors, Raúl, Joachim and José Miguel, and also Víctor, without all of you this work would not have been possible, you have guided me through unknown lands to me (and sometimes to you too) and have made the whole experience of the doctorate very enjoyable. Thank you for all your patience and the great amount of time you have invested in me. I could not have been luckier with other supervisors, it's been an honour learning from you. I would also like to thank the coordinating staff, especially Ramón and Prof. Noterdaeme, thanks to your hard work the program works great. Thanks also to Prof. Helander for welcoming me in his group at IPP Greifswald and for pointing me to some great sources. º I would also like to thank the staff at the Physics Department at Universidad Carlos III de Madrid for making the environment in the department so enjoyable. I would especially like to thank the doctoral colleagues (to which José Miguel and Andrés are an addendum) for making these past years easier to handle by having fun times after and during work as well. We all may have turned a bit crazier during these years, but I'm sure it'd be worse if we hadn't had each other. My stays at the IPP Greifswald were also very enjoyable, all thanks to the nice people around there, always open for discussions —whether work related or not—, thank you all for being so hospitable, especially the people at the Stellarator Theory group.

Special thanks go to those who during these past years have been great friends, new and old, without regards to distance. I have met great people during my time in Europe, people who have been very helpful, welcoming and fun. Thank you for opening the doors to your homes for me, for offering me you help when I needed it, for sharing trips to the mountains, for stargazing at my side, for the shared dances, for sharing your favourite music, for sharing your climbing secrets with me, for the long talks and the short ones too, for showing me your home towns, for sharing amazing trips, dinners and parties together, for sharing your time with me. I could not have made it through these years if it weren't for all of you. A special unicorny thanks to Maša, my flatmate, but more than that my sister from another mother, thanks for being you!

Finalmente quisiera dar gracias infinitas a mi familia. Sin ustedes no estaría donde estoy. Gracias por creer en mí, por los sacrificios que han hecho por mí, por tanta dedicación, por tantos buenos momentos y por apoyarme en los malos momentos. Y también a Annemarie, mein Ein und Alles. Thanks for always being there for me and for making everything better with just a smile. Ich möchte auch ihrer Familie danken, dass sie mich als Teil ihrer Familie aufgenommen hat.

Gracias! Danke! Thank you! Grazie! Hvala! Gràcies!
Merci! Mersi! Bedankt! Blagodarya! Děkuji! Pura Vida!

This project was financed by the Universidad Carlos III de Madrid and was developed in collaboration with the Stellarator Theory Division of the Max Planck Institute for Plasma Physics, in Greifswald. This work has been carried out with support of FuseNet – the European Fusion Education Network – within the framework of the EUROfusion Consortium (www.fusenet.eu)

Part I

Background

1 Introduction

Energy is the most precious thing for humanity. Energy is required to run our computers, to light up our homes, to heat us up when it's cold and cool us down when it's warm. It has been proven in many studies that our main sources of energy at the moment (i.e. fossil fuels), are of detriment to our environment and our own health [26,27,38,78,90]. There are many initiatives to reduce fossil fuels dependency and to introduce clean energy sources but the demand of energy keeps increasing at a high pace and the renewable energy sources are just not enough to satisfy the demand of energy. Renewable energies also have the drawback that they are dependant on the meteorological conditions of different locations, which means these can only be produced when the weather or geology allows. Wind, photo-voltaic (solar), hydroelectric power, geothermal and tidal waves' power all depend on how the weather behaves or on the geology of the place where power plants are installed. Having so many different sources one would think that there should be no problem when it comes to the amount of energy produced, nevertheless, the intermittency of the energy flux would be problematic for the stability present day electrical networks. Here the matter of energy storage would improve a lot the functionality of renewables, but to this day there is no technology which is able to store the amount of energy on which entire cities can rely, and even if there were the intermittency could also have a huge impact on the storage units [61].

Nuclear fission energy is a great alternative to fossil fuels because of its high energy density, the abundance of Uranium and the cheapness of the produced energy. While having several pros, nuclear fission also carries with it high risks of radioactive contamination of the environment — causing great catastrophes like those already seen in Chernobyl [105] and in Fukushima [11,14,18] — and produces nuclear waste, the radioactivity of which decays at safe levels only after thousands of years.

The average and the peak power are generally strongly deviated, up to a factor 6 peak being higher than average.

1.1 Nuclear Fusion

Along with all these options, nuclear fusion forms part of the cocktail of different clean energy sources that would be able to fulfil the high energy demand of the future. The basic principle of fusion is the same that lights up the stars: having two light atoms, make them fuse together by making them collide at such a high energy that they overcome the electric repulsion that would otherwise repel them. Clearly, the technical challenge of making them collide at such high energies is not simple to solve.

In principle any light element can be used as fuel for fusion power, as long as it is given enough energy to overcome the electrostatic repulsion. Nevertheless, the lighter the nuclei the easier it is to achieve fusion and the least energy needs to be given in to achieve fusion. The fuel chosen for fusion experiments, and one day fusion power plants, is Hydrogen. Two isotopes in particular are chosen because of the higher cross section of their fusion reaction: Deuterium and Tritium. The reaction between these two nuclei is

$$ {}^{2}_{1}H + {}^{3}_{1}H \rightarrow {}^{4}_{2}He(3.5\text{MeV}) + {}^{1}_{0}\text{n}(14.1\text{MeV}) $$

where the excess energy takes the form of kinetic energy distributed in the neutron and the alpha particle (ionised Helium nucleus). The alpha particles will transmit their energy to the plasma through collisions, given that they are so heavy, heating the plasma in this way. The neutron, with a mass similar to protons, will most probably escape the plasma: it could only interact through a collision and the probability of that happening is not high.

When the energy produced is enough to sustain the fusion reaction of plasma, i.e. to heat up the rest of the plasma, then it is said that *ignition* is achieved. Basically this means that the power given off by the alpha particles to the plasma is enough to overcome the energy losses (radiated energy and energy transported through different mechanisms). This sets a condition which defines the minimum requirements for ignition, which is known as the Lawson criterion[64]:

$$ n\tau_E T > 3 \times 10^{21}\text{m}^{-3}\text{keVs} \tag{1.1} $$

where τ_E is the confinement time, which is the ratio between energy density of the plasma and power loss density (caused by heating transport)

$$ \tau_E = \frac{W}{P_{loss}} \quad ; $$

For elements heavier than iron (Z=56) it is harder to reach the process and it also becomes senseless because the energy balance of the reaction is negative.

Transport could be direct transport of particles leaving the plasma, but also transport of energy through the plasma through diffusion or through turbulent mechanisms.

T the temperature of the plasma and n its density. The temperature is fixed by the choice of elements, for the case of the D-T reaction the most efficient region is between 50–100 keV. Therefore, this condition sets a minimum limit on time and density so that the power produced by the fusion reaction overcomes the power losses.

The fusion reaction can be achieved by different means. The way our sun produces nuclear fusion is called inertial confinement. Basically, gravity pulls the atoms together so tight that the gravitational pressure warms up the nuclei, creating huge plasma which is capable of fusing, where particles do not escape, i.e. they keep the fusion happening by heating up the confined plasma. This principle can of course not be used on Earth. There is, nevertheless, a design of a nuclear reactor experiment which is based on the principle of creating very high pressure on the fuel gas, as to produce the same effect that happens in stars. The most important working experiment of this design is the National Ignition Facility (NIF), at the Lawrence Livermore National Laboratory, California, USA. The pressure that heats up the nuclei is not provided through gravitational pull but via an enormous laser array. The idea is that several high power lasers converge in a single point, generally at the centre of a sphere, where a fuel pellet lies. The energy provided by the laser is high enough to ablate material from the surface of the fuel pellet so rapidly that the repulsion compresses the rest and heats it up to create a hot and dense plasma so that fusion can occur.

NIF is one of the few experiments which has been able to achieve fusion. It was reported that they were able to produce the same amount of energy as was initially put in the system[74], but it has fallen short from the ignition point[8].Besides NIF, there are the Laser MegaJoule project in France, and the EU project HiPER.

1.2 Magnetic Confinement Fusion

A more widespread approach to fusion power generation, is the magnetic confinement. The idea is that since fusion plasmas need to be at very high temperatures, it is possible to take advantage of the fact that a plasma is a charged gas and to control it by means of magnetic fields, often compared to creating a "magnetic bottle". While the plasma is kept in the magnetic trap, it can be heated up through different methods (mainly using microwaves) to the point where such a high temperature is reached that collisions will take place at energies which will overcome the electric repulsion and confine the plasma long enough.

The principle of magnetic confinement devices is quite simple. The use of a magnetic trap is a quite straightforward approach since the most logical method to control charged particles is to apply electric and magnetic fields to them. Within magnetic confinement fusion there have been several designs for the experiments. The initial ones were the Z- and Θ-pinches —both linear devices— which proved to be very unstable in sustaining a plasma long enough for it to reach fusion conditions since linear devices with a finite length suffer additionally from so-called end-losses as such

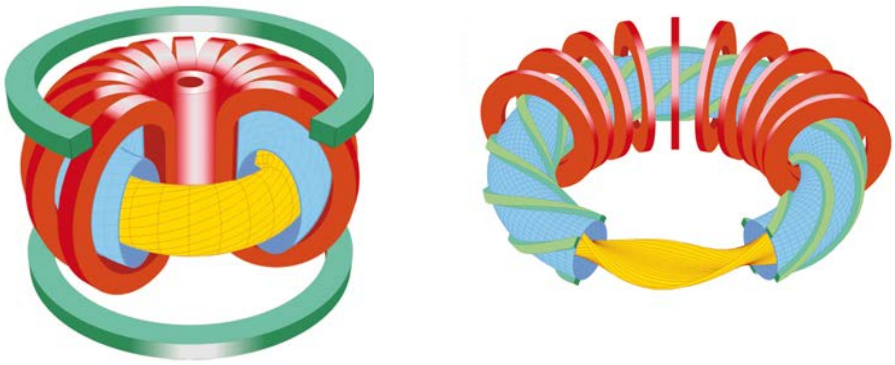

(a) Tokamak design

(b) Stellarator design

Figure 1.1: Comparison between tokamak (on the left) and stellarator designs (on the right). On both plots the blue surface depicts the vacuum vessel, the yellow volume represents the contained plasma and the red ``rings'' represent the toroidal field coils. Apart from this, for the Tokamak 1.1a, the green rings on the upper and the lower parts represent the vertical field coils and the pink cylinder in the center is the Ohmic transformer used to set the currents in the plasma. In the case of the Stellarator 1.1b, the green helix-like structures represent the helical coils. It should be noted that the stellarator design depicted here is a simple one. Figure from *Deutsche Physikalischen Geselschaft e.V (www.dpg-physik.de on 08.05.2017)*.

"magnetic bottles" can not be made tight to keep all particles confined. This problem is solved by bending the originally linear magnetic field to a toroid-like in the tokamak and stellarator designs, shown in figure 1.1. These have become the most successful options, so that the most developed experiments for fusion research are of both of these designs. It is worth noting that the reason these designs stand out is due to the specific dedication of the research community to study of these designs. Clearly, the amount of success depends on how promising the designs are, and at this point, stellarators and tokamaks continue to be the two most promising designs. There is, nevertheless, a newborn interest in small scale designs and other alternative designs, which is bringing a new face into fusion research[17,103], although these new designs still need to prove whether they are more successful than the tokamak or the stellarator designs.

The *tokamak* design, depicted in figure 1.1a, usually has a D-shaped cross section, as shown in figure 1.5, this shape is the same along the torus, which gives it a toroidal symmetry, i.e. the dynamics tend to be independent of the toroidal angle φ (depicted in figure 1.2). Given the shape of the devices, a toroidal field is needed in order to have a toroidal trap for the electrically charged particles in the plasma. In the case of a uniquely toroidal field there would be some instabilities present due to the different forces acting on the electrons and ions. Therefore the field needs to be modulated in order to include stabilising mechanisms. This modulation is achieved by introducing a poloidal magnetic field, so that the plasma rotates as it moves along the torus. In tokamaks this is achieved by

The curvature gives rise to a drift on the motion of the charged particle. There are also drifts due to the joint effect of magnetic and electric fields, due to the variation of the magnetic and electric fields, and negligible drifts due to gravity.

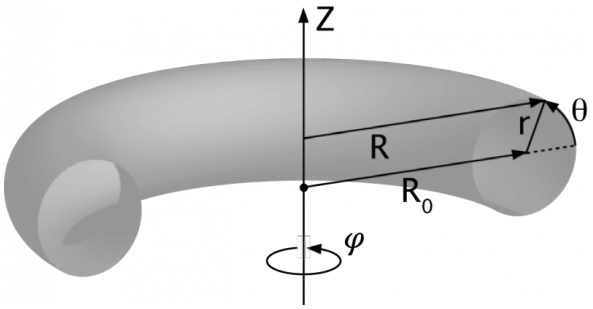

Figure 1.2: The simple toroidal coordinate system is shown along with the cylindrical coordinate system, both generally used for the analysis of toroidal machines. There are four quantities used to describe a toroidal system: the major radius R_0 which is a parameter, the minor radius r, the poloidal angle θ and the toroidal angle φ.

means of a net plasma current, which is generated by the central Ohmic transformer in the centre of figure 1.1a. An unconstrained toroidal current of major radius R has a natural disposition to increase its major radius by the so-called "hoop"-force, as the opposite currents repel each other. To counteract this hoop-force a vertical magnetic field —which is created by the coils depicted in green in figure 1.1a— is needed to prevent the radial expansion of the toroidal current. Also, the transformer at the centre calls for a pulsed operation and each pulse is limited in time by the available maximum voltage the transformer allows.

The International Thermonuclear Experimental Reactor (ITER) is an international effort to demonstrate that fusion energy is a reliable source of clean electric energy. The main objective is to show that the experiment can produce ten times more energy than it needs as input. This energy measure is given by the physics gain factor:

$$Q = \frac{\text{net thermal power out}}{\text{heating power in}} = \frac{P_{out} - P_{in}}{P_{in}} \quad . \tag{1.2}$$

When no fusion is produced, the total output thermal power P_{out}, which is given out through heat conduction and radiation, is exactly the power input P_{in}, accounting for $Q = 0$. When the same amount of fusion power as the input heating power is produced, $Q = 1$, also called *break-even*. And whenever $Q > 1$ there is an energy gain. If Q is not much higher than 1, then the energy production via nuclear fusion is not worth the investment.This is why the goal of ITER is to achieve $Q = 10$, so it can be proven that fusion is a viable way of producing electricity.

In the case of stellarators, the helical twist of the field lines to prevent the charge separation and detrimental $\mathbf{E} \times \mathbf{B}$-drift is achieved by external coils like the additional helical coils shown in green in fig. 1.1b. Thus the stellarator can generate a confining field without an externally driven plasma

The coils need to be kept at a low temperature to maintain their superconductivity, but with the pulsed operation they will irremediably suffer of Ohmic heating. Also, the high power needed can in some cases not be kept for much time, generally big capacitor batteries are used to provide the power needed.

current and can therefore in principle operate in steady-state since no Ohmic transformer is required. The price to pay is that the magnetic field is loosing the axisymmetry and the fields are 3-dimensional in nature. This leads to additional larger diffusive transport than in tokamaks. However, proper shaping of the magnetic field allows an optimisation and thus a reduction of these transport channels. In figure 1.1b this design is depicted as a combination of two sets of coils: the one in red which creates the main toroidal field and the already mentioned helical coils which create the main poloidal component —along with a secondary toroidal component— of the field at different points, resulting in a total field which has a helical structure. This can also be achieved by having coils with intricate shapes, as is the case of the Wendelstein 7-X (Wendelstein 7-X) stellarator, built at the Max-Planck Institut für Plasmaphysik (IPP) in Greifswald, Germany, shown in figure 1.3.

Naturally, due to the almost absence of currents in the stellarator plasmas, they are free of some instabilities which affect tokamaks. The small currents are there in order to satisfy the force balance equation

$$\mathbf{J} \times \mathbf{B} = \nabla p$$

and must naturally satisfy $\nabla \cdot \mathbf{J} = 0$. Both of these conditions give rise to non-zero currents parallel to the magnetic field, termed the Pfirsch-Schlüter current. It is a toroidal component which is much smaller than the one present in tokamaks, nevertheless it can distort the confinement properties of the devices, but optimisation of the flux surface shapes can reduce them significantly and thus their effect on the confining fields. Since stellarators do not rely on a central transformer, they can have a continuous operation regime, which is capable of reaching a steady state due to the lack of strong currents.

Due to the lack of toroidal symmetry, they tend to have worse confinement properties. This can and has been improved by making more complex stellarator designs that rely on the possibility to influence the motion of charged particles in toroidal magnetic fields by proper design, for example giving them symmetry properties in view of the particle motion. Such configurations are called quasi-symmetric as these symmetries can not be achieved perfectly in toroidal geometry (for details see Garren & Boozer [39], Nührenberg & Zille [76], Spong et al. [88]). The intrinsic difficulties and the large computational resources needed in their design have caused a slower progress in the stellarator research than in tokamaks which are easier to design and construct. The Wendelstein 7-X is the biggest stellarator presently working, with the main goal to show that the stellarator line might be a viable candidate for a fusion power reactor. This experiment is a great effort to bring the stellarator devices a step closer to the performance of the present-day working tokamaks. The objective accom-

Parallel current means that it follows the direction of the magnetic field lines. Since field lines in fusion devices are twisted, it makes more sense to talk about parallel and perpendicular components instead of toroidal and poloidal components.

The second biggest is the Large Helical Device (LHD) at the National Institute for Fusion Science (NIFS) in Toki, Japan. It has been operating since 1998 and still produces important scientific results.

plishment relies on a few main characteristics of the Wendelstein 7-X , namely the quasi-steady state operation —pulse length of 30 minutes is finally foreseen— and its optimised properties of good equilibrium and stability properties, low neoclassical transport, small bootstrap current and good fast particle confinement at high pressure.

namely the long time operation of the machine —about 30 minutes of sustained operation, in contrast to the expected 15 minutes of continued pulsed operation for ITER— and its optimised low transport, although the latter is worse than that of ITER.

1.3 Wendelstein 7-X

The Wendelstein 7-X stellarator[45,62,104], depicted in figure 1.3, is a machine which started operation in December 2015 at the Max-Planck Institut für Plasmaphysik (IPP) in Greifswald, Germany. It was designed to have good confinement properties, low neoclassical bootstrap currents and reduced neoclassical transport. The nominal magnetic field strength on the magnetic axis is 2.5T (operation up to 3T is possible), which is achieved by using 50 non-planar and 20 planar superconducting NbTi coils. The plasma major radius is 5.5m (R_0 from fig. 1.2) and the average minor radius is 0.53m (r in fig. 1.2). With this the plasma volume is roughly $30m^3$. The main plasma heating source is electron cyclotron resonance heating (ECRH) providing a heating power of 10MW at 140GHz. Further heating is provided by 5MW NBI at pulsed operation and 4MW ICR heating, which will become available in 2018..

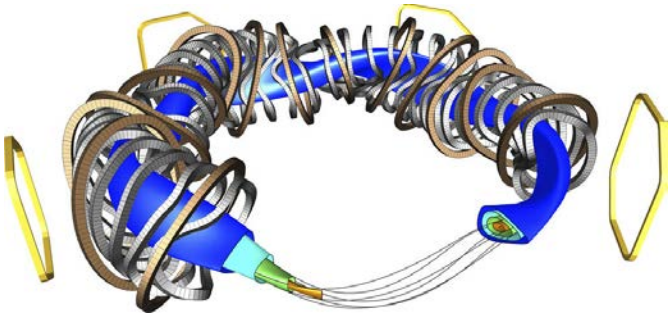

Figure 1.3: Schematics of the Wendelstein 7-X experiment's coils. The coils in grey are the non-planar coils, the ones in orange are the planar coils and the ones in yellow are the trim coils. Four closed surfaces are represented, along with some magnetic field lines lying on the green surface. Image taken from Sunn Pedersen et al. [91], distributed under a Creative Commons CC-BY license.

Since confinement is not perfect energy will flow to the edge of the plasma, eventually making its way to the vacuum vessel. In order to channel the interaction of plasma with the material wall, a staged approach in the assembly of the in-vessel parts of the machine had been chosen for Wendelstein 7-X [57,79,86,89]. For the first operation phase, know as $OP1.1$, which lasted from December 2015 to March 2016 and which was basically an integrated commissioning phase for the machine and the control systems, these protecting elements were five carbon limiter stripes. Due to

the reduced particle and heat exhaust ability of the limiters, the pulses during $OP1.1$ were limited to a total energy input per pulse of 4MJ (e.g. 4MW for 1 second).

This is changed for the presently running experimental phase called $OP1.2$ (from mid 2017 into the second half of 2018), for which an uncooled graphite divertor was installed for the so-called island divertor operation in which the interaction between divertor and plasma is via intrinsic magnetic islands limiting the confinement region with good flux surfaces. The particle and energy fluxes are guided to the divertor targets via the island separatrix. The pulse duration in this phase is limited by the heating up of these components which is expected to be around 80MJ. For the second part of $OP1.2$, from end 2018 to end of 2020, there will be an upgrade of the in-vessel components by which the uncooled divertor will be replaced by a water-cooled divertor of the same geometry which can withstand $10\mathrm{MW/m^2}$ steady-state heat loads. In the following operational phase, called $OP2$, the exploration of the steady-state capabilities is planned.

One of the key elements of the design of the Wendelstein 7-X is the island divertor. Generally for tokamaks, there is an x-point well defined at the bottom of the structure, as shown in figure 1.5. For stellarators, given their 3D geometry, an x-point, if present, has to run around helically according to the periodicity and the helicity of the magnetic field. In order to generate an island structure in a stellarator, a so-called resonant magnetic surface needs to be present on which the field lines close after a specific number of toroidal (m) and poloidal (n) turns. The winding number, or the so-called rotational transform iota, of such a surface is n/m. Field components radial to such a surface can break the surface and lead to the formation of magnetic islands. In the case of the Wendelstein 7-X, the magnetic configuration has been designed in such a way that there are islands at the edge of the plasma, creating in this way x-points in the configuration. The islands help maintaining the deposition of energy at a given position of the walls, which is where the divertor (or limiters) are located. The device can operate with three different configurations, each with a different island chain acting as the island divertor: $\iota = 5/4, 5/5$ or $5/6$ (Renner et al.[86]). The case for the $5/5$ divertor island chain was pictured by Feng et al.[33] and is presented in figure 1.4. Because of the importance of the magnetic field structure for the correct energy deposition on the walls, it is of utter importance that the magnetic field boundary topology can be maintained sufficiently stable. Therefore prediction of the effects of possible currents which may develop, on the topology of the magnetic fields at the plasma boundary is of utmost importance in order to counteract the changes if necessary[40]. This is where the improvement of 3-D MHD equilibrium codes is needed in order to allow further advances for stellarators towards their reactor viability.

1.4 Tools for the analysis of plasma equilibria of experiments

This work is centred in the analysis of equilibrium solutions for magnetically confined plasmas, following ideal MHD theory. This is important in all of the phases of a device, from design to analysis

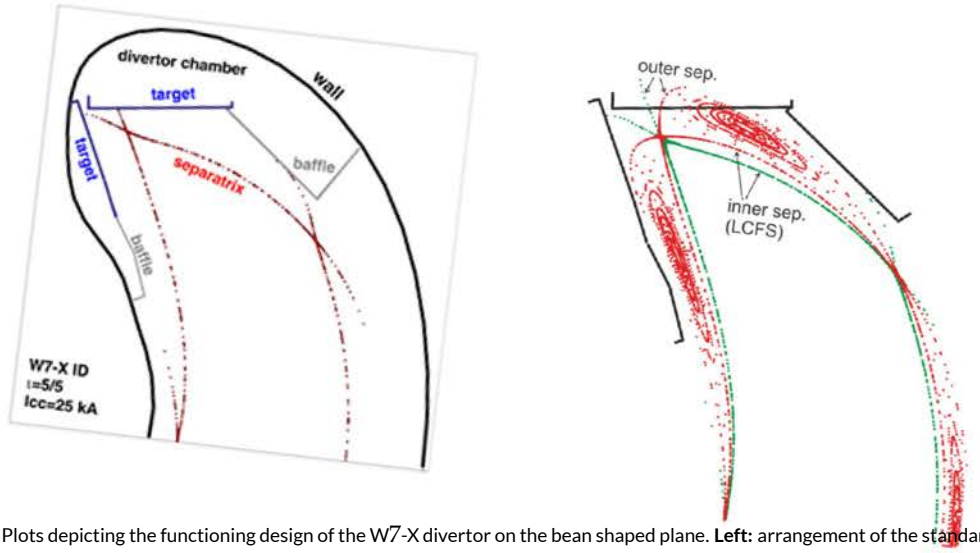

Figure 1.4: Plots depicting the functioning design of the W7-X divertor on the bean shaped plane. **Left:** arrangement of the standard divertor configuration. Between both targets there is a gap so that neutrals can be trapped in the divertor chamber. **Right:** Overposition of a Poincare plot for W7-X standard configuration showing that the material escaping through the separatrix should be directed straight into the divertor gap, the rest of the energy being deposited on the targets. From Feng et al. [33] PERMISSION PENDING!!!

of experiments. The tools discussed here are of great importance when analysing the global properties of magnetic confinement experiments and can be used to validate a given design, to corroborate experimental results and to shed some light on phenomena for which there is no theoretical explanation. The tools discussed here are clearly not enough to study all that can and needs to be studied in fusion plasmas. Along with these there are codes designed to study the individual behaviour of particles and the outwards transport of particles to quantify the confinement properties and analyse the turbulence in fusion plasmas, codes to study the possible instabilities and help quantifying the stability of a given design as well as codes for simulating the interaction between the heating mechanisms or the active diagnostics with the plasma.

Given that the plasma is an electrically charged gas, the interactions between particles are harder to describe than those of a neutral gas. The theory used for studying plasma interactions will be presented in detail in chapter 2, for now, it is enough to mention that given the amount of particles in the system, the most efficient way of doing the analysis is by using a statistical approach, generally know as the *kinetic theory of plasmas*. If this theory is simplified as explained in the next chapter, one is left with the theory known as *Magnetodydrodynamics*, or MHD to shorten it [42]. If further simplified, as we shall see, the obtained theory is called *ideal MHD*.

In any of the previous cases, an analytical solution of the system can only be achieved in special and sometimes simplified cases but not in the general 3D geometries.. Numerical simulations help us getting a solution to the system of equations given by these theories for the conditions present in nuclear fusion devices. When there is interest in solving the dynamics of energetic particles, for

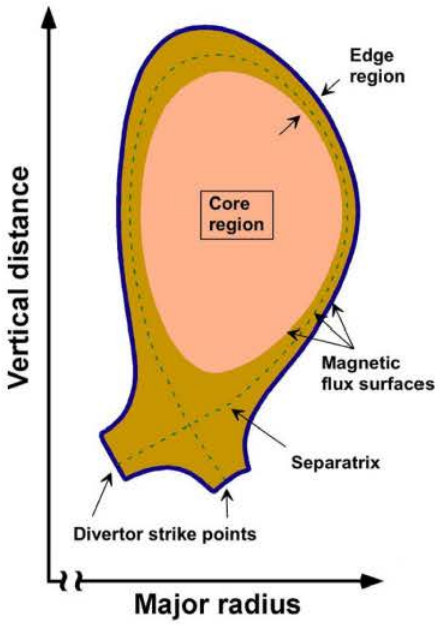

Figure 1.5: Plasma regions in a tokamak. The core region is where the plasma is fully confined, ideally the magnetic lines there form concentric magnetic surfaces. The *separatrix*, also last closed flux surface (LCFS), separates the confined plasma from the outer region where field lines are generally open. For tokamaks, the magnetic configuration shows a so called *x-point*, which is where the LCFS magnetic surface reconnects or closes on itself, which is used for a controlled energy deposition to the outside, having the divertor at the known hitting points. Taken from Tillack et al. [96]

.

example, it is appropriate to describe the system using the kinetic theory. If we want to check the general interaction of the magnetic field and the plasma currents then ideal MHD would suffice. There are many codes, each focusing on a specific problem. In this work we will focus on the usage of two of these, which will be explained in more detail in chapter 3 and which are briefly described below.

VMEC[52,53] is the most widely used code when it comes to equilibrium solutions of a magnetically confined plasma consistent with the ideal MHD theory. It provides, under certain assumptions, the magnetic field configuration that results from requiring force-balance between the Lorenz forces and the plasma pressure everywhere in the confining volume. The most important and limiting assumption is that the magnetic configuration has a nested-tori structure which is referred to as nested magnetic surfaces. This means that the magnetic field lines are organised on nested toroidal surfaces around a common axis. A violation of this assumption has already been stated in the case of the Wendelstein 7-X , which relies on magnetic islands for the proper operation of its divertor, as was seen in figure 1.4. This assumption may not be valid everywhere inside dynamic machines, such as tokamaks, where the evolution of the plasma can lead to the formation of magnetic islands inside of the confining volume. This is the origin, for instance, of the so-called sawtooth phenomena in

tokamaks[13,82,101]. Also, of discharge-ending instabilities known as disruptions[106].

There are situations, however, in which magnetic islands and stochastic regions are essential to the problem. For instance, in the case of the island divertor that W7-X possesses at the plasma boundary, or when resonant magnetic perturbations are applied to control instabilities, such as the so-called ELMs in tokamaks. In these cases, VMEC falls short of providing an adequate tool. Other codes must be used instead.

This work will be centred on the Scalable Iterative Equilibrium Solver for Toroidal Applications (SIESTA)[54], which works on the solution given by VMEC, taking it as an initial approximation. SIESTA does not make any assumption on the underlying magnetic topology, though. As a result, the locations where magnetic islands may develop (to be detailed in chapter 2) may become unstable and local reconnection can take place. To help this process, SIESTA introduces an artificial resistivity during the first iterations of its algorithm, that is then quickly switched off to allow convergence to an equilibrium solution. SIESTA also permits the introduction of external magnetic perturbations, that could be applied to study the external control of magnetic islands.

Working on the solution given by VMEC has an inconvenience, i.e. the numerical analysis is limited to the region which VMEC analyses. This means that SIESTA, as was originally conceived, is only able to analyse the plasma inside of the LCFS. SIESTA is thus a fixed-boundary code, which means that it does not modify the LCFS provided by VMEC. As a result, any situation that includes a resonance near the edge of the plasma will not be adequately modelled. This is for instance the case for W7-X and its island divertor. If any type of uncontrolled current would shift the island chain towards the plasma, SIESTA would not be able to study the effects on the LCFS in its current form.

1.5 Objective

Solving the aforementioned limitation of SIESTA is the main objective of this work. The details of the solution provided will be presented in detail in chapter 4, but the main idea is to expand the numerical domain analysed by SIESTA, so instead of taking only the region where the confined plasma resides, pictured pink in figure 1.5, we expand the volume of analysis up to the vessel, or an approximated surface on an external point close to it. While the edge has more important contributions which may affect it than those considered in ideal MHD, many features of the outermost parts of the core and the innermost parts of the edge region seem to be sufficiently well approximated by ideal MHD. In addition, given the iterative nature of SIESTA, proper initial guesses for the magnetic field and pressure in the pseudo-vacuum region between the plasma edge and the vessel must also be provided. Given the peculiarities of SIESTA, these guesses must satisfy certain physical criteria (i.e., a divergence-free magnetic field, non-zero pressure, near force-balance) to facilitate the solution. This will be discussed at length in Chapter 4.

Then, we will illustrate the usefulness of the new extended SIESTA to a real problem in W7-X in

Chapter 5. In particular, we will use SIESTA to assess the effectiveness of several proposed electron cyclotron current drive (ECCD) scenarios that aim at controlling the effects of undesired neoclassical bootstrap currents on the position and size of the edge islands of W7-X which should interact with the divertor targets.

2

Equilibrium and Stability

As mentioned in the introduction, a plasma has different ways of being described, depending on what the interest is. The most basic and complete way of analysing plasmas is through the Kinetic theory, also Boltzmann theory. This model describes the plasma dynamics by evolving the distribution functions of ions and electrons together with Maxwell equations for the confining field, which gives a statistical behaviour of particles in the plasma. Depending on the temperature and density of the plasma of interest, a particle approach may not be necessary, and a fluid approach is more than enough. A less complicated description is the two fluid model, which considers the ions as one fluid and the electrons as another fluid. This is a good model for describing the general behaviour of the different species in the plasma (electrons and ions), when the collisionality is important in the plasma and length scales are much longer and larger than those associated to particle gyromotion, making the particles' gyromotion irrelevant for the analysis. A further simplification is to consider the plasma as one fluid, to which ions provide the mass and the more mobile electrons provide the current called the MHD model. In this chapter we will follow a simple path from the kinetic model to the ideal MHD model.

Throughout this work when the word *plasma* is written we refer to a plasma of fusion interest, unless otherwise specified. This means, as will be seen below, that the plasma is considered collisionless, quasi-neutral and it is supposed to be fully ionised.

2.1 Theoretical analysis of plasmas

Plasmas consist of a high number of charged particles, therefore, when analysing considerable volumes of plasma, it is convenient to recur to statistical models in order to get a better understanding

of the global behaviour of plasmas. Although, it is clear that if one is interested in the motion of a single particle, then one must state the dynamic equations for the particle taking in consideration the different force fields acting on it.

2.1.1 Kinetic theory

Let us start start by the kinetic model. Here we follow the derivation by Goedbloed & Poedts [42] and making some references to Freidberg [36], if the reader wants to deepen into any of the topics mentioned here, those books should serve to lead the way. The Boltzmann equation describes the statistical behaviour of the different species in phase space, i.e. it gives a probability of a particle being located at a given position with a given velocity at a given time $f_\alpha(\mathbf{r}, \mathbf{v}, t)$, taking in consideration the interactions of particles between themselves and with external fields. If we neglect the gravitational interaction, the evolution of the distribution function f_α looks like this:

$$\begin{aligned}\frac{df_\alpha}{dt} =& \frac{\partial f_\alpha}{\partial t} + \frac{\partial f_\alpha}{\partial \mathbf{r}} \cdot \frac{\partial \mathbf{r}}{\partial t} + \frac{\partial f_\alpha}{\partial \mathbf{v}} \cdot \frac{\partial \mathbf{v}}{\partial t} \\ =& \frac{\partial f_\alpha}{\partial t} + \frac{\partial f_\alpha}{\partial \mathbf{r}} \cdot \mathbf{v} + \frac{q_\alpha}{m_\alpha} \frac{\partial f_\alpha}{\partial \mathbf{v}} \cdot (\mathbf{E} + \mathbf{v} \times \mathbf{B}) \qquad . \end{aligned} \tag{2.1}$$

When there is no interactions between particles, $\frac{df_\alpha}{dt}$ becomes zero, and the resulting equation is called the *Vlasov equation*. When there is interactions, i.e. collisions, it is necessary to include a factor that accounts for this:

$$\left(\frac{\partial f_\alpha}{\partial t}\right)_{coll} = \frac{\partial f_\alpha}{\partial t} + \frac{\partial f_\alpha}{\partial \mathbf{r}} \cdot \mathbf{v} + \frac{q_\alpha}{m_\alpha} \frac{\partial f_\alpha}{\partial \mathbf{v}} \cdot (\mathbf{E} + \mathbf{v} \times \mathbf{B}) = C_\alpha \qquad , \tag{2.2}$$

which is called the *Boltzmann equation*. The collision term can be modified accordingly to include any kind of interactions between particles. According to the assumptions on this term, so will be the range of validity of the kinetic model.

For very hot plasmas, as is the case of those used for fusion research, collisions are not that important on a global scale, therefore the system is completely described by *Vlasov's equation*

$$\frac{\partial f_\alpha}{\partial t} + \frac{\partial f_\alpha}{\partial \mathbf{r}} \cdot \mathbf{v} + \frac{q_\alpha}{m_\alpha} \frac{\partial f_\alpha}{\partial \mathbf{v}} \cdot (\mathbf{E} + \mathbf{v} \times \mathbf{B}) = 0 \qquad . \tag{2.3}$$

This consideration forces some limitations on the plasma for eq. (2.3) to be valid, namely:

1. The mean particle distance must be smaller than the Debye length. This means that in a sphere of radius equal to a Debye length, there should be a statistically significant number of particles.

2. The collision frequency is much smaller than the plasma frequency, to be able to neglect the collision integral.

In order to understand this conditions, a couple of definitions are needed:

- The Debye length is the distance at which an external electric field is shielded, which is explained through the high conductivity of the plasma. The Debye length can also be interpreted as a typical distance at which charge imbalance due to thermal fluctuations can occur. The expression for it is

$$\lambda_D \equiv \sqrt{\frac{\varepsilon_0 k_B T_e}{n_e e^2}} \tag{2.4}$$

  where n_e is the electron density and T_e is the electron temperature.

- The charge imbalance is considered to be driven mainly by the movement of electrons, due to the higher ion mass. The imbalance can be considered as electrons oscillating in the plasma, this oscillations occur at a frequency

$$\omega_p = \sqrt{\frac{n_e e^2}{\varepsilon_0 m_e}} \tag{2.5}$$

  which is called *plasma frequency*.

The full description of the plasma is obtained when either Boltzmann's (2.2) or Vlasov's (2.3) equation is combined with Maxwell's equations:

$$\nabla \times \mathbf{E} = -\frac{\partial \mathbf{B}}{\partial t} \tag{2.6a}$$

$$\nabla \times \mathbf{B} = \mu_0 \mathbf{J} + \varepsilon_0 \mu_0 \frac{\partial \mathbf{E}}{\partial t} \tag{2.6b}$$

$$\nabla \cdot \mathbf{E} = \frac{\sigma}{\varepsilon_0} \tag{2.6c}$$

$$\nabla \cdot \mathbf{B} = 0 \quad . \tag{2.6d}$$

To relate Boltzmann's or Vlasov's equation to Maxwell's equations, one makes use of the zeroth and first moment of the particle distributions f_α, in order to obtain an expression for the particle density and their velocities:

$$n_{\alpha\,(\mathbf{r},t)} \equiv \int f_{\alpha\,(\mathbf{r},\mathbf{v},t)} d^3v, \qquad \sigma_{(\mathbf{r},t)} \equiv \sum q_\alpha n_\alpha \tag{2.7a}$$

$$\mathbf{u}_{\alpha\,(\mathbf{r},t)} \equiv \frac{1}{n_{\alpha\,(\mathbf{r},t)}} \int \mathbf{v} f_{\alpha\,(\mathbf{r},\mathbf{v},t)} d^3v, \qquad \mathbf{J}_{(\mathbf{r},t)} \equiv \sum q_\alpha n_\alpha \mathbf{u}_\alpha \tag{2.7b}$$

Notice that all of these quantities are macroscopic, which means that there is no dependence on single particles qualities, rather on the macroscopic averages.

2.1.2 Two fluid model

So far, the equations describe the global behaviour of particles, taking into account the global magnetic and electric fields. This is still a kinetic model because the dynamics of the system is described by Boltzmann's equation. In order to obtain the equations describing the two fluid model, we take the first three moments of the Boltzmann equation, to have a more general model:

$$\int \left[\frac{df_\alpha}{dt} - \left(\frac{\partial f_\alpha}{\partial t}\right)_{coll}\right] d^3v = 0 \qquad \text{Mass conservation}$$

$$\int m_\alpha \mathbf{v} \left[\frac{df_\alpha}{dt} - \left(\frac{\partial f_\alpha}{\partial t}\right)_{coll}\right] d^3v = 0 \qquad \text{Momentum conservation}$$

$$\int \frac{m_\alpha v^2}{2} \left[\frac{df_\alpha}{dt} - \left(\frac{\partial f_\alpha}{\partial t}\right)_{coll}\right] d^3v = 0 \qquad \text{Energy conservation}$$

Since the Coulomb collisions are dominantly elastic —and therefore mass, momentum and energy should be conserved—, when doing the calculations to obtain the zeroth moment, the the following considerations should be made:

- There is conservation of particles (mass) at collisions between like and unlike particles, i.e.

$$\int C_{ee} d^3v = \int C_{ii} d^3v = \int C_{ei} d^3v = 0$$

  where $\left(\frac{\partial f_\alpha}{\partial t}\right)_{coll} \propto C_{\alpha\beta}$.

- The energy and the momentum are conserved in like particle collisions, i.e.

$$\int m_\alpha \mathbf{v} C_{\alpha\alpha} d^3v = 0$$

$$\int \frac{m_\alpha v^2}{2} C_{\alpha\alpha} d^3v = 0 \qquad .$$

- For unlike particle collisions, energy and momentum should also be conserved:

$$\int \left(m_e \mathbf{v}_e C_{ei} + m_i \mathbf{v}_i C_{ie}\right) d^3v = 0$$

$$\int \frac{1}{2} \left(m_e v_e^2 C_{ei} + m_i v_i^2 C_{ie}\right) d^3v = 0 \qquad .$$

A detailed derivation of the model can be followed in Freidberg [36] or Goedbloed & Poedts [42].

With these considerations, and decomposing the velocity in an average part and a random part $\mathbf{v} = \mathbf{u}_\alpha + \mathbf{w}$ the resulting equations simplify somewhat. After some math, it is possible to obtain the following equations for the three first moments:

$$\frac{\partial n_\alpha}{\partial t} + \nabla \cdot (\mathbf{u}_\alpha n_\alpha) = 0 \tag{2.8a}$$

$$m_\alpha n_\alpha \frac{d\mathbf{u}_\alpha}{dt} - q_\alpha n_\alpha \left(\mathbf{E} + \mathbf{u}_\alpha \times \mathbf{B}\right) + \nabla \cdot \overleftrightarrow{\mathbf{P}}_\alpha = \mathbf{R}_\alpha \tag{2.8b}$$

$$\frac{3}{2} n_\alpha \left(\frac{dT_\alpha}{dt}\right) + \overleftrightarrow{\mathbf{P}}_\alpha : \nabla \cdot \mathbf{u}_\alpha + \nabla \cdot \mathbf{h}_\alpha = Q_\alpha \tag{2.8c}$$

where the two dots in the last equation means that there is a double summation in cartesian coordinates $\overleftrightarrow{\mathbf{P}}_\alpha : \nabla \cdot \mathbf{u}_\alpha = \sum_i \sum_j P_{ij\alpha} \partial u_i / \partial x_j$, and the following substitutions have been made

- $\overleftrightarrow{\mathbf{P}}_\alpha \equiv m_\alpha \int \mathbf{w}\mathbf{w} f_\alpha d^3w = p_\alpha \mathbf{I} + \overleftrightarrow{\mathbf{\Pi}}_\alpha$ is the stress tensor, having the scalar pressure $p_\alpha = \frac{n_\alpha m_\alpha}{3} \int w^2 d^3w$ contribution —which is isotropic— and the anisotropic part $\overleftrightarrow{\mathbf{\Pi}}_\alpha$;
- $\mathbf{R}_\alpha \equiv \int m_\alpha \mathbf{w} C_{\alpha\beta} d^3w$ is the momentum transfer between unlike particles due to collisions or friction;
- $T_\alpha \equiv \frac{p_\alpha}{n_\alpha k}$ is the temperature;
- $\mathbf{h}_\alpha \equiv \frac{1}{2} n_\alpha m_\alpha \int w^2 \mathbf{w} d^3w$ is the heat flux due to velocity fluctuations;
- $Q_\alpha \equiv \int \frac{1}{2} m_\alpha w^{2\prime}{}_\alpha C_{\alpha\beta} d^3w$ is the heat generated due to the random collisions between unlike particles.

Equation (2.8a) is called the continuity equation, eq. (2.8b) is the momentum equation and eq. (2.8c) is the energy equation, which is also sometimes called heat balance equation. The two fluid model is completed by Maxwell's equations (2.6), where Ampère's equation (2.6b) and Gauss' equation (2.6c) are slightly modified by the definitions of density and current density

$$\nabla \times \mathbf{B} = \mu_0 e (n_i \mathbf{u}_i - n_e \mathbf{u}_e) + \varepsilon_0 \mu_0 \frac{\partial \mathbf{E}}{\partial t} \tag{2.9a}$$

$$\nabla \cdot \mathbf{E} = \frac{e}{\varepsilon_0} (n_i - n_e) \tag{2.9b}$$

with e being the elementary charge, assuming singly charged ions.

2.1.3 Single fluid MHD model

Up to now, no specific assumptions have been taken on the collision operator, other than the logical considerations stated before. The previous model is called the two fluid model, since there are

two species which are considered as fluids. The collision operator is part of the seemingly macroscopic quantities $\mathbf{R}_\alpha$ and Q_α. Also, higher moments are hidden in $\overleftrightarrow{\mathbf{P}}_\alpha$ (through $\overleftrightarrow{\mathbf{\Pi}}_\alpha$) and in $\mathbf{h}_\alpha$. The complete definition of these quantities is still related to the kinetic theory since they depend on microscopic quantities. To obtain the closure for the present system of equations is not an easy job. Among many possible solutions found in literature (see, for example, Abdelmalik & van Brummelen [1], Baganoff & Elliott [3], Balescu [4,5], Hinton & Hazeltine [49], Mueller & Ruggeri [75], Torrilhon [97]) there are two main approaches: the use of kinetic theory in order to obtain the transport coefficients, which requires some major simplifications, an example of which is Grad's expansion in Hermite polynomials [44]; and the use of phenomenological approaches, like invoking Fick's law to obtain the diffusion coefficients.

For our present mission, we shall take more simplifications in order to obtain the *ideal MHD* model, first going through the *resistive MHD* model. The first assumptions on the model are that MHD length and time scales are large compared to plasma [kinetic] scales, i.e. $\lambda_{MHD} \gg \lambda_i$ and $\tau_{MHD} \gg \omega_i^{-1}$, respectively. Here, the quantity $\omega_i \equiv ZeB/m_i$ is the ion gyro-frequency, which is the frequency at which ions turn around the magnetic field lines, and $\lambda_i \equiv v_{\perp i}/\omega_i$ is the ion Larmor radius or gyro-radius, which is the radius at which the ion rotates around the field line. Due to the definitions of the gyro-frequency and the gyro-radius, the intensity of the magnetic field plays an important role, i.e. the greater the field, the easier these conditions are fulfilled.

The second simplification is to neglect ion and electron viscosities and heat conductivities. This leaves only the isotropic part of the stress tensor, i.e. the scalar pressure, and a reduced version of the heat transfer, namely

$$Q_e = \frac{1}{en_e}\mathbf{R}_e \cdot \mathbf{J} - Q_i \qquad ; \qquad Q_i = \frac{3n_e k(T_e - T_i)}{2\tau_{eq}}$$

where τ_{eq} is the temperature equilibration time scale and the electron-ion momentum transfer is simplified to

$$\mathbf{R}_e = \eta e n_e \mathbf{J} \approx \frac{\eta e \rho Z}{(1+\mu)m_i}\mathbf{J} \qquad .$$

Here μ is the mass ratio $\mu \equiv Zm_e/m_i$.

This set of approximations also eliminates the higher moment $\mathbf{h}_\alpha$. The terms related to resistivity, which are part of $\mathbf{R}_\alpha$ and Q_α, are kept, as seen above.

Since the considered scales are meant to see the plasma as a whole and not as two fluids, the fluid

This is the longest relaxation time scale in our system

$$\tau_{eq} = \frac{m_i}{2m_e}\tau_e$$

quantities need to be appropriately adjusted to one fluid,

$$\rho \equiv n_e m_e + n_i m_i \tag{2.10a}$$
$$\sigma \equiv -e(n_e - Z n_i) \tag{2.10b}$$
$$\mathbf{v} \equiv \frac{1}{\rho}(n_e m_e \mathbf{u}_e + n_i m_i \mathbf{u}_i) \tag{2.10c}$$
$$\mathbf{J} \equiv -e(n_e \mathbf{u}_e - Z n_i \mathbf{u}_i) \tag{2.10d}$$
$$p \equiv p_e + p_i \quad . \tag{2.10e}$$

The temperature of the ions and electrons is supposed to be the same, which is a rational assumption for a plasma in equilibrium under magnetic confinement conditions. Also, since there is only one fluid and due to the assumed isotropic distribution, quasi-neutrality is assumed:

$$|n_e - Z n_i| \ll n_e$$

These set of approximations lead to the *resistive MHD equations*:

$$\frac{\partial \rho}{\partial t} + \nabla \cdot (\rho \mathbf{v}) = 0 \tag{2.11a}$$
$$\rho \left(\frac{\partial \mathbf{v}}{\partial t} + \mathbf{v} \cdot \nabla \mathbf{v} \right) + \nabla p - \mathbf{J} \times \mathbf{B} = 0 \tag{2.11b}$$
$$\frac{\partial p}{\partial t} + \mathbf{v} \cdot \nabla p + \gamma p \nabla \cdot \mathbf{v} = (\gamma - 1)\eta |\mathbf{J}|^2 \tag{2.11c}$$
$$\frac{\partial \mathbf{B}}{\partial t} + \nabla \times \mathbf{E} = 0 \tag{2.11d}$$

with

$$\mathbf{J} = \frac{1}{\mu_0} \nabla \times \mathbf{B} \tag{2.12a}$$
$$\mathbf{E} + \mathbf{v} \times \mathbf{B} = \eta \mathbf{J} \tag{2.12b}$$

and of course there should be no magnetic monopoles $\nabla \cdot \mathbf{B} = 0$. Here, η is the resistivity and $\gamma = C_P / C_V$ is the ratio of specific heats at constant pressure and at constant volume, respectively.

This deduction has been done following the one by Goedbloed & Poedts [42], chap. 3, hence the appearance of the Joule heating term in the internal energy equation (2.11c) (which also appears, for example, in the deduction by Boyd & Sanderson [16]). In most of the literature (for example Chen [22], Dolan [29], Freidberg [36], Goldston & Rutherford [43]), this term is usually neglected, i.e. any type of heat flow is neglected and they are left with the *adiabatic equation of state*, where the r.h.s. of equa-

tion (2.11c) is zero. This is a result of the assumption that the macroscopic dimension of the system analysed is large enough for the resistive diffusion time to be long compared to the typical MHD time τ_{MHD}. For the cases where resistivity is important, the macroscopic scales of interest might not fulfil this condition, which is why we have kept this term.

Ideal MHD

A further simplification can be made on the single fluid or MHD model just studied to obtain what is termed the *ideal MHD* model. Notice that equations (2.11) are the ones that describe the whole system, now equations (2.12) are just the way to relate $\mathbf{J}$ and $\mathbf{E}$ to the variables of the system. In order to obtain the *ideal MHD* model we just take null resistivity, which is true for the core of the plasma in nuclear fusion devices, but as the plasma get colder towards the edges this approach may not be valid. Making this change, we can rewrite the ideal MHD equations as

$$\frac{d\rho}{dt} = 0 \tag{2.13a}$$

$$\rho\frac{d\mathbf{v}}{dt} + \nabla p - \mathbf{J}\times\mathbf{B} = 0 \tag{2.13b}$$

$$\frac{d}{dt}\left(\frac{p}{\rho^\gamma}\right) = 0 \tag{2.13c}$$

$$\frac{\partial\mathbf{B}}{\partial t} + \nabla\times\mathbf{E} = 0 \tag{2.13d}$$

$$\frac{1}{\mu_0}\nabla\times\mathbf{B} = \mathbf{J} \tag{2.13e}$$

where we have used the definition of the convective derivative $\frac{d}{dt} = \frac{\partial}{\partial t} + \mathbf{v}\cdot\nabla$. These equations can be rewritten as conservation equations, i.e.,

$$\frac{\partial X}{\partial t} + \nabla\cdot(\mathbf{Y}) = 0$$

where X represents the conserved quantity and $\mathbf{Y}$ a flux-like quantity. For example, for Faraday's law eq. 2.13d, if we use Ohm's law with perfect conductivity $\mathbf{E} + \mathbf{v}\times\mathbf{B} = 0$, then we obtain the magnetic flux conservation equation

$$\frac{\partial\mathbf{B}}{\partial t} - \nabla\cdot(\mathbf{B}\mathbf{v} - \mathbf{v}\mathbf{B}) = 0$$

where we have used the equality $\nabla\times(\mathbf{a}\times\mathbf{b}) = \nabla\cdot(\mathbf{b}\mathbf{a} - \mathbf{a}\mathbf{b})$. Similarly, with a bit more of algebraic handling, it is possible to obtain the conservation form for the momentum equation (the

continuity and energy equations are already conservation equations),

$$\frac{\partial}{\partial t}(\rho \mathbf{v}) + \nabla \cdot \left[\rho \mathbf{v}\mathbf{v} + (p + 1/2B^2)\mathbf{I} - \mathbf{B}\mathbf{B}\right] = 0 \qquad ,$$

where the quantity inside of the square brackets is the stress tensor. Therefore, one important property of ideal MHD comes up, which is that the mass, momentum and energy are conserved, along with the magnetic flux.

The conservation of magnetic flux implies that the magnetic topology must remain the same, which limits the accessible energy states of the system. This is only satisfied when no resistivity is considered. The inclusion of resistivity gives access to different energy states and allows for a reconfiguration of the magnetic topology. For example, a given magnetic field under perturbation —e.g. due to plasma pressure—, in ideal MHD will only move the magnetic flux surfaces, but since flux is conserved the topology of the configuration cannot change. In resistive MHD the flux needs not be conserved, therefore magnetic field lines can break and reconnect to reach a state with a different magnetic topology and less energy. This discussion is the basis of work of SIESTA, which will be discussed in the next chapter, but the reader should keep this in mind.

2.2 Equilibrium

When considering magnetic confinement, the situation which is aimed at is reaching a *static equilibrium*, whether the equilibrium is stable or not is another branch of study, which closely relates to equilibrium studies but we shall not treat it here. By static equilibrium it is understood that time derivatives disappear from the ideal MHD equations, therefore the system reduces to

$$\mathbf{J} \times \mathbf{B} = \nabla p \tag{2.14a}$$

$$\frac{1}{\mu_0} \nabla \times \mathbf{B} = \mathbf{J} \tag{2.14b}$$

$$\nabla \cdot \mathbf{B} = 0 \tag{2.14c}$$

The potential energy of this system is given by

$$W = \int \left(\frac{B^2}{2\mu_0} + \frac{p}{\gamma - 1} \right) d^3 r \tag{2.15}$$

As many physical systems, an equilibrium is said to be reached when the potential energy is minimum. The number of states, or equilibria, that can be reached depends on the degrees of freedom taken into account. For example, as mentioned before, if surfaces are allowed to break open at a given point —through whichever method—, then an extra degree of freedom is introduced since

new magnetic topologies, i.e. new energy states, could be reached.

Equation (2.14a) states that the pressure gradients are compensated by the Lorentz force. The more direct relation between the plasma pressure and the magnetic pressure is actually an important quantity for describing plasmas, defined as

$$\beta \equiv 2\mu_0 \frac{< p >}{B^2} \qquad . \tag{2.16}$$

In fusion research, the β value tells about the performance of a device, i.e. it tells how much magnetic force is needed in order to confine the plasma. On the other hand, the general rule is that the higher beta is the closer to instabilities the plasma is. For instance, for tokamaks the beta value (volume average) is generally $< \beta > \lesssim 1\%$, though maximum values of $\sim 10\%$ have been reached[65]; for stellarators it is easier to reach higher beta values than for tokamaks, normal functioning being around $2 - 3\%$. When the magnetic field of a given device is known, the beta value gives an idea of the density for a given equilibrium. The reader will notice the use of the β percentage ($\beta * 100$) for the description of the equilibria studied in this work.

Coming back to the force compensation, if we apply a scalar or dot product with $\mathbf{B}$ to equation (2.14a) we are left with

$$\mathbf{B} \cdot \nabla p = 0 \qquad ,$$

which tells us that there is no pressure gradients along the magnetic field lines, or what is equivalent, that the pressure aligns itself to the magnetic field. This is also the case for the plasma currents $\mathbf{J}$. The magnetic field lines, for magnetic fusion devices, generally lie on a set of nested surfaces, which are called magnetic surfaces or flux surfaces. The point of the flux surfaces is that, since magnetic flux is conserved, one can define surfaces which have a fixed flux, which will remain the same due to the conservation properties of the system, with the magnetic flux defined by

$$\Phi_B = \int \mathbf{B} \cdot \mathbf{n} dS \qquad . \tag{2.17}$$

At the centre of the nested toroidal magnetic surfaces, lies the magnetic axis. The general structure of the magnetic surfaces is sketched in figure 2.1a, where a desired configuration of nested closed magnetic surfaces is plotted with colours representing the pressure at each of the surfaces.

Each of the magnetic surfaces can be labelled via the flux, so that the quantities become a function of the flux instead of the cartesian or cylindrical coordinates. For this, two separate fluxes are

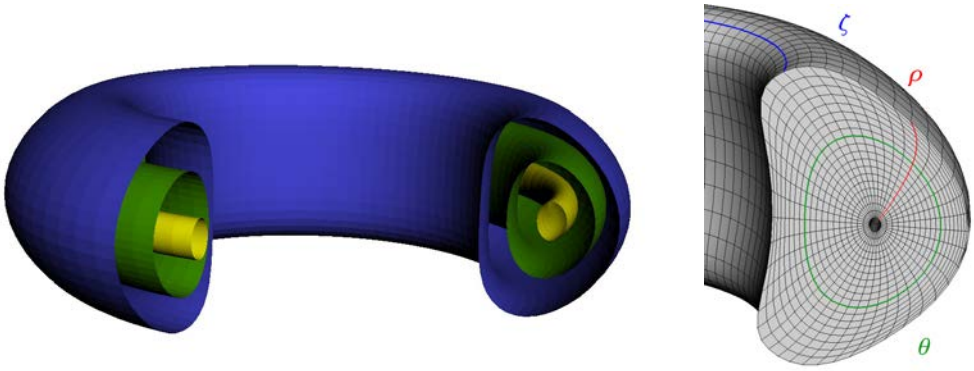

(a) Representation of magnetic surfaces.

(b) Example of VMEC coordinates.

Figure 2.1: Concentric magnetic surfaces are shown in 2.1a. These correspond to three surfaces of the D3D device. The colours represent the change of plasma pressure inside any toroidal device, the closer to the axis the higher the pressure. In fig. 2.1b an example for the flux coordinates used by VMEC on the same device is shown.

defined, namely, the toroidal ϕ and the poloidal χ fluxes:

$$\phi = \frac{1}{2\pi} \int \mathbf{B} \cdot \nabla \varphi \, dS_\varphi \tag{2.18a}$$

$$\chi = \frac{1}{2\pi} \int \mathbf{B} \cdot \nabla \theta \, dS_\theta \tag{2.18b}$$

where θ is defined as the poloidal angle and φ as the toroidal angle, as illustrated in figure 2.1b. With this definition the toroidal flux ϕ can be taken as a radial coordinate —the "ρ" shown in fig. 2.1b— instead of the radius of toroidal coordinates, which can only describe cylindrical surfaces around the major axis. We will comment more on flux coordinates when studying the basics of the VMEC code in the next chapter. For now, knowing that the magnetic flux can be used in order to define a radial coordinate in a system is enough.

In order to obtain closed magnetic surfaces, a field line on that surface should not close on itself. If on a given magnetic surface a magnetic field line closes on itself, i.e. after a given number n of toroidal turns it comes back where it started after having turned m times in the poloidal direction, then it is defined as a *rational surface*. Rational surfaces may turn into magnetic islands, depicted in figure 2.2. Whether given magnetic surface is rational or not, is found by the rotational transform ι, defined by

$$\iota = \frac{d\chi}{d\phi} \tag{2.19}$$

It should be noticed that the inverse of the rational transform also has a name, *safety factor*, which is extensively used in the study of tokamaks. The rotational transform is used more in the study of stellarators, but in any design it tells about the existence of a rational surface: whenever the rota-

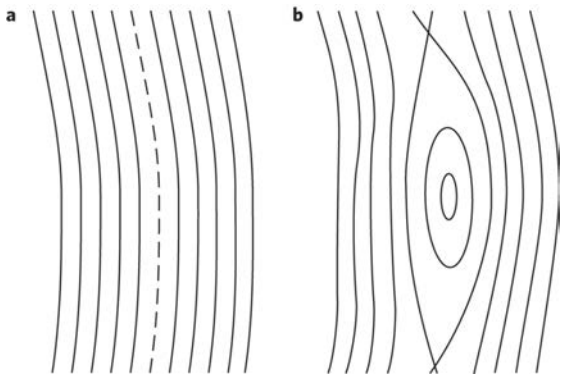

Figure 2.2: Comparison of an equilibrium with a) closed magnetic surfaces and b) with the presence of magnetic islands. Having a given surface which can resonate because of the rotational transform, when a perturbation is included, the development of magnetic islands is possible. If the equilibrium on the left were already on the lower energy state, then the equilibrium on the right would not be reached. Reprinted by permission from Macmillan Publishers Ltd: *Nature Physics* (Ongena & Ogawa [77]), copyright (2016).

tional transform has a rational value of 2π there is a rational surface. This is more easily expressed by the iota-bar quantity $\iota = \iota/2\pi$, therefore we can express the rational surfaces as

$$\iota = \frac{n}{m} \quad . \tag{2.20}$$

2.3 Magnetic islands and stochastic regions

Magnetic islands form in vacuum fields due to the departure of 3D fields from toroidal axisymmetry[15,73,102]. They first appear at the locations with lower-order rational values of the rotational transform. That is, where $\iota = n/m$, with low values of integers m and n. The width of these islands depends on the amplitude of the departure and the local magnetic shear. That is, how quickly the rotational transform changes as one moves from one surface to another. Vacuum magnetic islands can be avoided by careful design, or kept on purpose, as happens in the case of the use of island divertors[34] or of island transport barriers[21]. Magnetic islands do also develop inside the confined plasma, typically because of the currents that flow in the plasma. If these currents contain resonant components —i.e., a significant amplitude at the m, n Fourier mode at the location of the $\iota = n/m$ magnetic surface—, any finite resistivity may lead to the opening up of a magnetic island. Clearly, ideal MHD theory does not allow for this since it is a model with zero resistivity . Again, the width of the magnetic islands depends on the amplitude of the Fourier harmonic and the local magnetic shear, being in many cases too small to be of relevance. One can also force the opening of magnetic islands by introducing large resonant perturbations from the outside, using coils (see for example Evans[31], Fitzpatrick & Hender[35]). This is the path followed to pursue ELM active control in tokamaks, for instance.

In ideal MHD, rational surfaces cannot break open to form magnetic islands, except in the pres-

ence of resistivity (which is not ideal MHD anymore). Instead of the island formation, in ideal MHD a current sheet is developed on the rational surface as part of the solution. This current sheet is only a created mechanism, in reality rational surfaces would find their way to break open, given that the state they're in is unstable or has higher energy than the state where magnetic islands are present. Having a resonant perturbation and some resistivity, an associated tearing mode develops, breaking the closed magnetic field lines and leading to the formation of the island structure. The size of the island structure depends on the magnitude of the perturbation. It is important to stress that this tearing mode will only emerge or act if the energy of the state with magnetic islands is lower than the energy of the no-islands equilibrium.

While resistivity is needed for the reconnection required for the magnetic island formation, the surface-breaking driving mechanism is somewhat different for stellarators (3D MHD equilibria) and for tokamaks (2D MHD equilibria)[83,102]. In 3D MHD equilibria the plasma currents (mainly, diamagnetic and Pfirsch-Schlüter currents) are basically the ones which create the perturbations to the magnetic field which end up breaking a rational surface, whenever the perturbation is resonant. In 2D and 1D (slab geometries) equilibria, the surfaces may break due to the presence of tearing instabilities, which come up due to resistive effects in the plasma.

The formation of magnetic islands implies the presence of closed flux surfaces nested around a separate magnetic axis, which is generally located at the corresponding rational surface. This means that there is plasma which is limited to the volume of the island. Clearly the presence of plasma means that energy is confined within this volume and, depending on the location of the island, this may undermine the chances for achieving the fusion reaction. With the presence of plasma there is also current, temperature and pressure profiles within the island structures. Generally the temperature profiles inside magnetic islands flatten due to transport processes. As mentioned before, the importance of the islands' effects depend on the location and width of the island. Nowadays the islands can be somewhat controlled through RF current drive, which attempts to compensate part of the divergent current sheet at the rational surface, therefore they do not pose such a big problem when it comes to confinement.

One important characteristic of islands is that heat is transferred rapidly across them, so they may be useful to direct heat to a desired target, especially in the case of stellarators[59]. They may also be useful for driving currents in the core[25] and for mitigating edge localised modes (ELMs)[32].

When magnetic islands are too closely packed, they can lead to stochasticity. How densely packed they need to be is quantified in terms of the so-called Chirikov criterion[23]. In stochastic regions, magnetic field lines do not close on themselves or cover a surface. Instead, they ergodically fill a volume. Transport processes along field lines then lead to flattened profiles across stochastic regions, which makes it important to avoid them.

A *tearing mode* is called so because it is responsible for the tear of magnetic field lines.

Magnetic islands and stochastic regions in magnetically confined plasmas will play a central role in this work. The numerical tool that we will use to study them is SIESTA or, more precisely, a version of SIESTA expanded to be able to deal with free-plasma-boundary problems. We will introduce SIESTA, among other MHD tools, in the next chapter.

3

Numerical Solution of 3D ideal MHD equilibria: VMEC and SIESTA

Ideal MHD constitutes a simple model for the description of hot collisionless plasmas in the presence of a magnetic field, particularly useful for the purpose of describing plasmas in the core of the experiments of magnetic confinement fusion. The model has been solved numerically through the use of different methods throughout the history of magnetic confinement fusion research (see for example Bauer et al.[6], Callen & Dory[19], Chodura & Schlüter[24], among many others). The individuality of the research centres at the beginning of fusion research led to most laboratories developing their own code to solve the ideal MHD equations, both in their time-dependent and equilibrium versions.

One of the most important codes which has survived the passing years is the Variational Moments Equilibrium Code (VMEC)[50,51,52,53,56]. This is a 3D equilibrium code, which was developed at the Oak Ridge National Laboratory, in Tennessee, USA. It has been improved over time and has now reached the point of being the most widely used. As we shall see later in this chapter, VMEC assumes nested flux surfaces, which means that in the code there is no possibility for magnetic surfaces to break open and form other magnetic structures like magnetic islands.

For the analysis of scenarios where magnetic surfaces are able to break open, other codes have been developed, e.g. PIES[84], HINT2[92] and SIESTA[54] among others. SIESTA —Scalable Iterative Equilibrium Solver for Toroidal Applications— was developed in the same laboratory in Oak Ridge as VMEC, which means that the team developing it had plenty of experience with VMEC and the process of developing a 3D code able to analyse magnetic islands and stochastic regions was a natural step for them. Thanks to this great advantage, SIESTA takes the solution found by VMEC as a

first approximation and, as will be detailed later on, lets the system relax to search for nearby equilibrium solutions in which magnetic islands or stochastic regions might be present. This process makes SIESTA a code which is rather fast and robust.

In this chapter, details of both codes will be discussed. In section 3.1 the coordinate system used in both codes will be introduced, then section 3.2 deals with the details of VMEC and section 3.3 with the details of SIESTA. Both codes are iterative solvers that attempt to improve upon an initial solution, with the guiding principle of minimising its potential energy in the presence of some conservation constraints. While VMEC is a purely ideal MHD code, SIESTA artificially introduces a finite resistivity in the first few iterations of the iterative procedure to allow for the break-up of the magnetic surfaces and to accelerate the energy dissipation. The final solution of both codes is a solution to the ideal MHD equations explained in chapter 2.

3.1 Coordinate system

3.1.1 Basic definitions

Before going into the details of the coordinate system used, it is worth reminding the reader about some basic definitions of curvilinear coordinates. The position vector $\mathbf{r}$ is normally expressed in the cartesian or cylindrical base as

$$\begin{aligned}\mathbf{r} &= x\mathbf{e}_x + y\mathbf{e}_y + z\mathbf{e}_z \\ &= R\cos\varphi\mathbf{e}_x + R\sin\varphi\mathbf{e}_y + z\mathbf{e}_z \\ &= R\mathbf{e}_r + z\mathbf{e}_z\end{aligned}$$

In order to be able to map quantities from a flux coordinate system to the more normal cartesian or cylindrical systems, we need to find the basis of flux coordinates. The covariant and contravariant basis vectors for a given base $(u_1,\ u_2\, u_3)$ are given, generically by

$$\mathbf{e}_i \equiv \frac{\partial \mathbf{r}}{\partial u_i} \qquad\qquad \mathbf{e}^i \equiv \nabla u_i \quad , \tag{3.1}$$

and they can be related by the expression

$$\mathbf{e}^i \;=\; \frac{1}{\sqrt{g}}\mathbf{e}_j \times \mathbf{e}_k\, \epsilon_{ijk} \;=\; \frac{1}{\sqrt{g}}\frac{\partial \mathbf{r}}{\partial u_j} \times \frac{\partial \mathbf{r}}{\partial u_k}\, \epsilon_{ijk} \tag{3.2}$$

where the Jacobian $\sqrt{g}$ is given by

$$\sqrt{g} = \mathbf{e}_1 \times \mathbf{e}_2 \cdot \mathbf{e}_3 \tag{3.3}$$

and the symbol ϵ_{ijk} represents the Levi-Civita symbol, giving the permutation order on the multipli-

cation.

The metric elements will also be needed:

$$g_{ij} = \mathbf{e}_i \cdot \mathbf{e}_j \qquad\qquad g^{ij} = \mathbf{e}^i \cdot \mathbf{e}^j \tag{3.4}$$

They will be helpful for converting from contravariant to covariant vectors via the equalities

$$\mathbf{e}^i = g^{ij}\mathbf{e}_j \qquad\qquad \mathbf{e}_i = g_{ij}\mathbf{e}^j \quad . \tag{3.5}$$

3.1.2 Finding the right coordinate system

In order to solve the problem at hand we will follow the rule generally used in physics, i.e. we first need to find or define a coordinate system in which the problem can be easily described. Let us start by stating one more time the equations we need to solve, equations (2.14):

$$\mathbf{J} \times \mathbf{B} = \nabla p \tag{2.14a}$$

$$\frac{1}{\mu_0}\nabla \times \mathbf{B} = \mathbf{J} \tag{2.14b}$$

$$\nabla \cdot \mathbf{B} = 0 \tag{2.14c}$$

As the reader may remember, if we applied a scalar product of $\mathbf{B}$ on equation (2.14a) we obtain

$$\mathbf{B} \cdot \nabla p = 0 \quad ,$$

which means that there are no pressure gradients along the magnetic field lines. This is generally interpreted as the fusion relevant plasmas being arranged in nested flux surfaces, on which the pressure is constant.

A critical point on VMEC's scheme lies on the definition of the coordinates as a function of the magnetic fluxes. Knowing that the fluxes (poloidal χ and toroidal ϕ) are functions which are constant at the magnetic surfaces aforementioned and therefore independent of other quantities, it is possible to write the magnetic field in contravariant form as follows:

$$\begin{aligned} \mathbf{B} &= \nabla\zeta \times \nabla\chi + \nabla\phi \times \nabla\theta^* \\ &= B^\theta \mathbf{e}_\theta + B^\zeta \mathbf{e}_\zeta \end{aligned} \tag{3.6}$$

Because the fluxes are only dependent on the magnetic surface label, which we call ρ, i.e. $\chi_{(\rho)}$ and

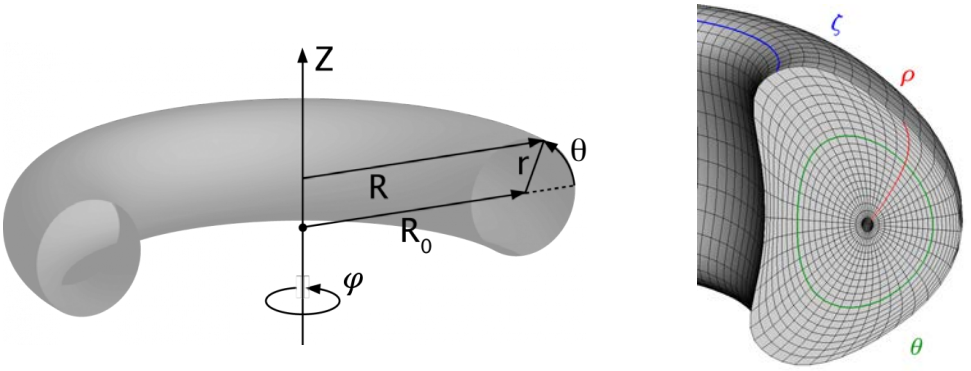

(a) General toroidal coordinates.

(b) Example of VMEC coordinates.

Figure 3.1: Left: The simple toroidal coordinate system is shown along with the cylindrical coordinate system, both generally used for the analysis of toroidal machines. There are four quantities used to describe a toroidal system: the major radius R_0 which is a parameter, the minor radius r, the poloidal angle θ and the toroidal angle φ. **Right:** an example of the VMEC coordinate system is shown, which are the flux coordinates presented in this section, for the D3D device, which is a tokamak. The quantities describing the coordinate system are the radial flux label ρ, the poloidal flux angle θ and the poloidal angle φ, which corresponds to the poloidal angle in figure 3.1a.

$\phi_{(\rho)}$ such that

$$\begin{aligned} \nabla\chi &\sim \mathbf{e}^{\rho} \\ \nabla\phi &\sim \mathbf{e}^{\rho} \end{aligned} \quad ,$$

they allow us to define the surface label. In this way, ρ is defined to be zero at the magnetic axis, where $\chi = 0$, and $\rho = 1$ at the border of the plasma. This means that the surface label ρ can be taken as the normalisation of the toroidal flux ϕ/ϕ_{edge} to its value at the edge. This is the case in VMEC, but in SIESTA, for reasons explained below, the square root of ρ is taken as a radial label. In principle, the surface label could be defined via either of the magnetic fluxes. Although in general the toroidal flux is the one used to define the radial flux coordinate, in the case of reverse field pinch (RFP) machines, the toroidal magnetic field changes its direction, causing the toroidal flux not to have its maximum at the edge, having to define the radial flux label with the poloidal magnetic flux[95]. Due to the definition of the surface label, the flux defining it must increase monotonically, which is generally the case of the toroidal flux, except in the aforementioned RFPs, for which the poloidal flux is taken to define the radial flux label.

The angles θ and ζ define the poloidal and toroidal angles, as shown in figure 3.1b, defining the system (ρ, θ^*, ζ) which will be used for the problem at hand. In VMEC, ζ is chosen to be the same as the toroidal angle φ. As for the poloidal angle in eq. (3.6), it is defined as

$$\theta^* = \theta + \lambda_{(\rho,\theta,\zeta)}$$

where λ is a re-normalisation factor called stream function which provides some flexibility for the definition of the poloidal coordinate. This convention also implies that the coordinate system has left-handed orientation, causing the Jacobian to be negative.

The formulation of $\mathbf{B}$ as in equation (3.6) satisfies both the requirement that there is no magnetic monopoles and the principle of nested magnetic surfaces ($\mathbf{B} \cdot \nabla p = 0$).

3.1.3 Relating the coordinate systems

It is clear that expressing quantities in cylindrical coordinates is not a problem, as a matter of fact it is easier for our understanding to have the quantities in that coordinate system since we can grasp what this physically looks like. Nevertheless, as we mentioned before, it is easier to solve the system of equations in a coordinate system where the quantities are expressed in a simple way. While, for example, in cylindrical coordinates the magnetic field vector would need the three components to be described, in flux coordinates only two components are needed.

In order to be able to express the vectorial quantities in flux coordinates, it is necessary to find the transformation relations between $(\mathbf{e}^r, \mathbf{e}^z, \mathbf{e}^\varphi)$ and $(\mathbf{e}^\rho, \mathbf{e}^\theta, \mathbf{e}^\zeta)$. Knowing that $\mathbf{e}^\mathbf{i} \equiv \nabla u_i$, we can easily find that

$$\mathbf{e}^r = \frac{\partial R}{\partial \rho}\mathbf{e}^\rho + \frac{\partial R}{\partial \theta}\mathbf{e}^\theta + \frac{\partial R}{\partial \zeta}\mathbf{e}^\zeta \tag{3.7a}$$

$$\mathbf{e}^z = \frac{\partial z}{\partial \rho}\mathbf{e}^\rho + \frac{\partial z}{\partial \theta}\mathbf{e}^\theta + \frac{\partial z}{\partial \zeta}\mathbf{e}^\zeta \tag{3.7b}$$

$$\mathbf{e}^\varphi = \frac{\partial \varphi}{\partial \rho}\mathbf{e}^\rho + \frac{\partial \varphi}{\partial \theta}\mathbf{e}^\theta + \frac{\partial \varphi}{\partial \zeta}\mathbf{e}^\zeta = \mathbf{e}^\zeta \quad . \tag{3.7c}$$

The covariant directional vectors in flux coordinates, following the definition in equation (3.1), are given by

$$\mathbf{e}_\rho = R_\rho \mathbf{e}_r + z_\rho \mathbf{e}_z \tag{3.8a}$$

$$\mathbf{e}_\theta = R_\theta \mathbf{e}_r + z_\theta \mathbf{e}_z \tag{3.8b}$$

$$\mathbf{e}_\zeta = R_\zeta \mathbf{e}_r + z_\zeta \mathbf{e}_z + R\mathbf{e}_\varphi \quad . \tag{3.8c}$$

It is also useful to have the contravariant vectors of the flux coordinate basis, which can be com-

puted by using the equality $\sqrt{g}\mathbf{e}^{\mathbf{i}} = \mathbf{e}_{\mathbf{j}} \times \mathbf{e}_{\mathbf{k}}$ (or inverting the relations (3.7)),

$$\mathbf{e}^{\rho} = \frac{1}{\sqrt{g}}\left[-Rz_{\theta}\mathbf{e}^{r} + RR_{\theta}\mathbf{e}^{z} + (R_{\zeta}z_{\theta} - R_{\theta}z_{\zeta})\mathbf{e}^{\varphi}\right] \tag{3.9a}$$

$$\mathbf{e}^{\theta} = \frac{1}{\sqrt{g}}\left[Rz_{\rho}\mathbf{e}^{r} - RR_{\rho}\mathbf{e}^{z} + (R_{\rho}z_{\zeta} - R_{\zeta}z_{\rho})\mathbf{e}^{\varphi}\right] \tag{3.9b}$$

$$\mathbf{e}^{\zeta} = \frac{1}{R}\mathbf{e}^{\varphi} \qquad , \tag{3.9c}$$

where the Jacobian is $\sqrt{g} = R(R_{\theta}z_{\rho} - R_{\rho}z_{\theta})$, as given by equation (3.3).

One can also invert equalities (3.8) to obtain the covariant (r, z, φ) directional vectors as a function of the flux basis vectors:

$$\mathbf{e}_{r} = \frac{R}{\sqrt{g}}\left(-z_{\theta}\mathbf{e}_{\rho} + z_{\rho}\mathbf{e}_{\theta}\right) \tag{3.10a}$$

$$\mathbf{e}_{z} = \frac{R}{\sqrt{g}}\left(R_{\theta}\mathbf{e}_{\rho} - R_{\rho}\mathbf{e}_{\theta}\right) \tag{3.10b}$$

$$\mathbf{e}_{\varphi} = \frac{1}{\sqrt{g}}\left[\left(R_{\zeta}z_{\theta} - R_{\theta}z_{\zeta}\right)\mathbf{e}_{\rho} + \left(R_{\rho}z_{\zeta} - R_{\zeta}z_{\rho}\right)\mathbf{e}_{\theta} + \left(R_{\theta}z_{\rho} - R_{\rho}z_{\theta}\right)\mathbf{e}_{\zeta}\right] \tag{3.10c}$$

With equalities (3.7) – (3.10) it is possible to find the relation between any co- or contravariant component of a given vector $\mathbf{F}$ and the unit vectors in any of the two coordinate systems, through the relations

$$F^{i} = \mathbf{F}\cdot\mathbf{e}^{i} \qquad\qquad F_{i} = \mathbf{F}\cdot\mathbf{e}_{i} \qquad . \tag{3.11}$$

3.1.4 Spectral representation

In both codes, a spectral representation of the quantities is assumed on the angular quantities, taking advantage of the periodicity of the poloidal and toroidal angles[53]. Stellarator symmetry[28,67] is assumed in SIESTA, for now. VMEC does not assume stellarator symmetry, nevertheless it can be run in a stellarator-symmetry-mode, so to say. The fact that a geometry possesses stellarator symmetry means that the geometry is symmetrical under the transformation $(\rho, \theta, \zeta) \rightarrow (\rho, -\theta, -\zeta)$, i.e.:

$$R_{(\rho,\theta,\zeta)} = R_{(\rho,-\theta,-\zeta)}$$
$$z_{(\rho,\theta,\zeta)} = -z_{(\rho,-\theta,-\zeta)}$$

Notice that this is the same as evaluating any quantity $f_{(R,\varphi,z)}$ in cylindrical coordinates at the points $(R, -\varphi, -z)$ instead. The quantity f is then considered to be symmetrical if $f_{(R,\varphi,z)} = f_{(R,-\varphi,-z)}$

or asymmetrical if $f_{(R,\varphi,z)} = -f_{(R,-\varphi,-z)}$. This symmetry is taken advantage of in Fourier representation through the description of even and odd quantities: those quantities which are symmetrical can be described by using a cosine series (even function) and those which are asymmetrical are described through a sine series (odd function). For, example, the cylindrical mesh is described as:

$$R_{(\rho,\theta,\zeta)} = \sum_{m=0}^{M} \sum_{n=-N}^{N} R_{m,n\,(\rho)} \cos(m\theta + n\zeta) \tag{3.12a}$$

$$z_{(\rho,\theta,\zeta)} = \sum_{m=0}^{M} \sum_{n=-N}^{N} z_{m,n\,(\rho)} \sin(m\theta + n\zeta) \qquad , \tag{3.12b}$$

description in which stellarator symmetry is inherent. The stream function can also be expressed in spectral representation, knowing that it is an odd function, as

$$\lambda_{(\rho,\theta,\zeta)} = \sum_{m=0}^{M} \sum_{n=-N}^{N} \lambda_{m,n\,(\rho)} \sin(m\theta + n\zeta) \qquad . \tag{3.13}$$

An important note must be done at this point: there is a small difference in the way SIESTA and VMEC use the spectral representation. In VMEC the argument of the trigonometric functions is $(m\theta - n\zeta)$*, while for SIESTA it is* $(m\theta + n\zeta)$*. This is just a matter of preference but it is important to have in consideration due to the derivatives involved in the problem being solved.*

This defines two spaces in which quantities are treated: Fourier and real spaces. The Fourier space is completely characterised by the flux surface label ρ —also referred here as the radial coordinate— and the poloidal and toroidal modes, whose ranges are

$$\begin{aligned} \text{poloidal modes:} \quad & 0 \leq m \leq M \\ \text{toroidal modes:} \quad & -N \leq n \leq N \qquad . \end{aligned}$$

On the other hand, the real space is described by ρ and the two angles θ and ζ when using the flux coordinates, which are geometrical angles (in their coordinate system), or z and φ when the cylindrical coordinates are used. The comparison of working on one space or the other is shown in figure 3.2.

In both systems the limitation of the resolution of the problem is given by the amount of mesh points taken. Nevertheless, it is important to notice that independently of how many mesh points are considered in real space, if the number of modes considered is not enough to represent the variability of the real space mesh or of the quantities in real space, then mistakes are going to be made in any case. The good thing about the spectral method is that for having a good resolution, the size of the mesh needed is much smaller than in real space.

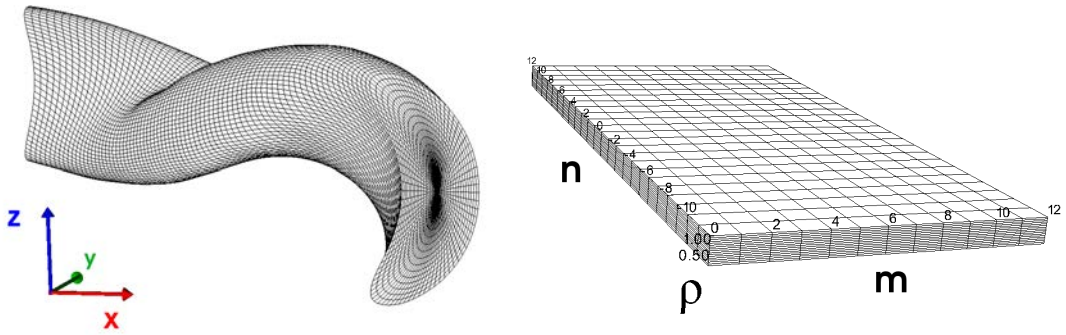

(a) Numerical mesh in real space.

(b) Numerical mesh in Fourier space.

Figure 3.2: Comparison between the real space mesh (left) and the Fourier space mesh (right). It is clear that treating the problem in an adequate mesh brings advantage on the representation of quantities.

Taking a look at Nyqvist's anti-aliasing theorem, the lower limit for the number of [sample] points needed in order to describe correctly a system transformed in Fourier space, is double the maximum frequency present in the system, which in our case is represented by the mode numbers. This means that if for having a good resolution of the quantity X in real space one needs a minimum of n_x mesh points, then in Fourier space it would suffice with $m = n_x/2$.

3.2 VMEC

3.2.1 Physical model

As mentioned before, the goal of VMEC is to solve the ideal MHD equations, and it does so by minimising the total energy of a confined plasma in a given domain Σ

$$W = \int_{\Sigma} \left(\frac{B^2}{2\mu_0} + \frac{p}{\gamma - 1} \right) d^3r \tag{2.15}$$

From equation 3.6 and from the definition of θ^* it is possible to express the poloidal and toroidal contravariant components of the magnetic field as

$$B^{\theta} = \frac{1}{\sqrt{g}} \left(\chi' - \phi' \frac{\partial \lambda}{\partial \zeta} \right) \tag{3.14}$$

$$B^{\zeta} = \frac{\phi'}{\sqrt{g}} \left(1 - \frac{\partial \lambda}{\partial \theta} \right) \quad , \tag{3.15}$$

and the radial component is null, which is the principle of nested magnetic surfaces.

If we compute the variation of the energy (therefore the name of the code) with respect to a pa-

rameter t, then we can write the result as

$$\frac{dW}{dt} = -\int F_i \frac{\partial x_i}{\partial t} d^3\alpha - \int F_\lambda \frac{\partial \lambda}{\partial t} d^3\alpha - \int_{\rho=1} |\sqrt{g}| \frac{d\rho}{dx_i} \left(\frac{|\mathbf{B}|^2}{2\mu_0} + p \right) \frac{dx_i}{dt} d\theta d\zeta \tag{3.16}$$

where the variables x_i refer to the cylindrical triad (R, φ, Z) and the variables α refer to the flux variables, such that the volume element $d^3\alpha = d\rho d\theta d\zeta$. Here, the functions F_i, where $i = (R, \varphi, Z)$, are defined by

$$\begin{aligned} F_i = &- \frac{\partial}{\partial \alpha_j} \left[|\sqrt{g}| \frac{\partial \alpha_j}{\partial x_i} \left(\frac{|\mathbf{B}|^2}{2\mu_0} + p \right) \right] \\ &+ \frac{|\sqrt{g}|}{\mu_0} \nabla \cdot \left[(\Lambda_i \mathbf{B} \cdot \nabla x_i) \, \mathbf{B} \right] \\ &+ \delta_{i1} \frac{|\sqrt{g}|}{R} \left(\frac{|\mathbf{B}|^2}{2\mu_0} + p - \frac{R^2 (\mathbf{B} \cdot \nabla \varphi)^2}{\mu_0} \right) \quad , \end{aligned} \tag{3.17}$$

where summation over the index j is assumed —here and henceforth—, also $\Lambda_1 = \Lambda_3 = 1$, $\Lambda_2 = R^2$ and

$$F_\lambda = \phi' \frac{|\sqrt{g}|}{\mu_0 \sqrt{g}} \left(\frac{\partial B_\zeta}{\partial \theta} - \frac{\partial B_\theta}{\partial \zeta} \right) \quad . \tag{3.18}$$

The last term in equation 3.16 corresponds to the change of energy due to the movement of the boundary, which in the case of VMEC can vary considerably when ran in the free-boundary mode.

The previous system of equation simplifies when Fourier harmonics are taken for the angular variables θ and φ. Redefining the index i in F_i and x_i so that it iterates over (R, λ, z) in that order, we can introduce the complex Fourier harmonics X_j^{mn}, so that the spectral representation can be compactly written as

$$x_j = \sum_{m,n} X_{j\,(\rho)}^{mn} \exp\left[i(m\theta - n\zeta) \right] \quad , \tag{3.19}$$

and the harmonics for the F_i functions are defined as

$$F_j^{mn} = \frac{1}{V'} \iint F_j \exp\left[-i(m\theta - n\zeta) \right] d\theta d\zeta \quad . \tag{3.20}$$

With these two definitions the energy variational can be written as

$$\frac{dW}{dt} = -\int (F_j^{mn})^* \frac{\partial X_j^{mn}}{\partial t} dV \quad , \tag{3.21}$$

where the volume elements relate by $dV = V' d\rho$. The harmonics F_j^{mn} represent now the varia-

tional forces which need to vanish for the system to reach equilibrium.

3.2.2 Method

It is know that the equilibrium state of the system corresponds to a minimum energy state because of the lower bound (due to flux and mass conservation) and because it is positive definite for $\gamma > 1$ (Kruskal & Kulsrud [63]). Then, in order to find the state of minimum energy, it is necessary to follow the path of continuous descent of dW/dt. Having such a complex expression for the energy variational, this is not an easy task. A Ritz method is applied in VMEC, where the trial functions for X_j^{mn} should lead to a solution. In the original paper Hirshman & Whitson [56] it is argued that the fastest rate of decrease obtained for the descent path is given by the trial function

$$\frac{dX_j^{mn}}{dt} = F_j^{mn}$$

In a later research, Hirshman & Betancourt [50] explain that the expressions for F_j^{mn} are non-linear functions of $\mathbf{X}$ and its spatial derivatives. The authors then apply a Richardson scheme in order "to solve the simultaneous coupled non-linear equations $F_j^{mn}(\mathbf{X}) = 0$ for the coordinate transform amplitudes X_j^{mn}", obtaining the following expression for the path of minimum descent

$$\frac{d^2X_j^{mn}}{dt^2} + \frac{1}{\tau}\frac{dX_j^{mn}}{dt} = F_j^{mn} \quad . \tag{3.22}$$

Here, the optimum frequency τ_{op} is given by

$$\tau_{op} = -\frac{d}{dt}\left(\int |F|^2 dV\right)$$

The conversion of the descent path equations to hyperbolic equations further increases the descent rate, accelerating the convergence of the problem. The details are out of this works' scope, but the curious reader is encouraged to read the original paper of VMEC [56] and its sequels Hirshman & Betancourt [50], Hirshman & Meier [53]. The reader will also find more technical details about the numerical scheme used in the code, here some of its characteristics, which are considered relevant to this work, will be stated.

Boundary conditions

The quantities are defined in two radial meshes in order to avoid discontinuities at the axis and at the $\rho = 1$ boundaries when computing derivatives. Namely, one mesh is defined as the *full radial*

mesh:

$$\Delta\rho = \frac{1}{N_\rho - 1} \qquad \Rightarrow \qquad \rho_i = (i-1)\Delta\rho \quad ; \quad i = 1, \cdots, N_\rho \tag{3.23}$$

and the other is defined as the *half radial mesh*:

$$\rho_{i+1/2} = \frac{\rho_i + \rho_{i+1}}{2} \tag{3.24}$$

The main objective of having the half-mesh points is to avoid the axis, where our functions are prone to diverge. In order to ensure continuity and well defined quantities, the R_{mn} and Z_{mn} coefficients are required to tend to zero as $\rho \to 0$ for $m \neq 0$. Furthermore, for the elements corresponding to $m = 0$, it is required that they behave as ρ, i.e. they quickly tend to zero at the axis. This ensures not only that the mesh quantities are finite at the axis, but also that their derivatives —and therefore the metric elements— are continuous.

The angular differentiation is much easier since there are analytical expressions for the derivatives of the Fourier expressions of the quantities defined throughout the code.

The other boundary, $\rho = 1$, is related to the external shape of the plasma surface. VMEC operates in two possible modes: fixed- or free-boundary. In the case of the fixed-boundary operation, the surface's shape is kept constant throughout the iteration process, which means that the Fourier coefficients $R_{mn\,(1)}$ and $Z_{mn\,(1)}$ are prescribed and kept constant. When prescribing the shape of the last surface in fixed-boundary mode, the general methods for obtaining the last surface's shape are: through a ray-tracing procedure on the vacuum magnetic field or from experimental measurements.

On the other hand, for the free boundary case the force equations

$$\nabla R \cdot (\mathbf{J} \times \mathbf{B} - \nabla p) = 0 \qquad\qquad \nabla Z \cdot (\mathbf{J} \times \mathbf{B} - \nabla p) = 0$$

are solved at $\rho = 1$ to obtain $R_{mn\,(1)}$ and $Z_{mn\,(1)}$. The solution for these coefficients is obtained using the same variational formulation as the one used for solving the inside of the plasma. This is of importance because then the force equations derived are consistent to those in the interior of the plasma. It may sound as a redundant aspect, though there are some cases where due to diverse reasons the edge condition is not computed consistently to the inner solution, see for example Bauer et al. [6].

3.2.3 Limitations of VMEC

As mentioned at the beginning of the chapter, VMEC has resisted the passing of the years due to the great job it does at a low computational price. A solution for a fusion relevant problem can take from a few seconds to a few minutes running in a single processor of a standard laptop (Intel i5 processor, for example), depending on the complexity of the geometry of the problem. So, truthfully

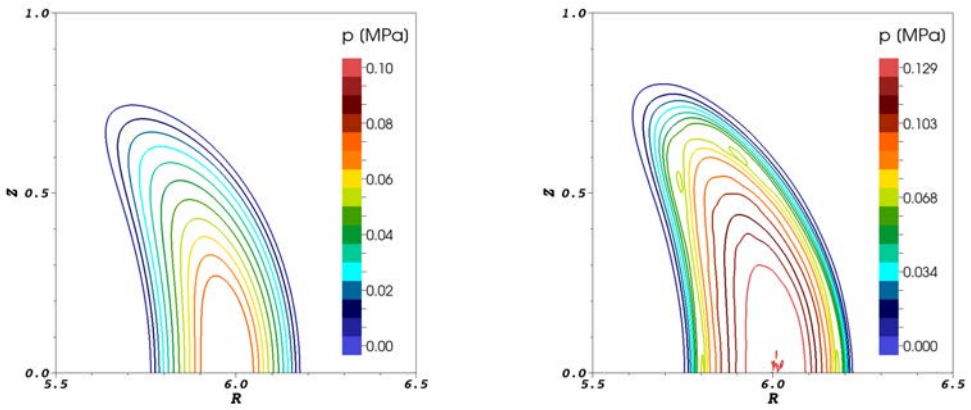

Figure 3.3: Example of pressure variation for an equilibrium of the W7-X device. **Left:** the ideal case where the pressure is maximum at the axis of the plasma and it reduces monotonically on the way to the edge. This is a solution of the VMEC code, though not necessarily the case in real experiments. **Right:** An example of an equilibrium, solved by SIESTA, where the pressure contours are not nested as assumed by VMEC.

speaking, VMEC does a great job at what it does.

The limitations then come up on *what* it does. VMEC solves ideal MHD equations with the assumption of nested magnetic surfaces. This means that the equality $\mathbf{B} \cdot \nabla p = 0$ has been interpreted assuming the ideal case of plasmas in fusion. Notice that for this equation

$$B^{\rho}\frac{\partial p}{\partial \rho} + B^{\theta}\frac{\partial p}{\partial \theta} + B^{\zeta}\frac{\partial p}{\partial \zeta} = 0 \tag{3.25}$$

there are infinite combinations which can fulfil the equality. The assumption of the existence of nested closed magnetic flux surfaces, allowed us to define ρ as the radial flux coordinate label and to have by definition a magnetic field with no radial component B^{ρ}. As a consequence the pressure became a function only of the radial label, so that ∇p only has a radial component, satisfying the previous equation. This is an ideal case, which is generally not true, although it makes a great job when describing the global behaviour of plasmas.

In the presence of magnetic islands or stochastic regions, the magnetic flux cannot be defined as a flux coordinate. Or what is the same, one can use the numerical mesh of VMEC as a background mesh, but ρ no longer represents the magnetic flux. In the latter case $\mathbf{B}$ and p can take any set of values as long as equation 3.25 is satisfied.

The ideal case is pictured in figure 3.3. It can be seen that the core of the plasma is at high pressure and that it decreases monotonically towards the edge of the plasma, i.e. the pressure depends only on the flux radial coordinate. While as a first approximation it is possible to take this as a fact, there are certain equilibria which have complex plasma structures, being possible to have regions where pressure flattens, or where a different pressure distribution is present, e.g. flux-tubes. The

same equations of ideal MHD would still be valid, even in the presence of flux tubes, so there is no reason to force a calculation with $B^\rho = 0$

These flux tubes are what constitute the magnetic islands. An island is a tube that extends along the torus and eventually closes on itself. As such, the plasma inside of the tube will show a particular structure, having greater pressure at the centre of the tube and decreasing to the exterior values at the edge of the tube, in an ideal case. Other structures where the assumption of nested flux surfaces is not valid —such as ergodic regions— may develop in any given device.

There are relevant situations, however, where magnetic islands are expected and even, desired. They may appear as a result of instabilities (tearing modes, sawtooth, etc.) or introduced by design (island divertors or transport barriers). To provide ideal MHD equilibrium solutions in these cases, we need something other than VMEC. That is where SIESTA comes in.

3.3 SIESTA

The Scalable Iterative Equilibrium Solver for Stellarator Applications (SIESTA)[54] is a code which allows to analyse the ideal MHD equilibrium of three dimensional magnetically confined plasma devices. It relies on the VMEC code, which does the same with the assumption of nested magnetic flux surfaces, as explained in the previous section. SIESTA relies on the solution of VMEC as an approximation to its solution, but it allows for the development of radial structures, i.e. it does not impose any conditions on the radial magnetic field, thus searching for solutions for eq. 3.25 in a much larger solution space. This advantage results in the possibility of accessing lower-energy solutions that, in some cases, are closer to what is expected in the real world where magnetic island structures and stochastic regions may form.

Such a code becomes of utter importance specially when studying devices which are prone to the development of magnetic islands, or which have them included in their design, as is the case for the Wendelstein 7-X stellarator[7]. Tokamaks can naturally develop such structures due to the high plasma currents which create instabilities, so naturally SIESTA is also very useful when analysing the equilibrium conditions in tokamaks (see for example Canik et al.[20], Hirshman et al.[55]).

The importance and practicality of this code is still hindered by its lack of ease of use, although work is underway to ease things in the near future. Due to the type of the problem being solved, the user must find the appropriate parameters —if they exist— for running SIESTA so that it converges for the problem under study. This may sound trivial, but it is not always an easy task.

3.3.1 Physical model

The problem being solved, as in VMEC, is that of ideal MHD. The idea is the same as that of VMEC, i.e. to minimise the energy of a stationary plasma which is under the effect of a magnetic field **B** and is under a pressure p, so that the energy is given by equation 2.15. In this case the difference is that

there is a radial component of the magnetic field. As before we derive the equation, but this time we do it with respect to time. The reader might note that it is irrelevant to consider a time derivative since the energy equation under consideration corresponds to a plasma in static equilibrium, and that is partly correct. Part of the approach of SIESTA is to perturb an existent solution which is not yet in equilibrium but very close to it —the one coming from VMEC—. In order to let this perturbation "evolve" to a final equilibrium a time-like parameter is introduced, along with a numerical resistivity that should permit the topological rearrangement of structures, if they lead to reductions in the total energy, and that is switched off when an equilibrium solution is approached. The significance of these two factors will [hopefully] become clear to the reader in the next lines.

The time derivative of equation 2.15 results in

$$\frac{\partial W}{\partial t} = \int_{\Sigma} \left(\frac{1}{\mu_0} \frac{\partial B}{\partial t} + \frac{1}{\gamma - 1} \frac{\partial p}{\partial t} \right) d^3 r \qquad . \tag{3.26}$$

Here is where considering an almost instantaneous time evolution becomes handy. We now take Faraday's law for the evolution of the magnetic field

$$\frac{\partial B}{\partial t} = -\nabla \times \mathbf{E} \qquad , \tag{3.27}$$

and the particle conservation along with the adiabatic law

$$\frac{\partial p}{\partial t} = (\gamma - 1)\mathbf{v} \cdot \nabla p - \gamma \nabla \cdot (p\mathbf{v}) \qquad . \tag{3.28}$$

After a few lines of mathematical operations the time variance of the energy can be expressed as

$$\frac{\partial W}{\partial t} = \int \left[-\mathbf{E} \cdot \mathbf{J} + \mathbf{v} \cdot \nabla p \right] d^3 r - \oint \mathbf{S} \cdot d\mathbf{A}$$

where the current density $\mathbf{J}$ can be obtained from Ampere's law and

$$\mathbf{S} = \frac{\mathbf{E} \times \mathbf{B}}{\mu_0} + \frac{\gamma}{\gamma - 1} p\mathbf{v}$$

is the Poynting flux (first term on the r.h.s.) plus the kinetic flux (second term on the r.h.s.). This flux contribution can be neglected by considering appropriate boundary conditions. The resulting equation can be further transformed by making use of Ohm's law

$$\mathbf{E}' \equiv \mathbf{E} + \mathbf{v} \times \mathbf{B} = \eta \mathbf{J}$$

and the variation of W can be finally expressed as

$$\frac{\partial W}{\partial t} = -\int \left[\mathbf{v}\cdot(\mathbf{J}\times\mathbf{B}-\nabla p)+\eta J^2\right] d^3r \tag{3.29}$$

The displacement is defined as $\mathbf{v} = d\boldsymbol{\xi}/dt$, making F a function of ξ. Displacements are then sought that minimize the force as much as possible using a non-linear Newton method. The resistivity η is only introduced for the initial iterations in order to accelerate the energy dissipation. When the residual decreases below a certain threshold, then the resistivity is decreased as well, to the point of $\eta \to 0$. Therefore at the end of SIESTA's iterations then the system only becomes stationary when the force is balanced, i.e. when

$$\mathbf{F} = \mathbf{J}\times\mathbf{B}-\nabla p = 0 \tag{3.30}$$

One particular aspect to keep in mind is that SIESTA uses a radial label in flux coordinates which relates to the one used in VMEC by the following equality

$$s = \sqrt{\rho} \quad .$$

This change in the radial label happens mainly due to one reason: to avoid issues at the magnetic axis $\rho = 0$. Taking the square root of a small number, pushes the result away from zero, therefore if there were any radial mesh points close to the magnetic axis, these would be redistributed to a more external surface. This results in a visible difference when it comes to the radial mesh of the two codes: VMEC has an equidistant mesh in the radial direction in flux space while SIESTA has an accumulation of surfaces towards the edge of the flux radial mesh.

Besides this change the reader should keep in mind the difference in the Fourier representation discussed before.

3.3.2 Method

SIESTA's method is similar to that one of VMEC. In order to see this, it is necessary to get the energy variational to a similar form as equation 3.21. To do that, let us express the ideal MHD energy principle in flux coordinates as

$$W = \int \left[\frac{B^i B_i}{2\mu_0}+\frac{p}{\gamma-1}\right]|\sqrt{g}|dsd\theta d\zeta \tag{3.31}$$

for which, after some mathematical handling, the variational form can be expressed like

$$\delta W = \int \left[\frac{B_i \delta \sqrt{g} B^i}{\mu_0} + \delta p \right] ds d\theta d\zeta$$

Using equations 3.27 and 3.28 to obtain the variation of B and p and taking $\boldsymbol{\xi} = \mathbf{v}\Delta t$ as the perturbed displacement vector, the variations of B and p can be written as

$$\begin{aligned} \delta b^i =& \frac{\partial}{\partial x_j}(\xi^i b^j - \xi^j b^i) \\ \delta P =& -\gamma \frac{\partial (P\xi^j)}{\partial x_j} + (\gamma + 1)\sqrt{g}\xi^j \frac{\partial p}{\partial x_j} \end{aligned}$$

where the substitutions $b^i = \sqrt{g}B^i$ and $P = \sqrt{g}p$ have been made. The first term on the right hand side of the pressure equation makes no contribution to the energy variational integral 3.29 due to the boundary conditions, which will be explained in the next subsection. From here it is possible, after some mathematical manipulation and integrating the magnetic field terms by parts, to obtain a form of the energy variational which resembles the one obtained for the VMEC case:

$$\delta W = -\int \sqrt{g}\xi^i \cdot F_i \, ds d\theta d\zeta \tag{3.32}$$

where the covariant components of the force are given by

$$F_i = \epsilon_{ijk}\sqrt{g}J^i B^k - \frac{\partial p}{\partial x_i} \qquad . \tag{3.33}$$

The contravariant component of the current distribution is simply given by Ampere's law expressed in flux coordinates

$$\mu_0 \sqrt{g} J^i = \epsilon_{ijk} \frac{\partial B_j}{\partial x_k} \qquad .$$

Equation 3.32 is now clearly similar to eq. 3.21. Therefore the method used to minimise the energy is again the steepest descent method. Similarly as for VMEC, the steepest descent path is given by taking $\xi^i = \Pi^{ij} F_j$ for some positive-definite matrix Π, which leaves the energy variational principle finally expressed as

$$\delta W = -\int \Pi^{ij} F_i F_j \, ds d\theta d\zeta \tag{3.34}$$

Which has the same condition as for VMEC: δW vanishes only if the MHD force vanishes.

The matrix Π^{ij} is generally taken to be the metric tensor g^{ij} (technically, its inverse), so that the integral is done over $|F^2| = F^i F_j$. The metric tensor, besides being positive definite, is also symmetrical, which simplifies the analysis quite a bit. The descent method can be further accelerated if the

matrix Π is taken as a preconditioner for the Hessian matrix. On top of this, a shift in the eigenvalues of the preconditioner is needed in order to ensure its positive-definiteness. While VMEC's solution already provides a near equilibrium state, it is still possible to obtain an eigenvalue spectrum which contains both positive and negative eigenvalues —all should be negative when the solution is close to a stable equilibrium—, and some close to zero. This shift is reduced to zero as the force residual tends to zero, avoiding in this way a non-physical solution since the full Hessian is being considered towards the end of a simulation.

The eigenvalues shift resembles the way the resistivity is considered. Both help accelerate the convergence of the system and towards the end they are "turned off" so to say. The resistivity is there to help breaking the closed magnetic surfaces and accelerate the energy dissipation, while the eigenvalue shift is used purely to accelerate the convergence of the system while ensuring the validity of the preconditioner matrix to equation 3.32.

The fact of SIESTA taking VMEC' solution as a first approximation implies not only that it takes the solution of the pressure and magnetic field, but also the coordinate system to use it as a background fixed coordinate system (no need to recalculate the metric elements through the iteration process). Remember that the coordinate system found by VMEC is that of flux surfaces, so each flux radial mesh point represents a magnetic surface. Once in SIESTA however, these surfaces are no longer flux surfaces, but just the radial surfaces of the background numerical mesh. The advantage of this, as explained in section 3.1, is that SIESTA works in a coordinate system which describes a state close to the final equilibrium, i.e. the magnetic field is very easily representable and the variations are generally small —unless, of course, VMEC's solution is far from the final equilibrium.

Boundary conditions

For simplicity, SIESTA considers a perfect conductor at the $s = 1$ boundary, which through Faraday's law implies that the tangential components of the electric field vanish. Using this result in Ohm's law, this means that $\xi^s = 0$, making the total energy in the Poynting and kinetic fluxes zero. This condition also makes the radial pressure gradient at $s = 1$ to vanish.

In the axis, as explained by Aydemir & Barnes [2], there is the requirement that quantities at the axis are singled valued, both vectors and scalars. This results in the equalities

$$\frac{\partial p}{\partial \theta} = 0 \tag{3.35a}$$

$$\frac{\partial \mathbf{u}}{\partial \theta} = 0 \quad , \tag{3.35b}$$

for a generally complex vector $\mathbf{u}$. This in turn implies that

$$p_{(s=0)\,mn} = 0 \qquad \text{for } m \neq 0 \tag{3.36a}$$

$$u^{\zeta}_{(s=0)\,mn} = 0 \qquad \text{for } m \neq 0 \tag{3.36b}$$

$$u^{s}_{(s=0)\,mn} + imu^{\theta}_{(s=0)\,mn} = 0 \qquad \text{for } |m| = 1 \tag{3.36c}$$

$$u^{s}_{(s=0)\,mn} = 0 = u^{\theta}_{(s=0)\,mn} \qquad \text{for } |m| \neq 1 \quad . \tag{3.36d}$$

In SIESTA this translate into the $m = 1$ harmonic of the covariant s and θ force components being dominant near the magnetic axis, while for the toroidal component it is the $m = 0$ harmonic which becomes dominant.

3.4 Motivation for extending SIESTA

SIESTA is a very promising code, but its range of applicability is constrained, in its current form, to fixed-boundary-problems that only examine the region where the plasma is confined. There is a plethora of problems where the plasma edge, and the region between plasma and the first wall, are of interest. Examples are the use of 3D shaping of the plasma edge to improve stability, or the introduction of edge rationals to build an island divertor. These problems are outside of the reach of the fixed-boundary SIESTA. It is for that reason that the main goal of this thesis is to extend SIESTA to free-plasma-boundary problems and to prove its usefulness in addressing some of the situations mentioned above.

Part II

Free-Boundary SIESTA

The contents of this chapter were published in the Physics of Plasmas Journal by H. Peraza-Rodriguez, J. M. Reynolds-Barredo, R. Sanchez, J. Geiger, V. Tribaldos, S. P. Hirshman and M. Cianciosa under the name "Extension of the SIESTA MHD equilibrium code to free-plasma-boundary problems"[81]. It is reproduced here with the permission of AIP Publishing.

4

Building free-plasma-boundary SIESTA

ABSTRACT

SIESTA [S.P. Hirshman, R. Sanchez and C.R. Cook, Phys. Plasmas 18, 062504 (2011)] is a recently developed MHD equilibrium code designed to perform fast and accurate calculations of ideal MHD equilibria for three-dimensional magnetic configurations. Since SIESTA does not assume closed magnetic surfaces, the solution can exhibit magnetic islands and stochastic regions. In its original implementation SIESTA addressed only fixed-boundary problems. That is, the shape of the plasma edge, assumed to be a magnetic surface, was kept fixed as the solution iteratively converges to equilibrium. This condition somewhat restricts the possible applications of SIESTA. In this paper we discuss an extension that will enable SIESTA to address free-plasma-boundary problems, opening up the possibility of investigating problems in which the plasma boundary is perturbed either externally or internally. As an illustration, SIESTA is applied to a configuration of the W7-X stellarator.

4.1 Introduction

SIESTA is an iterative MHD equilibrium solver that looks for lower energy states starting from nearby equilibria with nested magnetic surfaces[54], being one of just a handful of MHD equilibrium codes[58,84,92] that does not assume the existence of magnetic surfaces. SIESTA uses the nested equilibrium solution found by the VMEC code[56] to provide: 1) a (fixed) background set of quasi-polar coordinates, (s_v, θ_v and ϕ_v), in which calculations are carried out, and 2) an initial guess for the equilibrium magnetic field and pressure fields to start the iterative search of an equilibrium solu-

tion. Here, $\phi_v = \phi$ is the geometrical toroidal angle; $\theta_v = \theta^*$, the non-geometrical poloidal angle that VMEC internally uses to maximize the compression of the harmonic content of the solution[53]; finally, $s_v = \sqrt{s}$, with s being the normalized magnetic toroidal flux that VMEC uses as radial coordinate.

SIESTA, as VMEC, is a spectral code in which the curvilinear components of all fields are expanded in Fourier series in the poloidal (θ_v) and toroidal (ϕ_v) angles. For the sake of simplicity, SIESTA currently assumes stellarator symmetry[28], so that all fields exhibit either cosine,

$$C(s_v, \theta_v, \phi_v) = \sum_{m=0}^{M} \sum_{n=-N}^{N} C_{mn}(s_v) \cos(m\theta_v + nN_p\phi_v) \quad , \tag{4.1}$$

or sine,

$$S(s_v, \theta_v, \phi_v) = \sum_{m=0}^{M} \sum_{n=-N}^{N} S_{mn}(s_v) \sin(m\theta_v + nN_p\phi_v) \quad , \tag{4.2}$$

symmetry, depending on the parity of the field of interest. The values of the harmonics of the three contravariant components of the magnetic field (i.e., B^{s_v} [sine parity], B^{θ_v} [cosine] and B^{ϕ_v} [cosine]) and the plasma pressure (p, cosine) are iteratively varied by SIESTA until it reaches a minimum of the total MHD energy integrated over the plasma volume,

$$W = \int \left[\frac{B^2}{2\mu_0} + \frac{p}{\gamma - 1} \right] dV \quad , \tag{4.3}$$

consistent with the imposed boundary conditions and MHD conservation laws for flux and mass. As it is well known, the MHD energy becomes quasi-stationary only when the ideal MHD force, $\mathbf{J} \times \mathbf{B} - \nabla p$, vanishes[36]. SIESTA looks for zeros of this nonlinear force, in terms of the plasma displacement vector, using an iterative nonlinear Newton method[54]. The use of the VMEC coordinate system ensures that the number of Fourier harmonics that need to be included in SIESTA is kept down to a minimum, improving considerably both the convergence of the Newton method and the overall performance of the code. In addition, the solution of the linear problem that appears at each step of the non-linear Newton method is also searched iteratively, combining Krylov and conjugate-gradient methods with accurate physics-based preconditioning to further accelerate convergence to the desired tolerance[54].

Another subtle aspect of SIESTA is that it does allow for a certain (and controlled) departure from ideal MHD during the iterative procedure. In purely ideal MHD codes with nested surfaces, magnetic islands (and the stochastic regions that may result from their superposition) are prevented from opening up by the formation of (parallel) current sheets at the resonant magnetic surfaces[9,68,69]. SIESTA allows for the diffusion of these resonant currents (and therefore, the violation of the frozen-flux theorem of ideal MHD) by interlacing the preconditioned ideal steps with a few resistive steps.

In real devices, the very small diffusivity makes this a very slow physical process, that is significant only at the current sheet region. SIESTA accelerates this process by artificially increasing the resistivity (and also, via the rescaling of the relevant eigenvalues done by the internal preconditioning), but its application during the iterative procedure is done in a way that the main (non-resonant) components are barely affected [More details about the use of resistivity can be found in the original SIESTA reference Hirshman et al.[54].].

As it was mentioned earlier, the original version of SIESTA was developed as a fixed-boundary code[54]. That is, its spatial domain is the plasma volume, whose boundary is defined by the isosurface $s_v = 1$. Boundary conditions are imposed at this boundary that ensure that, while the MHD energy is minimized, any plasma displacement considered always vanishes there. As a result, both the magnetic field and the plasma pressure remain fixed at the boundary during the iterative procedure, with B^s (since $s_v = 1$ is a magnetic surface) and p set to zero. There are however situations of relevance in which one would like to be able to calculate the changes to the plasma boundary caused by different actions. For instance, during the application of resonant magnetic perturbations close to the plasma edge, as those often used to try to control ELM activity in tokamak H-modes[31]. Or when unbalanced plasma currents appear in zero-current stellarators, driven for instance by external heating or the pressure gradient, as could be the case of the W7-X stellarator[7]. For that reason, this paper introduces a new methodology that enables SIESTA to perform free-plasma-boundary equilibrium calculations.

The paper is organized as follows. In Sec. 4.2, the fundamentals of the new approach are described. They include the extension of the calculation domain beyond the plasma edge, the construction of an adequate numerical mesh throughout the extended region (Sec. 4.2.1) and the construction of a proper initial guess, for both magnetic field (Sec. 4.2.2) and pressure (Sec. 4.2.3), over the extended domain. The extended capabilities of the new version of SIESTA are illustrated in Sec. 4.3, where we use it on a selected configuration of the W7-X stellarator. Then, some final conclusions will be drawn in Sec. 4.4.

4.2 Free-plasma-boundary extension procedure

In order to enable SIESTA to perturb the plasma boundary while looking for equilibrium solutions with lower MHD energy, the computational domain needs to be expanded so that the plasma boundary (the old $s_v = 1$) becomes an internal surface (that will probably cease to coincide with the $s_v = 1$ isosurface of the fixed background coordinate system). Although any volume that includes the plasma could be used, it seems natural to consider the volume inside the vacuum vessel of the device of interest (see Fig. 4.1). The strategy we will then follow is to consider the boundary of the extended volume as a new fixed boundary, at which suitable boundary conditions will be imposed. In this way, SIESTA can be run in fixed boundary mode with respect to the extended volume, *while*

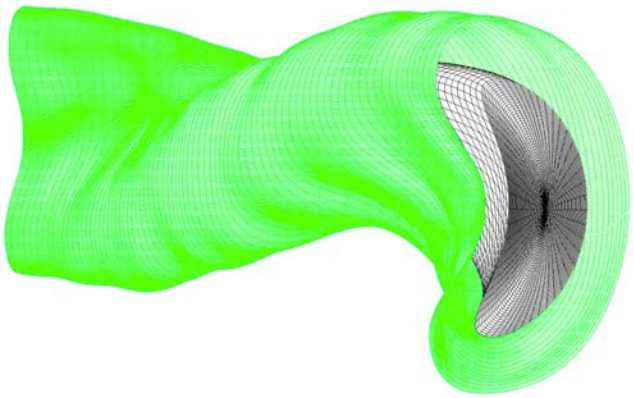

Figure 4.1: Illustration of the extended domain used by SIESTA for the W7-X stellarator runs that will be discussed in Sec. 4.3. (A smoothed version of) W7-X 's vaccum vessel, shown in green, defines the $s_v = s_w$ surface. The magnetic surfaces of the VMEC solution for the same run are shown in black, the last of them corresponding to $s_v = 1$.

being run in free boundary mode with respect to the plasma edge. Several things must be done before SIESTA can be run in this manner, though. First, the background coordinate system that VMEC provides must be extended over the region going from the original plasma boundary ($s_v = 1$) to the new boundary. Secondly, suitable initial guesses for both the magnetic and pressure fields, from which SIESTA will start to iterate, must also be provided over the extended region.

4.2.1 Mesh extension

The extension of SIESTA's background coordinate system beyond the plasma edge of the VMEC solution (i.e., $s_v = 1$) is done as follows. First, it is assumed that the vacuum vessel (or any other external surface chosen for this purpose) corresponds to an isosurface of the extended background coordinate system $s_v = s_w$, for some value $s_w > 1$ yet to be determined. Although it should be kept in mind that $s_v = s_w$ needs not be a magnetic surface. In fact, since magnetic surfaces typically vary during SIESTA's iterative procedure, be it in fixed- or free-plasma-boundary mode, there is no guarantee that $s_v = s_0$ will remain a magnetic surface in the final equilibrium solution for any value of s_0, except for $s_0 = 1$ in fixed-boundary mode. Then, N_ϕ toroidal planes are considered for the angle values,

$$\phi_v^i = \frac{2\pi}{N_p}\left(\frac{i-1}{N_\phi}\right), \quad i = 1, \cdots, N_\phi, \tag{4.4}$$

being N_p the number of periods of the configuration. On each of these toroidal planes, N_θ poloidal angles are selected,

$$\theta_v^k = 2\pi\left(\frac{k-1}{N_\theta}\right), \quad k = 1, \cdots, N_\theta. \tag{4.5}$$

At the i-th toroidal plane, one can easily trace the ray that goes from the axis ($s_v = 0$) to the

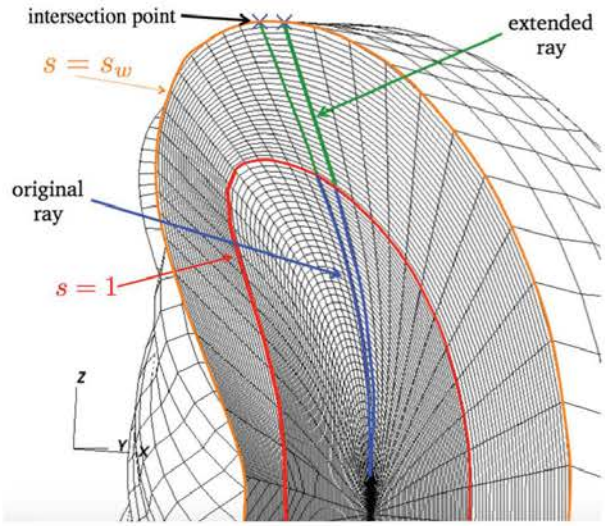

Figure 4.2: Sketch illustrating the construction of the extended coordinate system in the region in between the plasma and the vacuum vessel. First, poloidal rays are extended at each toroidal plane until they intersect the vessel. The collection of all intersections form the $s_v = s_w$ surface, where s_w is to be determined. Intermediate isosurfaces are constructed for $s_v > 1$ by dividing each poloidal ray in a fixed number of equal segments. The value of the label s_v at each of the new surfaces is defined by requiring that the increase in volume roughly grows as the average minor radius.

plasma edge ($s_v = 1$), i.e. $\theta_v = \theta_v^k$ in real space, by summing up the series,

$$R_{k,i}(s_v^l) = \sum_{m=0}^{M} \sum_{n=-N}^{N} R_{mn}(s_v^l) \cos(m\theta_v^k + nN_p\phi_v^i) \tag{4.6}$$

$$Z_{k,i}(s_v^l) = \sum_{m=0}^{M} \sum_{n=-N}^{N} Z_{mn}(s_v^l) \sin(m\theta_v^k + nN_p\phi_v^i) \tag{4.7}$$

for increasing $s_v^l = (l-1)ds, l = 1,2,3\cdots N_s$. Here, $ds = 1/(N_s - 1)$ is the spacing in between isosurfaces that SIESTA uses for fixed-boundary calculations.

To extend the rays beyond $s_v = 1$, we extrapolate both $R_{mn}(s_v^l)$ and $Z_{mn}(s_v^l)$ using a second-order polynomial fit of their values at $s_v^{N_s}$, $s_v^{N_s-1}$ and $s_v^{N_s-2}$ (see Fig. 4.2). Thus, when summing the series for $l > N_s$, the rays cross the plasma edge and move towards the vacuum vessel. In general, each ray will require a different value of $l > N_s$ (say, $l = l_{ik}$ for the i-th ray on the k-th toroidal plane) to cross the vacuum vessel. Therefore, there is no single value of l such that $s_v = s_v^l$ provides a unique label for the vacuum vessel, but it is required that it be an isosurface of the extended background coordinate system. In order to define a more adequate label we proceed as follows. First, the last isosurface of the domain, $s_v = s_w$, is defined as the collection of the intersections with the vacuum vessel of all poloidal rays in all toroidal planes (in cases in which the shape of the last surface contains regions with large degrees of indentation, the intersection points obtained may lie too close

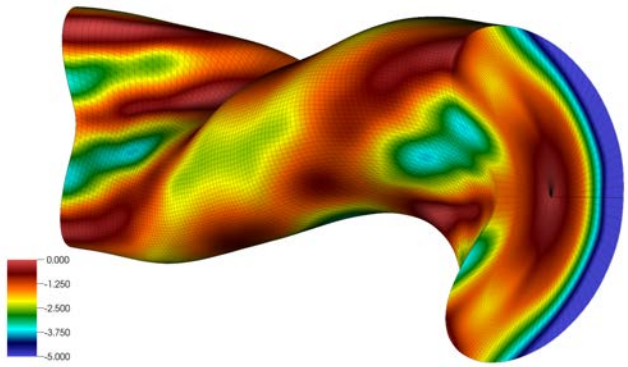

Figure 4.3: Contour plot of the jacobian, $\sqrt{g}$, over the extended computational volume built for the W7-X configuration examined in this paper by using the prescription described in the main text. Isosurfaces of constant s_v, rays of constant θ_v and toroidal planes can be clearly identified from the gridding.

to each other in some parts of the boundary; in those cases, an on-boundary resampling of the intersection positions is done before continuing the procedure). The actual value of s_w still needs to be determined. Next, we divide the part of each ray that goes from $s_v = 1$ to $s_v = s_w$ in N_s' equal segments. Isosurfaces in the extended volume are now successively defined by the collection of the end points of the first segment of all rays, the collection of the end points of the second segment of all rays, and so forth until the vacuum vessel is reached. The value of the label s_v^l for the l-th collection ($l > N_s$) is then assigned by requiring that the increment in volume enclosed by the l-th isosurface,

$$\begin{aligned} V(s_v^l) &= \int_0^{2\pi} d\theta_v \int_0^{2\pi} d\phi_v \sqrt{g}(s_v^l) = \\ &= \int_0^{2\pi} d\theta_v \int_0^{2\pi} d\phi_v R \left(\frac{\partial R}{\partial s_v}\frac{\partial Z}{\partial \theta_v} - \frac{\partial Z}{\partial s_v}\frac{\partial R}{\partial \theta_v} \right) \end{aligned} \tag{4.8}$$

grows as the square of the radial label s_v that defines each magnetic surface. That is,

$$s_v^l = s_v^{l-1} \left(\frac{V(s_v^l)}{V(s_v^{l-1})} \right)^{1/2}, \quad l = N_s + 1, \cdots, N_s + N_s'. \tag{4.9}$$

Once the new radial label is defined in this way, the jacobian $\sqrt{g}$ (see Fig. 4.3), as well as all other metric quantities, can be easily computed in the extended volume from the R_{mn} and Z_{mn} harmonics that define each isosurface for $s_v > 1$. These harmonics are obtained in turn via the Fourier inversion of the $R_{k,i}(s_v^l), Z_{k,i}(s_v^l)$ pairs, for $l > N_s$ (see Eq. 4.7). As the final touch of the extension, the mesh over the vacuum region is resampled along s to ensure that the spacing in the extended volume remains the same as that used for the plasma region, $s_v \leq 1$.

The method just described is the one used for all calculations included in this paper and it shows

to work very well. However, it is possible to do the extension in other ways. For instance, a method based instead on using analytical interpolation formulas is described in Appendix A.

4.2.2 Magnetic field guess in the extended domain

When it comes to the construction of an initial guess for the magnetic field in the extended computational volume, several options are possible. Although theoretically equivalent, it turns out that not all of them are equally optimal after being discretized on SIESTA's numerical mesh. To choose among these options, we have required that two conditions be met in order to facilitate the convergence of SIESTA and make the quality of the final solution better (i.e., a smaller force residual). First, the magnetic field must remain smooth over the extended volume to avoid the introduction of spurious eigenvalues in the Hessian of the problem. Secondly, it must have (almost) zero divergence, since SIESTA does not incorporate any divergence-cleaning strategy at this time.

The first way that comes to mind in order to construct a global guess for the magnetic field is probably to use the VMEC solution (that is, the contravariant B^{θ_v} and B^{ϕ_v} components, since $B^{s_v} = 0$) for all interior isosurfaces (i.e., for $s_v \leq 1$). In addition, one needs to estimate the three contravariant components of the magnetic field in the vacuum region of the extended coordinate system. We have tested several ways to do this. The first method we have tried is to evaluate Biot-Savart's law at each mesh point with $s_v > 1$ using the currents that VMEC provides,

$$\mathbf{B}^{J^{\text{VMEC}}}(\mathbf{r}, s_v \geq 1) = \frac{\mu_0}{4\pi} \iiint_{s_v \leq 1} dV' \, \frac{\mathbf{J}^{\text{VMEC}}(\mathbf{r}') \times (\mathbf{r} - \mathbf{r}')}{|\mathbf{r} - \mathbf{r}'|^3} \quad , \tag{4.10}$$

and add to it the vacuum magnetic field created, at the same location, by the external coils [For instance, in the case of W7-X discussed in this paper, the vacuum field has been computed using IPP's MAG3D code[94].] It is worth pointing out that, although the integration could be carried out directly in SIESTA coordinates, it is more computationally efficient to consider a local cylindrical or cartesian basis for the current vector, and then to project the result of the integral onto the local contravariant basis at $\mathbf{r}$ to get each of the contravariant components of B. Otherwise, Christoffel symbols[60] must be computed to relate the coordinate basis vectors at any arbitrary pair of locations within the volume, which is a very intensive computation.

A second (and faster) approach is to take advantage of the so-called virtual casing principle[46,87], that permits to substitute the volume integral in Eq. 4.10 by the surface integral

$$\mathbf{B}^{J^{\text{VMEC}}}(\mathbf{r}, s_v \geq 1) = \frac{\mu_0}{4\pi} \iint_{s_v = 1} dS' \, \frac{\mathbf{K}_{(\mathbf{r}')} \times (\mathbf{r} - \mathbf{r}')}{|\mathbf{r} - \mathbf{r}'|^3} \quad , \tag{4.11}$$

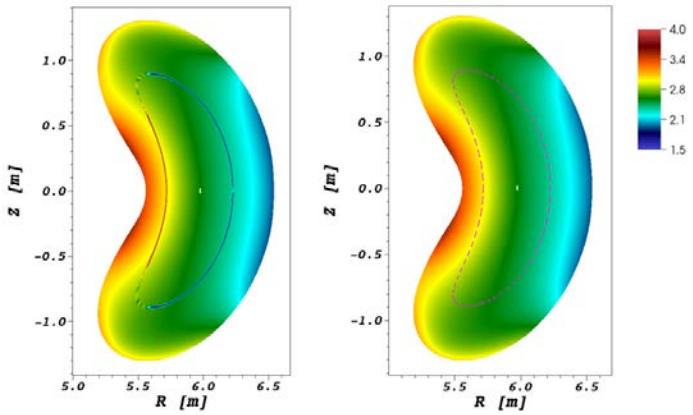

Figure 4.4: Left: Color plot for $|\mathbf{B}|$ for the W7-X magnetic field obtained by combining the VMEC field for $s_v < 1$ with the vacuum field plus the one obtained from Biot-Savart's law (Eq. 4.11) for $s_v > 1$. **Right:** Color plot for $|\mathbf{B}|$ for the field obtained by combining the vacuum field and the one obtained by integrating Biot-Savart's law using VMEC currents over the whole domain (the $s_v = 1$ surface is shown in dashed magenta line). Both are shown at the toroidal plane $\phi_v = 0$.

where the current sheet is given by,

$$\mathbf{K}(\mathbf{r}, s_v = 1) = \frac{[\mathbf{B}_{\text{VMEC}} \times \mathbf{n}]_{s_v=1}}{\mu_0} \quad , \tag{4.12}$$

where $\mathbf{n}$ is the (outwards) normal vector at each location in $s_v = 1$.

We have tested both approaches and found that both of them fail to provide a sufficiently smooth magnetic field across $s_v = 1$, which messes up SIESTA's convergence (see Fig. 4.4; left frame, that shows a color plot of $|\mathbf{B}|$ with a clear discontinuity at $s = 1$). This situation remains, although somewhat improved, even after applying some of the schemes proposed in the literature to remove this discontinuity[30] (namely, to use again the virtual casing principle to remove the vacuum field contribution from the VMEC solution and to replace it by the vacuum field computed directly from the coils).

It is clear that the easiest way to avoid these discontinuities at $s_v = 1$ is to avoid any patching at $s_v = 1$ of fields computed in different ways. For instance, one could discard the VMEC magnetic field for $s_v \leq 1$, integrate instead Eq. 4.11 inside of the plasma region and add to it the vacuum field generated by the external coils. The resulting field does not have any discontinuity at $s_v = 1$ (see Fig. 4.4; right frame). In fact, it often provides a much closer guess to the final solution since it may already contain magnetic islands and stochastic regions within $s_v < 1$. However, this method is still not an optimal choice since, due to the inaccuracies of the numerical integration of Biot-Savart's law, an unacceptably large non-zero divergence is present for the desired resolution (see Fig. 4.5; left frame). This excessively large value of the divergence would regretfully be preserved during the iterative procedure, since SIESTA does not perform any divergence cleaning procedure, which would

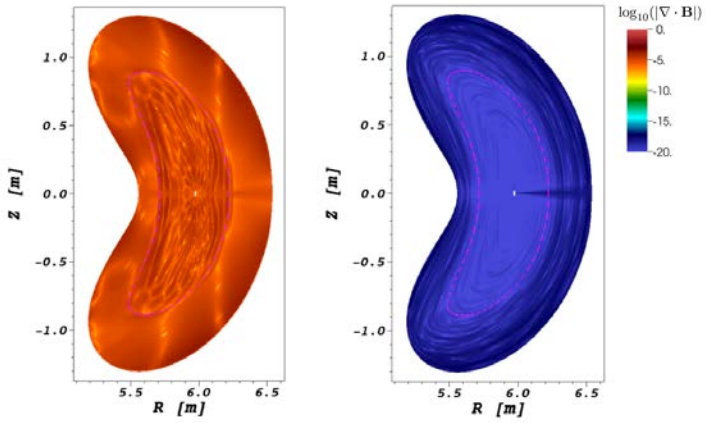

Figure 4.5: Left: Color plot for $\log(|\nabla \cdot \mathbf{B}|)$ for the W7-X magnetic field obtained by combining the vacuum field and the one obtained from Biot-Savart's law (Eq. 4.11) over the whole extended domain. **Right:** Color plot for $\log(|\nabla \cdot \mathbf{B}|)$ for the magnetic field obtained as the curl of the magnetic potential obtained by combining the vacuum one and the one obtained by integrating Eq. 4.17 (the $s_v = 1$ surface is shown in dashed magenta line). Both are shown at the toroidal plane $\phi_v = 0$.

yield a low quality magnetic field after converging.

The divergence problem can be easily resolved by considering instead the magnetic vector potential, $\mathbf{A} = (A_{s_v}, A_{\theta_v}, A_{\phi_v})$, and by differentiating it numerically in such a way that the divergence is identically zero on the SIESTA mesh. Indeed, in general coordinates, the magnetic field is obtained as [here, we use the notation $\tilde{B}^{\alpha} = \sqrt{g}B^{\alpha}$]:

$$\tilde{B}^{s_v} = \frac{\partial A_{\phi_v}}{\partial \theta_v} - \frac{\partial A_{\theta_v}}{\partial \phi_v} \tag{4.13}$$

$$\tilde{B}^{\theta_v} = \frac{\partial A_{s_s}}{\partial \phi_v} - \frac{\partial A_{\phi_v}}{\partial s_v} \tag{4.14}$$

$$\tilde{B}^{\phi_v} = \frac{\partial A_{\theta_v}}{\partial s_v} - \frac{\partial A_{s_v}}{\partial \theta_v}. \tag{4.15}$$

Since SIESTA needs the magnetic field on the radial half mesh, defined as, $s^h_k = ds(k-1/2), k = 1, 2, \cdots N_s + N'_s - 1$, A_{s_v} must be defined on the half radial mesh, but A_{θ_v} and A_{ϕ_v} must both be given on the full radial mesh, $s^f_k = ds(k-1), k = 1, 2, \cdots N_s + N'_s$. It is straightforward to prove that the divergence of the resulting magnetic field now identically vanishes on the half radial mesh.

In order to estimate the vector magnetic potential, we first tested a scheme analogous to the one we outlined earlier for the magnetic field. That is, to integrate numerically

$$\mathbf{A}^{J^{\mathrm{VMEC}}}(\mathbf{r}) = \frac{\mu_0}{4\pi} \iiint_{s \leq 1} dV' \frac{\mathbf{J}^{\mathrm{VMEC}}(\mathbf{r}')}{|\mathbf{r} - \mathbf{r}'|} \quad , \tag{4.16}$$

over the whole extended volume, and to add to the result the magnetic potential vector created by

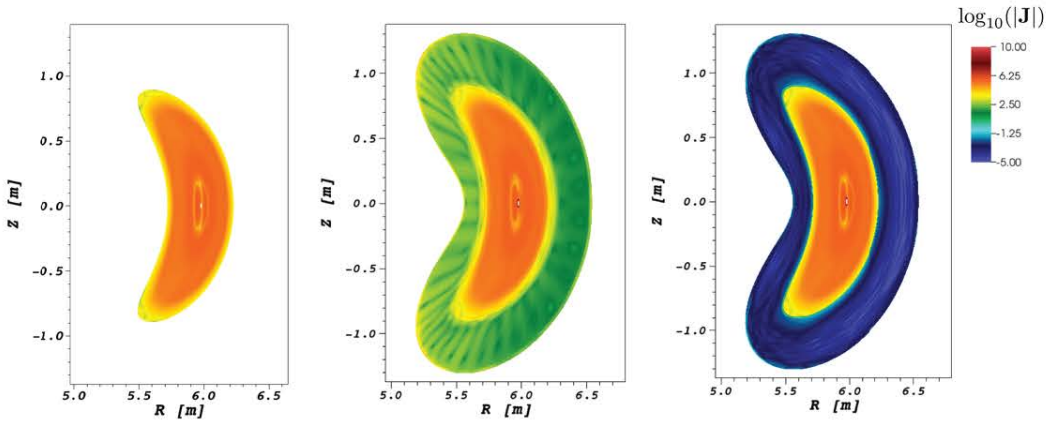

Figure 4.6: Left: Color plot of $\log(|\mathbf{J}|)$ for the original VMEC solution inside $s_v = 1$; **Middle:** color plot for the same quantity as obtained by performing the consistency check described in the text (i.e., evaluating $\mu_0^{-1}\nabla\times\nabla\times\mathbf{A}$) on the W7-X magnetic potential vector obtained by performing the integral that appears in Eq. 4.16. **Right:** Color plot of $\log(|\mathbf{J}|)$ obtained instead by performing the same consistency check on the magnetic potential vector obtained from solving the differential equation Eq. 4.17. Both are shown at the toroidal plane $\phi_v = 0$.

the currents flowing in the external coils [provided again by IPP's MAG3D code]. This approach might appear the perfect solution since no patching of solutions is done, thus avoiding all discontinuities at $s_v = 1$, and a zero divergence of the field is guaranteed over the whole volume. Regretfully, we found that yet another problem appears due to the numerical inaccuracies accumulated during the several coordinate transformations needed to obtain the results on the SIESTA mesh (the integration of Eq. 4.16 is carried out in Cartesian (or cylindrical) coordinates, and then transformed to SIESTA's coordinates to avoid an expensive evaluation of Christoffel symbols; also, the vacuum magnetic potential is provided by MAG3D in cylindrical coordinates). The problem can be made apparent by performing the consistency check of calculating $\nabla\times(\nabla\times\mathbf{A})[=\mu_0\mathbf{J}]$ on the obtained magnetic vector potential. Clearly, the result should be very close to the original VMEC currents (shown in the left frame of Fig. 4.6) only for $s_v < 1$, where the plasma is present, and zero (or very small) everywhere else in the extended computational domain. However, unphysical current densities do appear in the vacuum region, that can locally be significant (see middle frame of Fig. 4.6).

Although these currents could probably be avoided by carrying out all numerical integrations directly on the SIESTA mesh, the computational cost of doing it this way is very large, due to the aforementioned need to evaluate all Christoffel tensors at every point in the mesh. Thus, we have tested another method, that has turned out to be much faster and more efficient. We simply invert numerically Ampére's law inside the extended domain:

$$\nabla\times(\nabla\times\mathbf{A}^{\text{guess}}) = \mu_0\mathbf{J}^{\text{VMEC}}, \quad s \leq s_w, \tag{4.17}$$

differentiated on the SIESTA extended coordinate system, and using the currents VMEC provides as the source. The procedure is much simpler than any of the ones described earlier, since the $\mathbf{A}^{\text{guess}}$ and $\mathbf{J}^{\text{VMEC}}$ vectors are now related locally, meaning that one does not have to deal with coordinate transformations or Christoffel symbols. To have a unique, meaningful solution, Eq. 4.17 is supplemented with two boundary conditions that prescribe the value of the vector potential at the $s_v = \epsilon \ll 1$ and $s_v = s_w$ isosurfaces. These values are computed by integrating Eq. 4.16 and by adding to the result the vacuum potential vector (provided by IPP's MAG3D in this case) at those two surfaces. In this way, the presence of the external coils is felt in the solution through the boundary condition, without having to carry out any additional coordinate transformation. The resulting Poincaré plot for the magnetic field is virtually identical to the one that would be obtained from the integrating procedure but, if the same consistency check is now applied, one finds that all current densities in the vacuum region are virtually zero, as they should be (see Fig. 4.6, right frame).

After all these trials and tests, the procedure we have finally implemented in SIESTA is to obtain the magnetic potential from Eq.4.17, and then build the initial guess for the magnetic field evaluating

$$\mathbf{B}^{\text{guess}} = \nabla \times \mathbf{A}^{\text{guess}}, \quad s_v \leq s_w, \tag{4.18}$$

at every point in the SIESTA mesh by using the internal SIESTA's discretization scheme (Eq.4.13).

4.2.3 Plasma pressure guess in the extended domain

Regarding the guess for the pressure field, $p^{\text{guess}}(\mathbf{r})$, a natural choice would be to use the pressure profile provided by VMEC for $s_v < 1$, and to set it to zero elsewhere. This choice leads however to numerical problems for SIESTA's iterative scheme for at least the following reason. The local deviations in pressure and magnetic field that, according to ideal MHD[36], a plasma displacement $\boldsymbol{\xi}$ causes from its current state $(p_0,\ \mathbf{B}_0)$ are:

$$\delta p = -(\xi \cdot \nabla) p_0 - \Gamma p_0 \nabla \cdot \xi \tag{4.19}$$

$$\delta \mathbf{B} = \nabla \times (\xi \times \mathbf{B}_0) \tag{4.20}$$

If p_0 vanishes for $s_v > 1$, it is clear that one could build many different non-zero displacement fields ξ that vanish for $s_v \leq 1$, but that are non-zero and parallel to $\mathbf{B}_0$ for $s_v > 1$. None of these displacements change the total MHD energy, since $\delta p = \delta \mathbf{B} = 0$ everywhere. Thus, if such displacements are allowed, the kernel of the numerical Hessian of the problem becomes huge which causes severe convergence problems. In order to avoid the formation of such a kernel, we have considered instead a finite, fast-decaying pressure profile for $s_v > 1$.

4.2.4 Boundary conditions at $s_v = s_w$

The last piece needed to complete the free-plasma-boundary extension of SIESTA is to choose the boundary conditions that will be applied at the new fixed boundary, $s_v = s_w$. In the original SIESTA implementation, $s_v = 1$ was assumed to stay a true magnetic surface. Thus, it was natural to prescribe $p(1) = B^s(1) = 0$. In the extended version, this ceases to be the case since $s = s_w$ needs not be a magnetic surface [Indeed, the vacuum magnetic field calculated from the coils is usually not tangent to the vacuum vessel.]. Instead, we do impose $p(s_w) = 0$ and keep $\mathbf{B}(s_w)$ at the same value that the initial guess for the magnetic field had at $s = s_w$. The physical justification for this choice comes from the fact that most vacuum vessels are made of steel (with a conductivity $\sigma \sim 10^6(\Omega \cdot m)^{-1}$) and have widths $\Delta \sim (1-2)$cm, which yields a penetration time for the magnetic field through the vessel of $\tau_m \sim \mu\sigma\Delta^2 \sim (200-300)$ ¯s. Therefore, the vacuum field has plenty of time to penetrate the vessel before the plasma discharge even starts, at least for stellarators. The non-linear response of the plasma is not included in our chosen boundary condition for $\mathbf{B}$, but we think that the error made will be relatively small considering that s_w is far from the plasma edge. We will provide numerical evidence supporting this claim for the W7-X case used to illustrate SIESTA's new capabilities in the next section. It is left to a future extension of this work to iterate on this boundary condition by including the changes of the plasma response during the SIESTA iteration.

4.3 Free-plasma-boundary SIESTA calculations for the W7-X stellarator

The Wendelstein 7-X (W7-X) stellarator[7] is an experimental device located in Greifswald, Germany by the Max-Planck-Institute for Plasma Physics. It is one of the largest stellarators in operation with a major radius $R_0 = 5.5$m, a minor radius $a = 0.53$m, and a magnetic field up to $B_0 = 3$T made possible by superconducting coils. The five period ($N_p = 5$) W7-X has been designed to have low magnetic shear, optimized for small bootstrap current and equipped with an island divertor for particle and power control.

The W7-X configuration that we have chosen to illustrate the new free-plasma-boundary capabilities of SIESTA has the rotational transform profile shown in the left frame of Fig. 4.7. Several rational surfaces exist at locations with $s_v < 1$ as shown in the figure, but they are of relatively high order. Its more salient feature, however, is that the low-order $5/5$ rational is located just outside the plasma edge in order to provide the basis for an island divertor magnetic field topology to isolate the plasma from the vacuum vessel.

The vacuum field for this configuration, as provided by IPP's MAG3D code is shown in Fig. 4.8. It clearly shows the $5/5$ magnetic island just outside the plasma edge considered by VMEC at $s_v = 1$, whose boundary is shown in magenta. Its presence makes this configuration a particularly useful

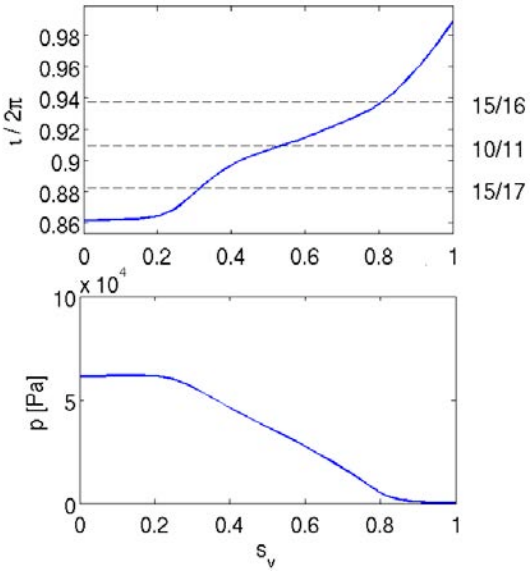

Figure 4.7: Rotational transform (above) and plasma pressure (below) radial profiles for the W7-X configuration examined in this paper. The locations of the lowest order rational surfaces are indicated, in the rotational transform profile, with horizontal dashed lines.

test case to illustrate the new free-plasma-boundary capabilities of SIESTA, since we expect the island to modify the plasma edge significantly, once the equilibrium solution is extended all the way to the vacuum vessel.

The VMEC equilibrium solution (converged down to a normalized force residual $\langle |\mathbf{F}|^2 \rangle \sim 10^{-20}$, where the brackets stand for volume average) naturally has perfectly nested magnetic surfaces all the way to $s_v = 1$, as advertised (see Fig. 4.9). We have used $N_s = 49$ radial points, $M = 20$ and $N = 16$, that amounts to roughly 700 different harmonics. Cross-sections of the magnetic surfaces obtained by VMEC, for an average $\beta \equiv \langle 2\mu_0 p / B^2 \rangle \sim 0.8\%$, are shown in Fig. 4.9.

4.3.1 Fixed-boundary calculation

First, we proceed to run SIESTA in its standard fixed-boundary mode. The $\beta \sim 0.8\%$ VMEC equilibrium previously described provides both the fixed background coordinate system and the seed magnetic field to start the iteration. The number of isosurfaces considered in the SIESTA run is the same as in the VMEC solution, $N_s = 49$, although the fields have been resampled on SIESTA's radial coordinate, since $s_v = \sqrt{s}$. The harmonic content of the solution is also the same as that of VMEC, $M = 20$ and $N = 16$.

After a few iterations in which a finite, albeit small resistivity is applied, the resistive step is removed and the solution is allowed to converge to a final equilibrium in which the average force residual is of the order of $\langle |\mathbf{F}|^2 \rangle \sim 10^{-20}$. No perturbation of the seed field has been applied, but

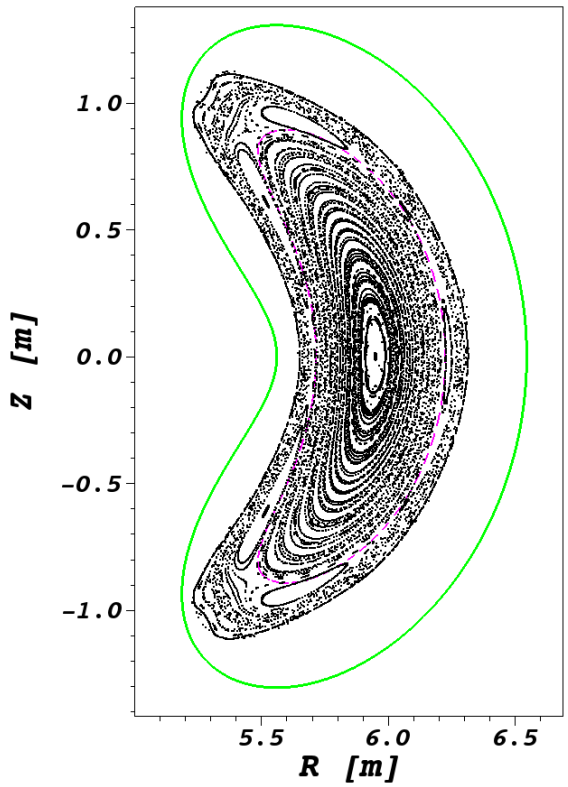

Figure 4.8: Poincaré plot at the toroidal plane $\phi_v = 0$ of the vacuum magnetic field for the W7-X configuration used, as provided by IPP's MAG3D code.

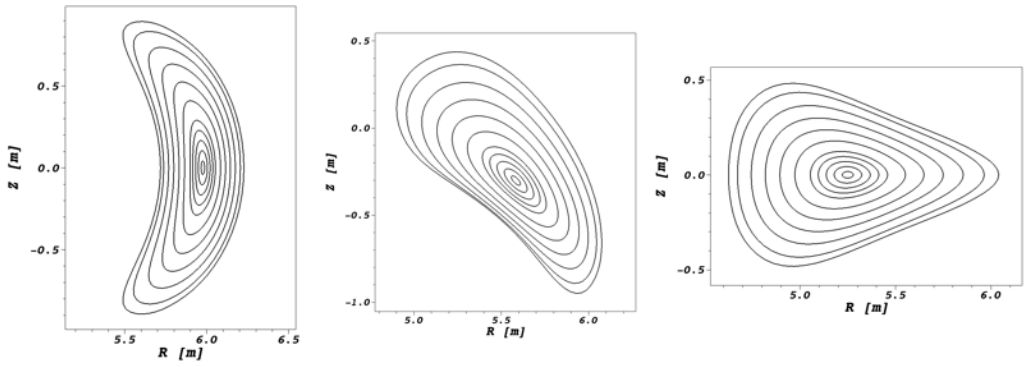

Figure 4.9: Several toroidal cross-sections (at toroidal angles $\phi_v = 0, \pi/(2N_p), \pi/N_p$) of the magnetic surfaces obtained by the VMEC code for the W7-X configuration under study.

a small, finite resistivity is allowed in the first few iterations to permit the adjustment of the pressure if needed. The final equilibrium magnetic field is shown in Fig. 4.10, where a Poincaré plot for the

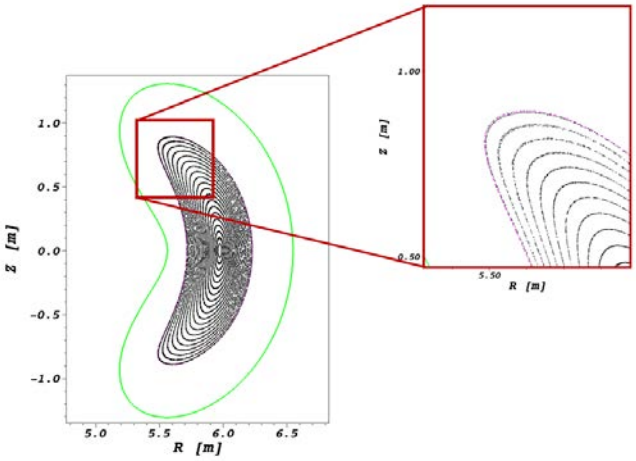

Figure 4.10: Poincaré plot at the toroidal plane $\phi_v = 0$ of the magnetic field of the converged equilibrium obtained by SIESTA when run in fixed boundary mode.

final magnetic field is shown at the toroidal cross-section $\phi_v = 0$. As expected, no visible magnetic island appears for $s_v \leq 1$ since no low-order rational surfaces are present there. In fact, it is very similar to the VMEC solution (Fig. 4.9). The corresponding reduction in the total MHD energy is small with respect to the VMEC solution being roughly $\delta W / W \sim 10^{-7}$.

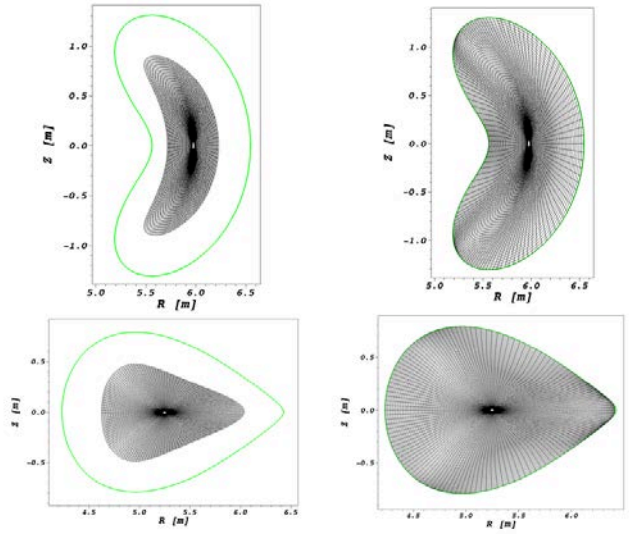

Figure 4.11: Left: cross-sections of magnetic surfaces at toroidal angles $\phi_v = 0,\ \pi / N_p$ for $s_v \leq 1$, including the vacuum vessel (in green) for W7-X; **Right:** same cross-sections for the final extended mesh up to $s_v = s_w$.

4.3.2 Free-plasma-boundary calculation

We illustrate next the capabilities of the new extension of SIESTA. As previously advertised, the vacuum vessel of W7-X (or, more precisely, a smoothed-out version of it) is used as the new external boundary. It is shown in green in Fig. 4.11 (a 3D portion of it is also shown in Fig. 4.1). The extended mesh that results from following the procedure described in Sec. 4.2.1 is also shown in Fig. 4.11. It has a total of 82 isosurfaces (i.e., $N_s = 49; N_s' = 33$). The first 49 isosurfaces (that is, those with $s_v \leq 1$) are in essence those of the VMEC solution, albeit resampled to be evenly spaced with respect to the new radial label $s_v = \sqrt{s}$. The next 33 isosurfaces correspond to values of the radial coordinate $s_v > 1$. The last isosurface, $s_v = s_w$, naturally coincides with the smoothed-out vacuum vessel. Regarding the number of harmonics, $M = 20$ and $N = 16$ has been chosen in order to properly capture the complex harmonic content of the external region, introduced in part by the shape of the vacuum vessel. In fact, that is why we chose those values for the previous VMEC runs, in spite of the fact that a good VMEC solution is possible with less harmonics. All the required metric information (the jacobian, for instance, is shown in Fig. 4.2) has been computed, over the extended mesh, using the procedure described in detail in Sec. 4.2.1.

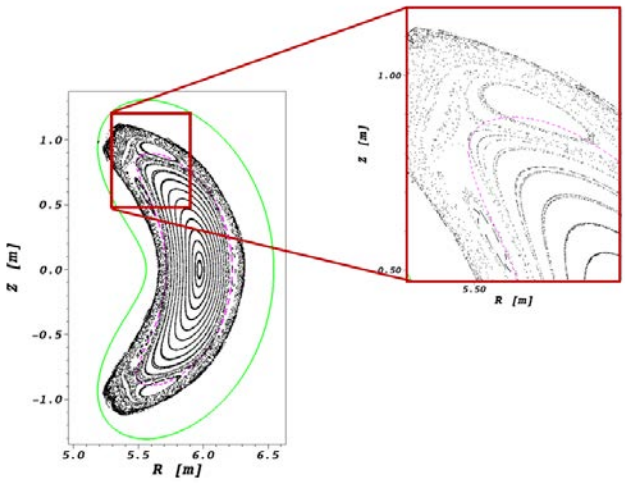

Figure 4.12: Poincaré at the toroidal plane $\phi_v = 0$ of the magnetic field of the converged equilibrium obtained by SIESTA when run in free-plasma-boundary mode.

The converged results of the SIESTA free plasma boundary run, which took close to 4 hours running in 16 XEON processors of the E5 family, (with a normalized residual force $\langle F^2 \rangle \sim 10^{-18}$) are shown in Figs. 4.12 and 4.13. The corresponding reduction in the total MHD energy is now significant, $\delta W / W \sim 10^{-5}$, since it is two orders of magnitude greater than the change of energy achieved in the previous fixed-boundary run, where no islands appeared in the equilibrium. Fig. 4.12 shows the Poincaré plot of the converged magnetic field for the configuration under study. As it is

clearly shown, the magnetic island associated to the $5/5$ rational surface is now wide enough as to penetrate the $s_v = 1$ surface (shown in magenta), thus deforming the plasma boundary (see also Fig. 4.14). This is a direct consequence of the finite pressure of the equilibrium, as it becomes apparent after comparing this Poincaré plot with that shown in Fig. 4.8 for the vacuum case. The phase of the island in the finite pressure case remains the same as that of the vacuum, in contrast to what is sometimes found for higher-β cases, where the phase of the island may also shift. Due to the small β, the position of the magnetic axis also remains unchanged with respect to the vacuum case, due to the negligible Shafranov shift.

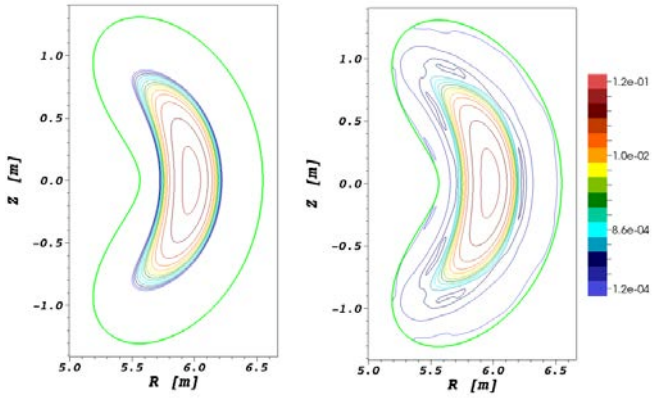

Figure 4.13: Left: pressure isosurfaces shown at the toroidal section $\phi_v = 0$ for the equilibrium solution obtained by SIESTA in fixed-boundary for the W7-X equilibrium with 0.8% discussed in the text; **Right:** pressure isosurfaces for the converged equilibrium solution found by SIESTA when run in free-plasma-boundary mode instead. In all plots, the $s_v = 1$ surface is shown in magenta; the $s_v = s_w$ surface is shown in green.

Fig. 4.13, on the other hand, shows a set of selected isosurfaces for the plasma pressure for two of the W7-X runs previously described. On the left, contours are shown for the SIESTA fixed-boundary converged solution which, in essence, is identical to the original VMEC solution for this case. On the right, the pressure contours shown correspond to the final equilibrium solution found by SIESTA when run in free-plasma-boundary mode. As can be seen, the few resistive iterations that took place at the beginning of SIESTA's nonlinear iteration have allowed the pressure contours to align themselves with the modified magnetic structure, in order to satisfy $\mathbf{B} \cdot \nabla p = 0$. In the process, the shape of the plasma boundary has been modified to adapt to the new topology existent across the region where the $5/5$ islands are present, as shown in more detail in Fig. 4.14. It is also worth noting that the pressure isosurfaces that appear for $s_v > 1$ correspond to the (very tenuous) pressure that was included in the vacuum region (see discussion in Sec. 4.2.3) in order to avoid a Hessian with a large, non-trival in the linear problem that SIESTA solves at each step of the nonlinear Newton iteration. They are absent in the fixed-boundary solution.

Finally, we are now in the position to check the validity of the assumption made in Sec. 4.2.4 re-

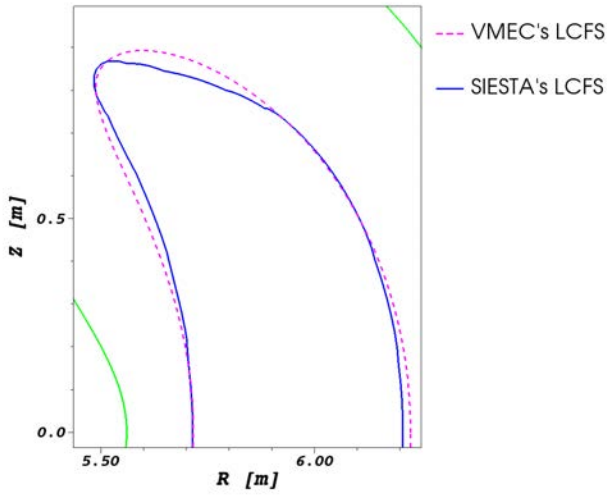

Figure 4.14: Plasma boundaries at the upper part of the $\phi_v = 0$ cross-section for the original VMEC and SIESTA fixed-boundary runs (shown in dashed magenta) and the final plasma boundary obtained by SIESTA when run in free-plasma-boundary mode (in blue).

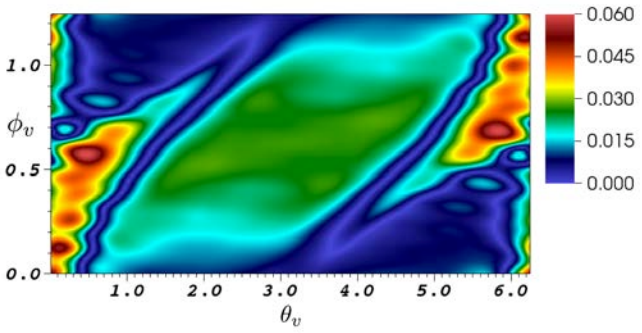

Figure 4.15: Isolevels of $|\mathbf{A}_1 - \mathbf{A}_2| \,/\, |\mathbf{A}_1|$ on one period of the boundary surface at $s_v = s_w$. Here, $\mathbf{A}_1$ is the value of the magnetic potential vector used as boundary condition (see discussion in Sec. 4.2.4) while $\mathbf{A}_2$ is the magnetic potential vector obtained by integrating all the currents (plasma and coils) of the final SIESTA solution.

garding the modification of the value of the magnetic potential vector at $s = s_w$ by the nonlinear plasma response being small. Fig. 4.15 shows the isolevels of the relative difference at $s_v = s_w$ between the magnitude of two magnetic vector potentials: the one used as boundary condition, and the one resulting from integrating plasma and coil currents from the converged SIESTA solution. As can be seen, the modification is small as expected, having an average value of just 2%. Furthermore, if we examine only the most important resonant harmonic in this configuration, i.e. $(m = 5,\ n = 5)$, the error drops to 0.02% at the vacuum vessel.

4.4 Conclusions

A free-plasma-boundary extension of the SIESTA MHD equilibrium code has been presented. By enlarging SIESTA's computational volume, the plasma edge ceases to be considered a fixed boundary, being now able to freely change in order to balance any pressure or magnetic forces that might be present. As a result, SIESTA is now in the position to address problems in which a perturbed plasma edge might become important, such as the application of edge magnetic resonant perturbations[31], or the possible distortion of the plasma edge due to unbalanced plasma currents such as bootstrap or heating-induced currents[41].

It is important to keep in mind that, in all SIESTA free-plasma-boundary runs, the vacuum magnetic field (or, more precisely, the magnetic vector potential) created by the external coils must be explicitly provided. At least, on the two surfaces used to provide the boundary conditions to solve Eq. 4.17. For the W7-X configuration studied in this paper, the vacuum vector potential has been calculated by means of IPP's MAG3D code. But for applications to other devices, this information will have to be provided by the user. Work is currently underway to make SIESTA capable of extracting this information from the same files (the so-called (*mgrid*) files) that VMEC uses when run in free-boundary mode[52].

Appendix A. Alternative mesh extension scheme via interpolation formulas.

The mesh extension procedure that was described in Sec. 4.2.1 relied on the building of a proper database of points over the extended domain, from which the s_v-isosurfaces of the SIESTA coordinate systems was built. The starting point was a set of intersections of the extrapolated poloidal rays of the VMEC coordinate system with the last closed surface (usually the vacuum vessel), calculated at each toroidal plane. The undesired accumulation of these intersection points that often appears near regions with large indentation was dealt with by point resampling over the last closed surface, if needed. This method works very well and has been used in all the calculations included in the paper, but it is not the only one possible.

In this appendix, we discuss a second possibility based on the use of interpolation formulas. The starting point is to express the vacuum vessel position in a Fourier series analogous to the one VMEC uses, although with θ the geometrical angle, not VMEC's internal angle.

$$R^{\mathrm{VV}}(\theta,\phi) = \sum_{m,n} R^{\mathrm{VV}}_{mn} \cos(m\theta - nN_p\phi); \tag{4.21}$$

$$Z^{\mathrm{VV}}(\theta,\phi) = \sum_{m,n} R^{\mathrm{VV}}_{mn} \sin(m\theta - nN_p\phi) \quad , \tag{4.22}$$

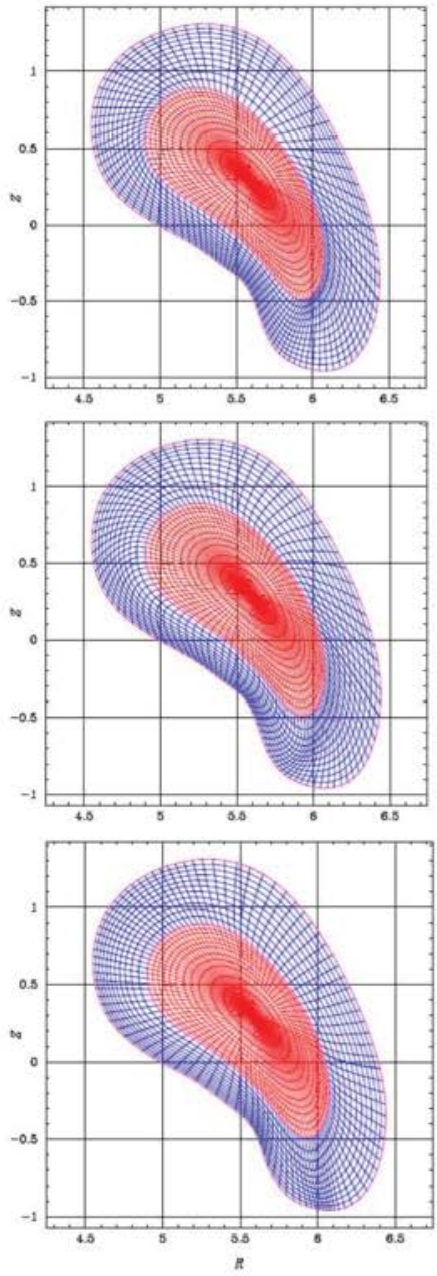

Figure 4.16: Cross sections at toroidal angle $\phi = \pi/(2N_p)$ of the magnetic surfaces obtained over the extended volume (in red, the original VMEC surfaces for $s_v \leq 1$; in blue, over the extended region) for the W7-X configuration examined in Sec. 4.3.2 using linear, quadratic and quadratic with slip interpolation formulas discussed in Appendix A.

We will also introduce the notation,

$$R^1(\theta,\phi) = \sum_{m,n} R_{mn}(s_v = 1)\cos(m\theta - nN_p\phi) \tag{4.23}$$

$$Z^1(\theta,\phi) = \sum_{m,n} Z_{mn}(s_v = 1)\sin(m\theta - nN_p\phi) \quad , \tag{4.24}$$

for the positions of the points located at the last VMEC closed surface, $s_v = 1$, at the same angle value (i.e., for $\theta^* = \theta$).

We now seek an interpolation formula that will generate the extension of the mesh between VMEC's last closed surface and the vacuum vessel while, at the same time, providing continuity of all quantities and their derivatives across the $s_v = 1$ surface. It turns out that linear interpolation is not good enough. Indeed, if one tries, for fixed θ and ϕ (we drop their dependence in what follows, although it is implicitly assumed), a linear formula such as:

$$R(\rho) = R^1 + \rho(R^{VV} - R^1) \tag{4.25}$$

$$Z(\rho) = Z^1 + \rho(Z^{VV} - Z^1) \quad , \tag{4.26}$$

one obtains an interpolation that has no continuous derivative at $s = 1$. This is clearly appreciated in the upper frame of Fig. 4.16, that shows the cross-section of the extended coordinate system for the W7-X configuration at toroidal angle $\phi = \pi/(2N_p)$. The reason is that θ and θ^* are very different angles, although we have used them as if they were the same.

This limitation can be avoided by moving to a quadratic representation such as:

$$\begin{aligned} R(\rho) &= \frac{R_s^1}{2}\left[1 - \rho^2 - (1-\rho)^2)\right] + R^1 + \\ &\quad +\rho^2(R^{VV} - R^1) \end{aligned} \tag{4.27}$$

$$\begin{aligned} Z(\rho) &= \frac{Z_s^1}{2}\left[1 - \rho^2 - (1-\rho)^2)\right] + Z^1 + \\ &\quad +\rho^2(Z^{VV} - Z1) \quad . \end{aligned} \tag{4.28}$$

Here R_s^1 and Z_s^1 are the radial derivatives at the $s_v = 1$ surface. The result of using the second-order interpolation is shown in the middle frame of Fig. 4.16. Clearly, all derivatives are now continuous across the $s_v = 1$ surface. However, some additional curvature (to the poloidal rays) has been introduced in the process that would introduce undesired additional angular dependences in the metric tensor, compared to how they behave inside $s_v = 1$. These undesired effects can be ameliorated by introducing a poloidal slip function $\lambda(\theta)$ that allows each of the initial vessel points to slide poloidally along the vessel while preserving the vessel shape (in a spirit that is very similar to how points on the vessel were poloidally redistributed in the procedure described in Sec. 4.2.1 to avoid accumulation near regions with large indentation):

$$R(\lambda, \theta) = R_{VV}(\theta + \lambda) \tag{4.29}$$

$$Z(\lambda, \theta) = Z_{VV}(\theta + \lambda) \quad . \tag{4.30}$$

The only requirement on λ is that $1 + d\lambda/d\theta > 0$, so that the new angle distribution stays monotonic. We determine $\lambda(\theta)$ by minimising (as a function of θ, at each toroidal plane) the curvature of each poloidal ray, roughly given by:

$$\kappa^{-1} \sim \sqrt{R_{\rho\rho}^2 + Z_{\rho\rho}^2} \quad . \tag{4.31}$$

The significant improvement of applying the sliding is illustrated in the lower frame of Fig. 4.16, where the largely reduced curvature of the poloidal rays for $s_v > 1$ is apparent.

Acknowledgements

Research funded in part by the Ministerio de Economía, Industria y Competitividad of Spain, grant No. ENE2015-68265. Research carried in part at the Max-Planck-Institute for Plasma Physics in Greifswald (Germany), whose hospitality is gratefully acknowledged. Research supported in part by the US Department of Energy, Office of Fusion Energy Sciences under Award DE-AC05-00OR22725. SIESTA runs have been carred out in *Uranus*, a supercomputer cluster located at Universidad Carlos III de Madrid and funded jointly by European Regional Development Funds (EU-FEDER) project No. UNC313- 4E-2361, and by the Ministerio de Economía, Industria y Competitividad via the National Projects No. ENE2009-12213-C03-03, No. ENE2012-33219, and No. ENE2012-31753.

The contents of this chapter were submitted in September 2017*, for publication the Plasma Physics and Controlled Fusion Journal by H. Peraza-Rodriguez, J. M. Reynolds-Barredo, R. Sanchez, J. Geiger and V. Tribaldos under the name "Bootstrap current control studies in the Wendelstein 7-X stellarator using the free-plasma-boundary version of the SIESTA MHD equilibrium code"*[80].

5

First free-boundary SIESTA calculations

Abstract

The recently developed free-plasma-boundary version of the SIESTA MHD equilibrium code[54,81], is applied to the study of bootstrap current control scenarios for a selected configuration of the Wendelstein 7-X (W7-X) stellarator. Freely evolving bootstrap currents could lead to a deterioration of some design features of W7-X, either by creating unwanted magnetic island chains and/or stochastic regions within the plasma, or by altering the shape and/or location of the plasma edge. The latter issue is particularly relevant for W7-X since it often relies on a (vacuum) magnetic island chain located just outside of the plasma edge to isolate the confined plasma from the first wall and to control the particle and energy exhaust towards the divertor plates. In this paper we show that the free-plasma-boundary version of SIESTA is a useful tool to treat the resulting non-linear MHD equilibrium problem self-consistently, both inside and outside of the plasma, and to provide support for this type of studies.

5.1 Introduction

The W7-X stellarator, that started its operation in December of 2015 at the Max-Planck Institute for Plasma Physics in Greifswald[91], has been optimised so that it presents a magnetic topology with good MHD stability, improved neoclassical confinement and low bootstrap currents. Nevertheless, scenarios exist at finite pressure in which the development of self-generated neoclassical bootstrap currents[10,37] may alter the confinement properties of the device, due to the modifications on the ro-

tational transform profile it may cause[48]. A modified rotational transform profile could result in the formation of magnetic islands or stochastic regions inside of the plasma, leading to a reduction of the confinement volume, and therefore to a decrease of the confined energy. In addition, these modifications might also displace and distort the topology of the vacuum magnetic island chain that sits just outside of the plasma, isolating it from the walls and controlling the particle and energy exhaust towards the island divertor plates. Clearly, any possible changes in size, position and phase of this island chain need to be predicted and counteracted when needed. For instance, in some scenarios the island could move within the plasma from the edge, reducing the confined plasma volume significantly. Or, in other cases, the island chain could move beyond the divertor plates leading to the contact of good flux surfaces with the divertor, that would start to function instead as a normal limiter.

Due to their importance for the operation of W7-X , a number of possible control procedures for bootstrap scenarios have been investigated in a number of previous works[40,41,57,99]. Two main scenarios are usually considered: a first one at low to mid plasma densities, where self-generated bootstrap currents can become significant but, at the same time, Electron Cyclotron Current Drive (ECCD) using the X2-mode can be used efficiently; and a second one at higher plasma densities, where bootstrap currents are smaller (due, among other things, to the larger collisionalities) but in which X2-mode ECCD is no longer available due to the plasma density being above the X2-mode cutoff, and other schemes are necessary. In this work we will focus only on the first type of scenarios. That is, those with low to mid plasma density and significant bootstrap current generation. In them, ECCD is considered adequate to compensate any unwanted currents since current diffusion takes place on a timescale of the order of the resistive skin time that, for the W7-X conditions, is of the order of a few seconds. The analysis of these cases is usually done by iterating between several ideal MHD equilibrium and transport codes. The procedure goes approximately as follows. First, an MHD equilibrium solution is obtained within the plasma with the VMEC code[52] for the W7-X configuration of interest. VMEC is a very fast ideal MHD equilibrium solver, widely used throughout the stellarator community, that assumes however that closed magnetic surfaces exist over the whole plasma volume. The magnetic field found by VMEC is then used, together with the plasma profiles considered, to estimate the neoclassical bootstrap current by means of the NTSS transport code[98], that uses for its neoclassical calculations the coefficients provided by the DKES code[100] for that particular VMEC equilibrium. The estimated bootstrap current is added to the plasma currents previously found by VMEC, and then given back to VMEC to obtain a new MHD equilibrium. This cycle should be repeated, in principle, for as long as required for convergence (i.e., until the difference in estimated bootstrap currents becomes smaller than a certain tolerance), although acceptable results are usually obtained after a just a few iterations. In order to investigate the impact of the bootstrap current on the topology and location of the magnetic island chain that

separates the plasma from the divertor, an estimate for the magnetic field in the region between the plasma and the vacuum vessel (we will loosely refer to it as the "vacuum region" in what follows) is also needed. VMEC does not provide that kind of information, though. In the works previously mentioned, the magnetic field in this region was obtained instead by combining a Biot-Savart integrator (in this case, IPP's MAG3D code[94]), that takes into the account the currents flowing in the external coils, together with the results of the EXTENDER code[30]. EXTENDER uses the so-called "virtual-casing principle"[46,87] to estimate the magnetic field created by VMEC's plasma currents from the last flux surface considered by VMEC to the vacuum vessel. Since no assumptions are being made here, any possible magnetic topology could in principle be obtained across this extended region, even including magnetic islands and stochastic regions. The procedure just outlined, that considered a single instant of time, is easily extended to cases in which the plasma profiles are evolved in time (in the case of W7-X , this usually is done by means of the NTSS transport code[98], that includes all relevant fuelling and heating sources and sinks). One just needs to repeat the previously described sequence for every time of interest during the simulated scenario.

The methodology just described, although very useful, is however not optimal. Clearly, VMEC's assumption regarding the existence of closed magnetic surfaces within the plasma region is a very strong one that may not hold in some cases (although we will discuss later that the VMEC+EXTENDER combo performs better that what might be expected a priori, due to some additional treatment of the combined solution to be described soon[41]). In particular, whenever the rotational transform profile includes low-rational surfaces inside the plasma. This might be the case, for instance, if the modifications induced by the self-generated bootstrap current bring the vacuum island chain that separates the confined plasma from the island divertor inside of the plasma. Other low-order rationals may also enter the plasma, either from the magnetic axis or from the edge, further deteriorating the topology of the confining magnetic field. In each of these cases, the VMEC solution misrepresents the plasma currents at the rational surfaces, where current sheets form to prevent the opening up of magnetic islands[68,85]. As a result, these current sheets contribute to the estimate of the magnetic fields that EXTENDER calculates over the "vacuum region" that goes from the plasma edge to the vacuum vessel. It is thus apparent that any ideal MHD solver not assuming the existence of nested magnetic surfaces[54,58,84,93] would be better suited for this type of studies. Historically, these solvers have not been used because they are often complicated to use and computationally very intensive, which usually makes them inadequate for use in any optimization environment that might require tens or hundreds of runs, and particularly in free-boundary mode. In this paper we will show that the recently released free-plasma-boundary version of the SIESTA code[54,81] can deal with this type of problems rather effectively, being able to compute the MHD equilibrium solution over the combined plasma+vacuum region simultaneously without making any assumption on the underlying magnetic topology, usually in just a few hours. It is worth noting, though, that a code like

SIESTA cannot fully replace VMEC in the bootstrap current studies previously described. The reason is that, at this time, there is no code that could estimate neoclassical bootstrap currents without assuming underlying closed magnetic surfaces within the plasma region. In spite of this, SIESTA can provide a very useful tool to ensure that the predictions of codes such as VMEC+EXTENDER are physically meaningful, both inside and outside of the plasma. We will illustrate this fact by applying the free-plasma-boundary SIESTA to a previously investigated bootstrap-current control scenario for the W7-X standard configuration [41]. The study will imply the analysis of two situations, a first one with freely-evolving bootstrap currents and a second one in which ECCD is applied to try to compensate them. The paper is thus organized as follows. In Sec. 5.2 we will first describe the analysis of the two W7-X scenarios using the VMEC+EXTENDER combo. Then, Sec. 5.3.1 presents the results of applying SIESTA to the freely-evolving bootstrap scenario, while the application of SIESTA to the ECCD scenario is presented in Sec. 5.3.2. Finally, we will summarise our results and draw some conclusions in Sec. 5.4.

5.2 Considered W7-X scenarios

In the last few years several bootstrap current scenarios have been studied for W7-X in order to design methods to heal their possible undesired consequences [40,41,72,99]. The analysis was made by combining the temporal evolution of the plasma profiles and the estimation of the bootstrap current carried out by the NTSS transport code [98], with the calculation of the magnetic field at each time carried out by the VMEC+EXTENDER combo, as we described previously. The NTSS code uses the mono-energetic neoclassical transport coefficients estimated with the DKES code [100] to calculate the neoclassical transport coefficients that are appropriate for each plasma profile. In the case in which ECCD is included, the TRAVIS code [71] is used to estimate the ECRH power deposition profiles and the current drive achieved at each iteration. The resulting modification of the rotational transform due to ECCD is then included in the VMEC+EXTENDER calculation. In the absence of an Ohmic transformer, the evolution of the toroidal current density involves shielding currents and their redistribution on a time of the order of the resistive skin time, that is of the order on one second. The total toroidal current, on the other hand, evolves on the time scale of the L/R time that for present parameters, is of the order of twenty to forty seconds.

A detailed description of the results of the aforementioned studies can be found in Ref. [40]. We will partially repeat them here by focusing on one particular case, pertaining to W7-X standard configuration, that is described next. The estimated toroidal current (including self-generated bootstrap currents) and the resulting rotational transform profiles for these cases are shown in Figs. 5.1 and 5.3, with the freely-evolving case shown in the first figure and the ECCD compensated case in the second. For reference, it is also worth saying that the W7-X standard configuration has been designed to have a negligible toroidal current. Its rotational transform lies in between the $5/6$ and the $5/5$

rationals, the latter being responsible for the island chain that appears just outside of the plasma edge (i.e., at $s = 1$ in SIESTA coordinates, where $s = \sqrt{\psi/\psi_{edge}}$ is used as the radial coordinate, with ψ corresponding to the magnetic toroidal flux), that forms the divertor. Only the $10/11$ rational surface lies within the plasma, approximately at $s = 0.6$.

5.2.1 Freely-evolving bootstrap current case

As can be seen in the left frame of Fig. 5.1, the initially negligible toroidal current density is significantly increased due to the self-generation of the bootstrap contribution as $< \beta >$ increases up to approximately 2%. At the time $t = 6$ sec, the shielding currents are distributed according to the conductivity profile and, since their decay is just starting, the net current is still small. Nevertheless, the central rotational transform is greatly reduced for $s < 0.7$ (see right frame of Fig. 5.1, in red), with three new low-order rational surfaces, the $5/6$, $10/13$ and $5/7$ rationals, having made their way into the plasma from the axis. At $t = 110$ sec (shown in green), on the other hand, the shielding currents have had time to decay almost entirely. Therefore, the near-axis toroidal current has managed to reverse the sign of the toroidal current density, pushing the aforementioned three low-order rationals back out of the plasma, but at the cost of introducing the edge $5/5$ rational (that is, the one that forms the island divertor) to the middle of the plasma, at approximately $s = 0.6$, and displacing the $10/11$ rational to about $s \sim 0.4$.

We will take a look at the resulting magnetic field structure by constructing Poincaré puncture plots for the field obtained by the VMEC+EXTENDER combo described earlier (see Fig. 5.2). Several things are worth commenting here. Starting with the puncture plot at $t = 6$ sec shown on the left, it is clear that the location of the $5/5$ rational remains at the edge, as expected since the edge rotational transform is not modified there (see right frame of Fig. 5.1, in red). However, the island chain *penetrates the plasma edge* (i.e., $s = 1$) up to about $s \sim 0.9$. The fact that the VMEC+EXTENDER solution contains an island within $s < 1$ is rather surprising, since the VMEC solution assumes nested magnetic surfaces within the plasma. This is even more pronounced in the puncture plot calculated at $t = 110$ sec, where the $5/5$ island now appears between $s = 0.65 - 0.75$, again consistent with the estimated rotational transform profile (see left frame of Fig. 5.1, in green) but very odd, given the aforementioned VMEC constraints.

The reason why these magnetic islands appear inside of the plasma seems to be a side effect of an additional corrective procedure that is applied within the VMEC+EXTENDER combo to remove magnetic field discontinuities at $s = 1$, although the details of how this exactly happens remain under investigation [47]. These discontinuities appear, in the calculation previously described, because the contribution to the magnetic field coming from the external coils is calculated differently inside the plasma (where the VMEC solution already includes this contribution) and in the "vacuum region" that extends from the last flux surface VMEC considers to the vacuum vessel (where Biot-

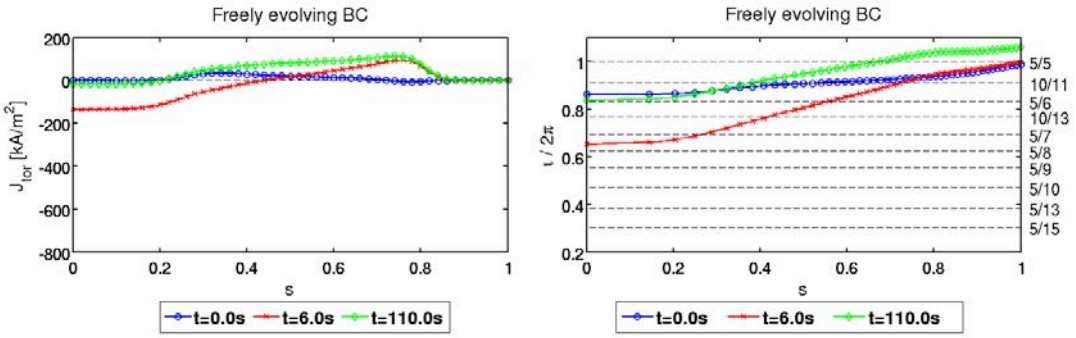

Figure 5.1: Toroidal current density (left) and rotational transform (right) radial profiles at selected times for the freely-evolving bootstrap current case described in the main text. Profiles are shown for three different times as the plasma $< \beta >$ is raised from 0.86% (at $t = 0$) to about $< \beta > \approx 2.0\%$ ($t = 6$ sec). The radial label used is $s = \sqrt{\psi/\psi_{edge}}$.

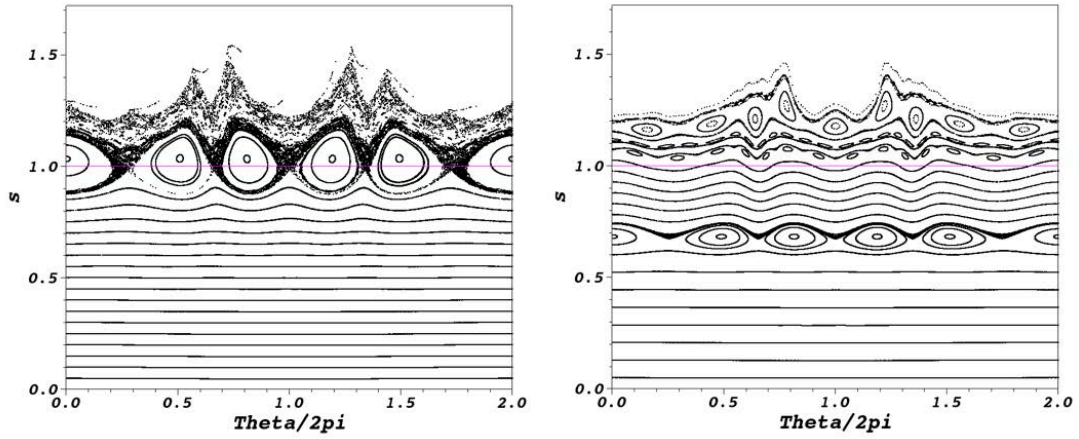

Figure 5.2: Poincaré plots (in SIESTA coordinates) of the magnetic field obtained by the VMEC+EXTENDER combo, for the freely-evolving bootstrap case, calculated at toroidal angle $\phi = 0$ at times $t = 6$ sec and $t = 110$ sec. A magenta line marks the plasma edge at $s = 1$.

Savart's law is integrated directly using the MAG3D code). Naturally, it would be better to add contributions that are calculated in the same way over the whole plasma+vacuum domain. Therefore, the creators of VMEC+EXTENDER decided to invoke again the "virtual casing principle", that was previously used to estimate the magnetic field created by the plasma currents in the vacuum region, and estimate with it the magnetic field created *by the external coils inside the plasma*[30]. This contribution is then subtracted from the VMEC solution and replaced by the magnetic field obtained by integrating over the plasma region Biot-Savart's law using the external coil currents. The Poincaré plots that result from these corrections are the ones shown in Fig. 5.2.

It is also worth mentioning that the solution obtained by the VMEC+EXTENDER combo is not a self-consistent MHD equilibrium, as recognized by its developers[30]. Inside $s = 1$, the plasma

pressure is still the one that VMEC obtained. That is, a flux quantity with respect to VMEC's magnetic field. The magnetic field topology, however, may have changed inside of the VMEC-domain (e.g., islands may have appeared) due to the corrective procedures just described. In principle, this would change the pressure distribution and, consequently, the plasma current distribution. In turn, this would also affect the fields outside of the VMEC domain that had been calculated on the basis of the unaltered plasma currents. The extent to which the VMEC+EXTENDER combo will provide a sufficiently good approximate solution over the whole plasma+vacuum volume will then depend on how important these effects are, that is clearly case-dependent. It is here that SIESTA should be able to help, as we will show soon.

We conclude this section by making a few more comments about the puncture plots shown in Fig. 5.2. They have to do with the fact that, in spite of the three low-order rational surfaces (i.e., $10/11, 5/6$ and $5/7$) that entered the plasma from the axis at $t = 6$ sec, no island chains seem to have formed in the magnetic field provided by VMEC+EXTENDER. Or if they have, they are extremely small and missed by the resolution of the puncture plot. Similarly, at $t = 110$ sec there is no sign of any rational surface inside the plasma except for the $5/5$ island chain at $s \sim 0.7$.

5.2.2 ECCD compensated bootstrap current case

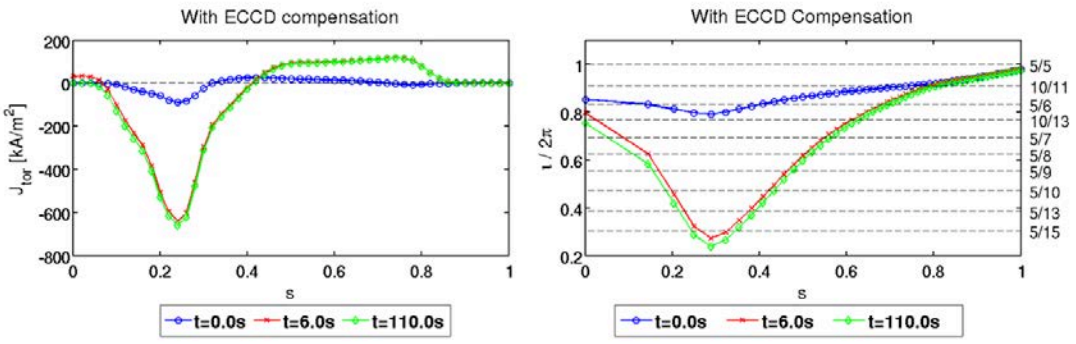

Figure 5.3: Toroidal current density (left) and rotational transform (right) radial profiles at selected times for the ECCD-compensated case described in the main text.

In order to avoid the $5/5$ island chain entering into the plasma because of freely evolving bootstrap currents, W7-X scientists have considered several scenarios to compensate the self-generated bootstrap currents by applyingh ECCD. The right frame of Fig. 5.3 shows the compensated toroidal current profiles that were obtained by means of the controlled use of Electron Cyclotron Current Drive for a particular W7-X experimental scenario, as reported in Refs. [40,41]. The guiding principle here was to compensate the expected bootstrap current with ECCD to make the net toroidal current vanish. In this way, the $5/5$ island chain would remain at its location and its role in the divertor op-

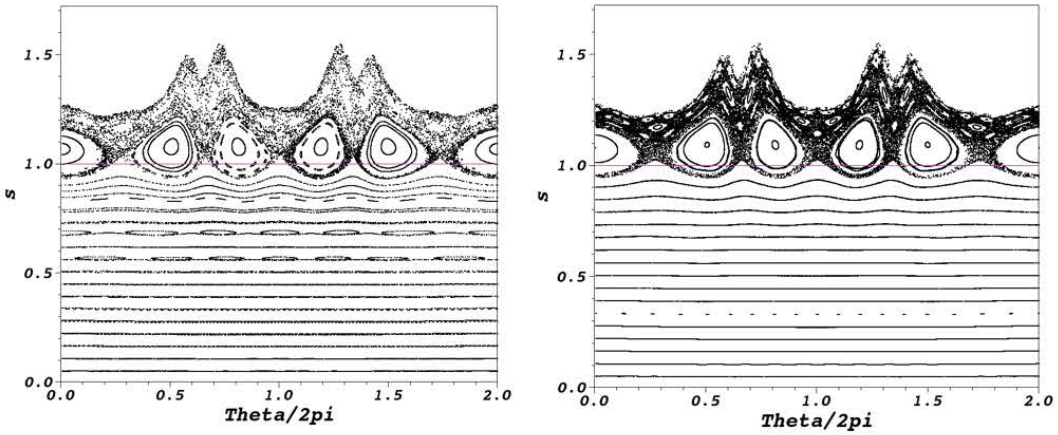

Figure 5.4: Poincaré plots (in SIESTA coordinates) of the magnetic field obtained by the VMEC+EXTENDER combo, for the ECCD compensated case, calculated at toroidal angle $\phi = 0$ at times $t = 6$ sec and $t = 110$ sec. The magenta line marks the plasma edge at $s = 1$.

eration would be unchallenged. However, since ECCD drives the current at the heating location and the boostrap current is driven by the gradients of the plasma profiles, a full compensation of the local current densities is not possible. ECCD is a very localized current drive scheme and a pure on-axis current drive would formally drive the rotational transform to negative values as seen in experiments in W7-AS[7°]. Therefore, an off-axis scenario was chosen here (see left frame of Fig. 5.3)), that led to an off-axis minimum of the rotational transform profile (see right frame of Fig. 5.3). As a result, a number of low-order rational surfaces (in particular, rationals $5/6, 10/13, 5/7, 5/8, 5/9, 5/10$, $5/13$ and $5/15$) made their way into the plasma through the axis, many of them even becoming doubly resonant (that is, being resonant at two different radial positions).

The effect of the ECCD compensation on the magnetic field topology can again be estimated by means of VMEC+EXTENDER. The Poincaré plots of the obtained magnetic field are shown in Fig. 5.4. Since the rotational transform profile is virtually the same at $t = 6$ sec and $t = 100$ sec, the puncture plots are also very similar. Both contain a large $5/5$ island chain at the plasma edge (again, with the island extending inside $s = 1$ for the reasons previously mentioned). Inside $s = 1$, well-defined magnetic surfaces are present almost everywhere. There are some hints of magnetic islands for the $t = 6$ case, though, particularly at $s \sim 0.68$ and $s \sim 0.55$, corresponding to the locations of the $5/6$ and $5/7$ rationals. At $t = 110$ sec, these rationals do not seem to be present in spite of the rotational transform profile being very similar. If the VMEC+EXTENDER estimate for the magnetic field inside the plasma could be trusted, these results would clearly be very good news. They would suggest that ECCD compensation schemes could be certainly used to control the location of the island divertor in W7-X .

5.3 Free-Boundary SIESTA analysis of the considered W7-X scenarios

In this section we will re-examine the two cases just considered in the previous section (i.e., the freely-evolving vs the compensated bootstrap cases) using the newly developed free-plasma-boundary version of SIESTA. SIESTA[54,81] is a nonlinear ideal MHD equilibrium code that lets the plasma pressure and magnetic field evolve freely, subject only to the local MHD conservation laws (of toroidal and poloidal magnetic flux and mass) and proper boundary conditions[81], until a minimum of the confined MHD energy,

$$W^{\mathrm{MHD}} = \int_{\mathrm{plasma+vaccum}} dV \left(\frac{B^2}{2\mu_0} + \frac{p}{\Gamma - 1} \right), \tag{5.1}$$

is reached, Γ being the adiabatic index. As a result, the magnetic field may develop any desired topology consistent with these constraints. Although SIESTA is an ideal MHD solver, it allows for a finite amount of resistivity at the start of its iteration cycle to help diffuse any divergent current present at rational surfaces, that is then set to zero before it converges to the final equilibrium solution[54]. The initial magnetic fields from which SIESTA starts to iterate are built from the plasma currents that VMEC finds for the same problem plus those flowing in the coils. Regarding the initial plasma pressure, it is that of the VMEC solution for $s < 1$. In addition, a very low-density plasma is also considered to fill the "vacuum region" that extends between the last closed flux surface considered in the VMEC solution and the vacuum vessel in order to avoid the formation of a large kernel in the Hessian matrix of the discretized numerical problem, that would complicate enormously the convergence towards a final solution (see explanation in Ref. [81]).

5.3.1 Freely evolving bootstrap current case

SIESTA has been first run for the W7-X freely-evolving bootstrap current case described in the previous section (more details about how SIESTA is run for W7-X in free-plasma-boundary mode can be found in Ref. [81]). The VMEC runs used to initialize SIESTA included 49 radial surfaces, 21 poloidal modes and 33 toroidal modes. They are, in fact, the same that were used within the VMEC+EXTENDER procedure described in the previous section. In addition, 34 new surfaces have been included to cover the vacuum region that goes from the plasma edge to the vacuum vessel. The number of Fourier modes, however, has remained the same. No additional resonant magnetic perturbations have been included during the run. Only a finite resistivity has been allowed in the first few nonlinear iterations in order to let unstable rational surfaces break up and reconnect. After this initial phase, the resistivity is set back to zero so that convergence to a final solution can be achieved[54]. Typically, convergence is declared when the normalized residual force becomes of the order of $< F^2 > \sim 10^{-18} - 10^{-20}$, which typically requires a few hours for a problem of this size.

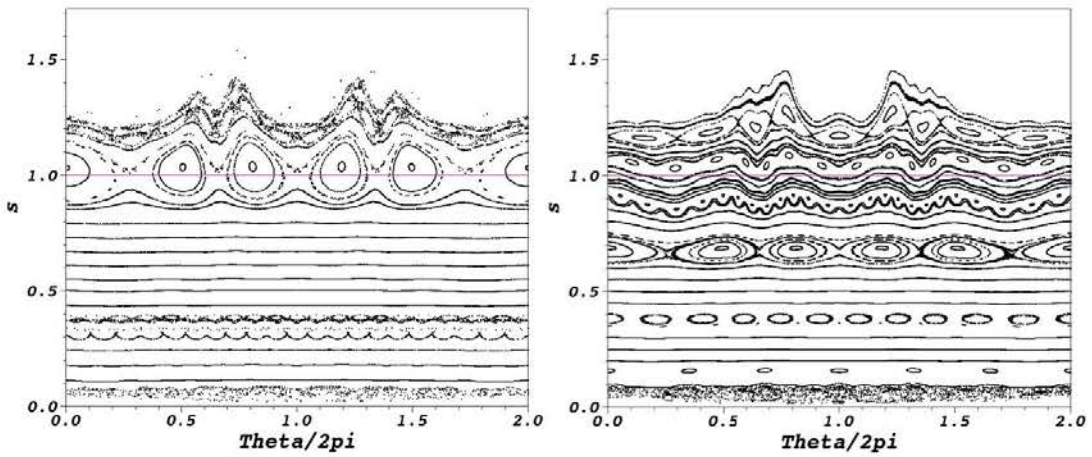

Figure 5.5: Poincaré plots (in SIESTA coordinates) of the equilibrium magnetic field obtained by SIESTA, for the freely-evolving bootstrap current case, at toroidal angle $\phi = 0$ for times $t = 6$ sec and $t = 110$ sec. The magenta line marks the plasma edge at $s = 1$.

The topology of the magnetic field obtained by SIESTA for the freely-evolving bootstrap current case is shown in Fig. 5.5, where Poincaré plots for the magnetic field are shown at times $t = 6$ and $t = 100$ sec. These puncture plots should be compared with those that were obtained by the VMEC+EXTENDER combo, shown in Fig. 5.2. The first thing that one appreciates is that the main features are similar, particularly outside of the plasma (i.e., for $s > 1$). For instance, the $5/5$ island chain is found at the plasma edge at $t = 6$ sec, although it is perhaps a bit wider in the case of the SIESTA solution. At $t = 100$ sec, on the other hand, the $5/5$ chain has entered the plasma and is now located at around $s \sim 0.65 - 0.75$, almost at the same position where it was in the VMEC+EXTENDER solution. One can also see the $15/14$ and $10/9$ rationals in the extended region between the plasma and the vacuum vessel at $t = 110$ sec in both solutions.

The largest differences appear however inside of the plasma, since magnetic islands were barely present in the VMEC+EXTENDER solution but, in the SIESTA case, small-width island chains are seen at $s \sim 0.4$ (where the $10/13$ rational sits). At time $t = 110$, some other island chains are seen close to $s \sim 0.2$ (probably, related to the $5/7$ rational), together with a small stochastic region at about $s = 0.1$. In spite of these differences, the expected impact on confinement seems to be similarly small in both the SIESTA and the VMEC+EXTENDER solutions due to fact that these islands are pretty small (one should probably check whether they are sufficiently large as to seed any neoclassical tearing modes. This is outside of the scope of this paper, though.). This is probably due to the fact that, in this configuration, the magnetic shear is sufficiently low to keep low-order rationals separated and sufficiently large to keep their size small. As a result, the well-known Chirikov's resonance-overlap criterion [23] is not violated, and stochastization does not take place.

5.3.2 ECCD compensated bootstrap current

Next, we re-examine with SIESTA the ECCD compensated bootstrap current case described earlier. SIESTA has been run here with the same number of radial surfaces and Fourier modes as before, using the same initialization procedure. The magnetic field of the converged MHD equilibrium solution is once more examined by means of Poincaré plots. These are shown in Fig. 5.6 for the two times $t = 6$ sec and $t = 100$ sec. These puncture plots should be compared to those calculated with the VMEC+EXTENDER combo for the ECCD compensated scenario, that are shown in Fig. 5.4.

The SIESTA results confirm part of what was found by VMEC+EXTENDER. Namely, that the very small net toroidal current left after the compensation clamps the location of the $5/5$ island chain to the plasma edge. However, important differences are seen with respect to the VMEC+EXTENDER solution in the region $0.15 < s < 0.45$. As will be remembered, this is the region where the rotational transform contained a larger number of low-order rational surfaces due to the counter-flowing ECCD current. In the VMEC+EXTENDER case, these resonances seemed to have no significant effect on the magnetic topology. SIESTA, however, finds that the region within $0.1 < s < 0.35$ becomes stochastic. This outcome is in fact not too surprising, given the large number of low-order rationals packed in this region that, being doubly resonant (in particular, rationals $5/9$, $5/10$, $5/13$ and $5/15$), are thus susceptible to the onset of double-tearing instabilities[12]. The puncture plot indeed suggests that Chirikov's resonance-overlap criterion[23] is probably violated over the $0.10 < s < 0.35$ region, resulting in stochastization. This is indeed an undesired outcome, since plasma profiles should be expected to become radially flattened across the stochastic region, thus leading to a considerable deterioration of confinement.

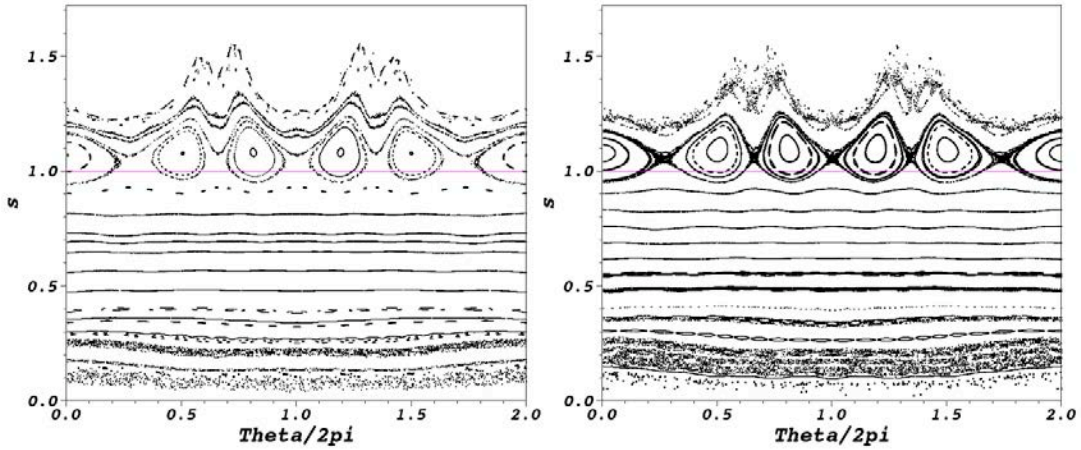

Figure 5.6: Poincaré plots (in SIESTA coordinates) at toroidal angle $\phi = 0$ of the magnetic field obtained at times 6.0s and 110.0 by SIESTA, for the ECCD compensated case. The green contour marks the vacuum vessel while the magenta dashed line marks the plasma edge at $s = 1$.

5.4 Summary and conclusions

A re-analysis of W7-X ECCD-compensated bootstrap-current scenarios has shown that the free-boundary-version of the SIESTA code can be very useful to assess the effects that freely evolving currents might have on the topological properties of the confining 3D magnetic fields, both within the plasma and in the region between the plasma and the vacuum vessel. In the case examined in this paper, it has been found that although the initial goal of keeping the W7-X island divertor clamped at the plasma edge is indeed achievable by means of off-axis ECCD, it can lead to modifications of the rotational transform profile inside the plasma that could lead to strong confinement deterioration and that should be avoided. SIESTA can help in determining when this is indeed the case. Clearly, for the scenario examined here, broader deposition profiles might be required to drive a less peaked toroidal current density near the axis, whilst still keeping the net toroidal current as close to zero as possible. Rational surface packing could then be avoided in this manner, thus preventing stochastization. An optimization of the deposition and current drive profiles might be possible since the W7-X ECRH-system is quite flexible but an exploration of this is, as the exploration of other additional strategies for bootstrap current control, outside of the scope of this paper. We conclude by saying that, in our opinion, the use of SIESTA could also be advantageous in other problems that need to deal with magnetic topologies other than just nested magnetic surfaces, such as when studying the effects of applying resonant magnetic perturbations[31] or while assessing the consequences of significant error fields[66].

Acknowledgements

Research funded in part by the Spanish National Project No. ENE2015-68265. Research carried in part at the Max-Planck-Institute for Plasma Physics in Greifswald (Germany), whose hospitality is gratefully acknowledged. SIESTA free-boundary runs have been carried out in *Uranus*, a supercomputer cluster located at Universidad Carlos III de Madrid and funded jointly by EU-FEDER funds and by the Spanish Government via the National Projects No. UNC313- 4E-2361, No. ENE2009-12213-C03-03, No. ENE2012-33219, and No. ENE2012-31753.

6
Conclusions

In this work we have developed a free-plasma-boundary version of the ideal MHD 3D code *SIESTA* and applied it to the W7-X stellarator, a relevant experiment for the fusion community at the time of writing this thesis. The development of this version of *SIESTA* has been tailored for the W7-X , though it has been implemented in such a way that it is easy to expand to any other experiment.

The new version was built as a external code which complements the original *SIESTA* code, which was varied only slightly to ensure the proper coupling of the new input. For this reason we have developed two external codes to obtain the necessary input for the extended *SIESTA* version. As explained in chapter 4, *SIESTA* needs three basic inputs, namely a background numerical mesh, a good approximation for the magnetic field and a pressure profile for the volume considered. As was mentioned earlier, the process of building the magnetic field depends on an external code, which is why two codes are needed, one before the external code and a second one after. As a result of this combination of codes, the process for an extended *SIESTA* run is as follows:

1. Run *VMEC* to obtain its solution, which provides the background mesh for $s < 1$.
2. Run the *XTEND* code to extend the numerical mesh from *VMEC*'s to an outer surface.
3. Obtain the magnetic potential vector for the experiment on the 3rd and last surfaces.
4. Run the *REPACK* code to generate the input for *SIESTA* having three inputs: *VMEC*'s `wout` file, a file containing the Fourier modes of the extended mesh and the file containing the magnetic potential for the required surfaces.
5. Run *SIESTA* with the flag `l_extension` set to `True`.

In our case, for the external surface we have used the vacuum vessel of the W7-X , as explained in chapter 4. The surface to which the mesh is extended is provided in a separate file, so it is easy to adapt the code to another machine, the only requirement being to have a file with the Fourier harmonics (R_{mn} for a cosine series and Z_{mn} for a sine series) for the corresponding outer surface. The magnetic vector potential has been provided by the *MAG3D*, as explained in chapter 4, which means that for adapting the extension to another machine, an equivalent code is necessary. The rest of the process is valid for any machine.

The complete process takes more or less 12 hours for the W7-X , running everything except *SIESTA* in a single processor, *SIESTA* is run in 16 XEON processors of the E5 family. Depending on the equilibrium it might take as little as 6 hours or as much as 24 hours, again for the W7-X which has a complex geometry. This might be considerably reduced when considering simpler geometries. The process has been automated through a Python script which makes the calls to all the different codes.

The main conclusion of this work is that *SIESTA* works in free-plasma-boundary mode. In addition, we have demonstrated that the pseudo-vacuum region between plasma and first wall can be analysed with *SIESTA* in a number of relevant situations. Through this new version of *SIESTA* it is possible to study equilibria which include ergodic regions and/or magnetic islands, in a quasi free-boundary manner. The advantage brought to the fusion community is the possibility to study the behaviour of plasma and its interaction with the external magnetic field past the last closed flux surface. As we have seen in this work, this is extremely useful for the particular case of the W7-X , though we expect *SIESTA* to be useful for tokamaks as well. In particular, since ELM control techniques rely on adding resonant magnetic perturbations very close to the plasma edge, which should lead to LCFS modifications.

We would like to end this manuscript with a few words about future research. As mentioned at the beginning of this chapter, this work has been tailored for the W7-X , which means that there is some work needed to be done in order to generalise its application to other experiments. Namely, the work which is being taken as a natural next step is to implement a subroutine to extract information about the magnetic vector potential from the `mgrid` file used by *VMEC* when it runs in free-boundary mode. This would make the extension process completely independent and a complete standalone version of the extended *SIESTA* code could be offered.

The algorithms and methods implemented in the developed codes might be improved, some research is needed in order to make the process more efficient and to try and improve the approach taken here.

Conclusiones

En este trabajo hemos desarrollado una versión frontera de plasma libre del código tri-dimensional de MHD ideal SIESTA y lo hemos aplicado al stellarator W7-X , un experimento relevante para la comunidad de investigadores de fusión nuclear por confinamiento magnético en el momento de escritura de esta tesis. El desarrollo de esta nueva versión de SIESTA ha sido ajustado para el W7-X , aunque ha sido implementado de manera tal que sea fácilmente aplicado a otros dispositivos.

La nueva versión fue construida como un código externo que complementa la versión original de SIESTA. Como se ha explicado en el capítulo 4, SIESTA necesita tres datos de entrada básicos, a saber: una malla numérica, una buena aproximación para el campo magnético y un perfil de presión en esa malla. Como fue mencionado anteriormente, el proceso de construir el campo magnético depende de un código externo, razón por la cual el código externo que complementa a SIESTA ha sido dividido en dos, una parte antes y otra después de la llamada al código externo. Como resultado de esta combinación de códigos, el proceso para correr SIESTA en su nueva versión extendida procede de la siguiente manera:

1. Correr *VMEC*, cuya solución provee la malla numérica para $s < 1$.
2. Correr el código *XTEND* para extender la malla numérica desde la de *VMEC* hasta una superficie exterior.
3. Obtener el vector de potencial magnético para la 3ra y última superficies.
4. Correr el código *REPACK* para generar los datos de entrada de *SIESTA*, teniendo tres entradas: el archivo `wout` de *VMEC*, un archivo conteniendo los modos de Fourier para la malla extendida y el archivo con el vector potencial magnético para las superficies requeridas.
5. Correr *SIESTA* con el indicativo `l_extension` establecido como `True`.

En nuestro caso, para la superficie externa, hemos utilizado la cámara de vacío del W7-X , como se explicó en el capítulo 4. La superficie hasta la cual se realiza la extensión de la malla numérica se provee en un archivo separado, por lo que es fácil adaptar el código a otra máquina, el único requerimiento siendo el disponer de un archivo con los modos Fourier (R_{mn} para serie de cosenos y Z_{mn} para serie de senos) para la superficie correspondiente. El vector de potencial magnético (paso 3) ha sido obtenido mediante *MAG3D*, como se mencionó en el capítulo 4, lo que significa que

un código equivalente es necesario para poder adaptar esta versión de *SIESTA* a otro dispositivo toroidal de confinamiento magnético. El resto del proceso es válido para cualquier máquina.

El proceso completo toma alrededor de 12 horas para el W7-X , corriendo todo menos *SIESTA* en un solo procesador; *SIESTA* se corre en 16 procesadores XEON de la familia E5. Dependiendo en el equilibrio puede tomar tan poco como 6 horas o tanto como 24 horas, pero de nuevo recordamos al lector de la complicada geometría del W7-X . Estos tiempos se pueden ver considerablemente reducidos para geometrías más sencillas. El proceso se ha automatizado mediante un script en Python que realiza las llamadas a los diferentes códigos.

El resultado principal de este trabajo es que *SIESTA* trabaja en modo frontera de plasma libre. Además, hemos demostrado que la región de pseudo-vacío entre el plasma y la primera pared interna se puede analizar con *SIESTA* para un número de situaciones relevantes. Mediante esta nueva versión de *SIESTA* es posible analizar equilibrios que incluyen regiones ergódicas y/o islas magnéticas en una manera similar a la frontera-libre. La ventaja que esto conlleva para la comunidad de fusión es la posibilidad de estudiar el comportamiento del plasma y su interacción con el campo magnético externo, más allá de la última superficie cerrada. Como se ha demostrado en este trabajo, esto es de extrema utilidad para el caso particular del W7-X , aunque también esperamos que *SIESTA* sea útil para tokamaks. En particular, debido a que las técnicas de control de ELMs se basan en añadir perturbaciones magnéticas resonantes muy cerca del borde del plasma, que debiera llevar a la modificación de la LCFS.

Nos gustaría acabar este manuscrito, con unas breves palabras sobre trabajo futuro. Como se mencionó al inicio de este capítulo, este trabajo se ha desarrollado ajustándolo específicamente al W7-X , lo que significa que hay aún trabajo pendiente para poder generalizar su aplicación a otros experimentos. Específicamente, el trabajo que se ve como un paso natural a seguir es la implementación de una subrutina para obtener información acerca del vector potencial magnético a partir del archivo `mgrid` utilizado por *VMEC* cuando corre en modo frontera-libre. Esto haría el proceso de extensión completamente independiente y se podría ofrecer una versión de *SIESTA* sin dependencias en otros códigos.

Los métodos y algoritmos implementados en los códigos desarrollados se podrían mejorar, se debe realizar estudios para lograr que el proceso sea más eficiente.

Conclusies

In dit werk ontwikkelden we een vrije plasmawand versie van de ideale MHD 3D code *SIESTA*, die we dan toepasten op de W7-X stellarator, een relevant experiment in de fusiegemeenschap op het moment van schrijven van deze thesis. De ontwikkeling van deze versie van *SIESTA* werd op maat gemaakt voor de W7-X , maar de implementatie gebeurde op een manier die makkelijk uitbreidbaar is naar eender welk ander experiment.

De nieuwe versie werd gebouwd als een externe code die de originele *SIESTA* code complementeert, waarbij *SIESTA* zelf maar zeer weinig veranderd moest worden voor de koppeling met de nieuwe input. Voor deze reden hebben we twee externe codes ontwikkeld die de nodige inputs van de uitgebreide *SIESTA* code binnen halen. Zoals uitegelegd in hoofdstuk 4, heeft *SIESTA* drie basis inputs nodig, met name een achtergrondmaas, een goede benadering van het magnetische veld en een drukprofiel voor het volume onder consideratie. Zoals eerder vermeld hangt het proces van het bouwen van het magnetische veld af van een externe code, wat de reden is waarom twee codes nodig zijn: één voor de externe code en één na de externe code. Als resultaat van deze combinatie van codes ziet een uitgebreide *SIESTA* simulatie er nu zo uit:

1. Run *VMEC* om een oplossing te bekomen, die een achtergrondmaas verschaft voor $s < 1$.
2. Run de *XTEND* code die het numerieke maas van *VMEC* uibreid naar een extern oppervlak.
3. Verkrijg de magnetische vectorpotentieel voor het experiment op de laatste en derde laatste oppervlakken.
4. Run de *REPACK* code die de invoer voor *SIESTA* genereert, op basis van drie inputs: van *VMEC*'s `wout` bestand, van een bestand dat de Fouriermodes van het uitgebreide maas bevat, en van een een bestand dat de magnetische vectorpotentieel van de benodigde oppervlakken bevat.
5. Run *SIESTA* met de optie `l_extension`.

In ons geval gebruikten we als externe oppervlak het oppervlatkte van het vacuümvat van W7-X , zoals uitgelegd werd in hoofdstuk 4. Het oppervlak naar waar onze maas werd uitgebreid moet worden aangeleverd in een appart bestand, zodat het makkelijk aanpasbaar is voor een andere machine. Dit bestand moet enkel de Fourier harmonischen bevatten (R_{mn} voor een cosinusserie en Z_{mn} voor

een sinusserie) voor het laatste externe oppervlak. De magnetische vectorpotentieel werd aangeveleerd door de *MAG3D* code, zoals uitgelegd werd in hoofdstuk 4, wat erop neer komt dat een equivalente code nodig zou zijn voor de uitbreiding naar een andere machine. De rest van het proces is geldig voor elke machine.

Het complete proces duurt min of meer 12 uren voor W7-X , waarbij alles behalve *SIESTA* op een enkele processor runt. *SIESTA* zelf loopt op 16 XEON processoren van de E5 familie. Afhankelijk van het evenwicht kan dit tussen 6 en 24 uren duren, voor de complexe W7-X geometrie. Dit alles kan aanzienlijk verminderd worden voor simpelere geometriëen. Het hele process is geautomatizeerd in een Python script dat alle codes aanroept.

De belangrijkste conclusie van dit werk is dat de *SIESTA* code nu werkt in een vrije plasmawandmodus. Hiernaast hebben we ook aangetoond dat de pseudo-vacüumregio tussen plasma en wand kan worden geanalyzeerd in *SIESTA* voor meerdere relevante scenario's. Met deze nieuwe versie van *SIESTA* is het nu mogelijk om evenwichten te bestuderen die ergodische regio's en/of magnetische eilanden bevatten, met een quasi-vrije oppervlak. Het voordeel voor de fusiegemeenschap is de mogelijkheid om het gedrag van het plasma en haar interactie met de externe magnetische velden buiten het laatste gesloten fluxoppervlak ('Last Closed Flux Surface', LCFS), te bestuderen. Zoals we gezien hebben in dit werk, is dit zeer nuttig voor de W7-X configuraties, maar we verwachten dat dit ook nuttig zal zijn voor tokamaks. ELM controletechnieken, in het bijzonder, leiden tot LCFS modificaties, aangezien bij deze technieken resonante magnetische perturbaties worden gebruikt, dicht bij de plasmawand.

We zouden dit manuscript graag beëindigen met een paar woorden in verband met verder onderzoek. Zoals vermeld in het begin van dit hoofdstuk, is dit werk op maat gemaakt voor W7-X , wat impliceert er nog wat moet gebeuren om dit te veralgementen naar andere experimenten. De meest logische volgende stap hierbij is de implementatie van een subroutine die informatie over de magnetische vectorpotentieel uit het `mgrid` bestand haalt, dat gebruikt wordt door *VMEC* als het in vrije wandmodus gebruikt wordt. Dit zal het extensieproces van *SIESTA* compleet onafhankelijk maken en zo zal een complete stand-alone versie van *SIESTA* aangeboden kunnen worden.

De modellen die werden gebruikt in de codes kunnen ook verbeterd worden en onderzoek is nodig om het proces meer efficiënt te maken en om de algemene strategie gebruikt in dit werk nog te verbeteren.

Hugo A. Peraza Rodriguez

linkedin.com/in/hperaza

Studies

- **Universidad Carlos III de Madrid - Universiteit Gent** **Madrid, Spain / Gent, Belgium**
  Ph.D. in Plasma Physics and Nuclear Fusion *Sept. 2012 – [Dec.] 2017*
- **CINECA Supercomputing Center** **Bologna, Italy**
  22nd Summer School on Parallel Computing *20th - 30th May, 2013*
- **Universiteit Gent** **Gent, Belgium**
  M.Sc. in Nuclear Fusion Science and Engineering Physics *Sept. 2010 – Aug. 2012*
- **Universidad de Costa Rica** **San Jose, Costa Rica**
  B.Sc. in Physics *Feb. 2003 – Aug. 2008*

Experience

- **Universidad Nacional** **Heredia, Costa Rica**
  Instructor for Introductory Physics courses *Sept. 2008 – July 2010*
- **Universidad de Costa Rica** **San Jose, Costa Rica**
  Instructor for Introductory Physics courses *Jan. 2009 – July 2010*

Conferences and Publications

- **Plasma Physics and Controlled Fusion Journal** **Submitted, Sept. 2017**
  Bootstrap current control studies in the Wendelstein 7-X stellarator using the free-plasma-boundary version of the SIESTA MHD equilibrium code
  H. Peraza-Rodriguez, J.M. Reynolds-Barredo, R. Sanchez, J. Geiger and V. Tribaldos
- **Journal of Computational Physics** **Aug. 2017, vol. 24 (8), page 082516**
  Extension of the SIESTA MHD equilibrium code to free-plasma-boundary problems
  H. Peraza-Rodriguez, J.M. Reynolds-Barredo, R. Sanchez, J. Geiger, V. Tribaldos, S.P. Hirshman and M. Cianciosa
- **APS Division of Plasma Physics Meeting 2016** **San Jose, CA, USA**
  Poster: Development of a free-boundary version of the SIESTA MHD equilibrium code *31st Oct - 4th Nov. 2016*
  H. Peraza-Rodriguez, R. Sanchez, J.M. Reynolds-Barredo, V. Tribaldos, J. Geiger, S.P. Hirshman and M. Cianciosa
- **5th PhD Event in Fusion Science and Engineering** **Prague, Czech Republic**
  Oral presentation: SIESTA and its free boundary development *16th - 17th Nov. 2015*
  H. Peraza-Rodriguez, R. Sanchez, J. Geiger, J.M. Reynolds-Barredo, V. Tribaldos and S.P. Hirshman

- **20th International Stellarator and Heliotron Workshop** **Greifswald,Germany**
  Poster: Application of the extended SIESTA code to the Wendelstein 7-X *5th - 9th Oct. 2015*
  H. Peraza-Rodriguez, R. Sanchez, J. Geiger, V. Tribaldos and J.M. Reynolds-Barredo

- **41st EPS Conference on Plasma Physics** **Berlin, Germany**
  Poster: Application of the SIESTA code to the calculation *23rd - 27th Jun. 2014*
  of MHD equilibria for the Wendelstein 7-X Stellarator
  H. Peraza-Rodriguez, R. Sanchez, J. Geiger, J.M. Reynolds-Barredo and V. Tribaldos

- **3rd PhD Event in Fusion Science and Engineering** **York, England**
  Poster: MHD equilibrium and stability analysis using the SIESTA code *24th - 26th Jun. 2013*
  H. Peraza-Rodriguez, R. Sanchez, J.M. Reynolds-Barredo and J. Geiger

- **2nd PhD Event in Fusion Science and Engineering** **Pont-à-Mousson, France**
  Poster: Adapting SIESTA for the study of MHD *22nd - 25th Oct. 2012*
  equilibrium and stability with the for W7-X
  H. Peraza-Rodriguez and R. Sanchez

References

[1] Abdelmalik, M. R. A. & van Brummelen, E. H. (2016). Moment closure approximations of the boltzmann equation based on ϕ-divergences. Journal of Statistical Physics, 164(1), 77–104.

[2] Aydemir, A. & Barnes, D. (1984). Three-dimensional nonlinear incompressible mhd calculations. Journal of Computational Physics, 53(1), 100–123.

[3] Baganoff, D. & Elliott, J. P. (1975). Development of closure relations in kinetic theory. Canadian Journal of Physics, 53(13), 1301–1303.

[4] Balescu, R. (1988). Classical Transport. Transport Processes in Plasmas. Amsterdam, The Netherlands: North-Holland.

[5] Balescu, R. (2005). Aspects of Anomalous Transport in Plasmas. Series in Plasma Physics. Bristol, U.K.: Institute of Physics Publishing.

[6] Bauer, F., Betancourt, O., & Garabedian, P. (1978). A Computational Method in Plasma Physics. Springer series in computational physics. New York, USA: Springer-Verlag.

[7] Beidler, C., Grieger, G., Herrnegger, F., Harmeyer, E., Kißlinger, J., Lotz, W., Maaßberg, H., Merkel, P., Nührenberg, J., Rau, F., Sapper, J., Sardei, F., Scardovelli, R., Schlüter, A., &

Wobig, H. (1990). Physics and engineering design for wendelstein vii-x. Fusion Technology, 17(1), 148–168.

[8] Betti, R. & Hurricane, O. A. (2016). Inertial-confinement fusion with lasers. Nature Physics, 12(5), 435–448. Review.

[9] Bhattacharjee, A., Hayashi, T., Hegna, C. C., Nakajima, N., & Sato, T. (1995). Theory of pressureâ□□induced islands and selfâ□□healing in threeâ□□dimensional toroidal magnetohydrodynamic equilibria. Physics of Plasmas, 2(3), 883–888.

[10] Bickerton, R., Connor, J., & Taylor, J. (1971). Diffusion driven plasma currents and bootstrap tokamak. Nature Physical Science, 229, 110–112.

[11] Binns, C. & Low, W. Y. (2017). Fukushima disaster. Asia Pacific Journal of Public Health, 29(2_suppl), 5S–6S. PMID: 28330406.

[12] Biskamp, D. (2000). Magnetic Reconnection in Plasmas. Cambridge Monographs on Plasma Physics. Cambridge University Press.

[13] Biskamp, D. & Drake, J. F. (1994). Dynamics of the sawtooth collapse in tokamak plasmas. Phys. Rev. Lett., 73, 971–974.

[14] Blandford, E. D. & Ahn, J. (2012). Examining the nuclear accident at fukushima daiichi. Elements, 8(3), 189–194.

[15] Boozer, A. H. (1981). Plasma equilibrium with rational magnetic surfaces. The Physics of Fluids, 24(11), 1999–2003.

[16] Boyd, T. & Sanderson, J. (2003). The Physics of Plasmas. Cambridge, U.K.: Cambridge University Press.

[17] Boyle, A. (2016). Nuclear fusion gets boost from private-sector startups. https://www.sciencenews.org/article/nuclear-fusion-gets-boost-private-sector-startups. Last checked 14.06.2017.

[18] Callen, J. & Homma, T. (2017). Lessons learned in protection of the public for the accident at the fukushima daiichi nuclear power plant. Health Physics, 112(6), 550–559.

[19] Callen, J. D. & Dory, R. A. (1972). Magnetohydrodynamic equilibria in sharply curved axisymmetric devices. The Physics of Fluids, 15(8), 1523–1528.

[20] Canik, J., Hirshman, S., Sanchez, R., Maingi, R., Ahn, J.-W., Bell, R., Diallo, A., Gerhardt, S., LeBlanc, B., Menard, J., Park, J.-K., Podesta, M., & Sabbagh, S. (2012). First use of three-dimensional equilibrium, stability and transport calculations for interpretation of elm triggering with magnetic perturbations in nstx. Nuclear Fusion, 52(5), 054004.

[21] Castejón, F., López-Bruna, D., Estrada, T., Ascasíbar, E., Zurro, B., & Baciero, A. (2004). Influence of low-order rational magnetic surfaces on heat transport in tj-ii heliac ecrh plasmas. Nuclear Fusion, 44(5), 593.

[22] Chen, F. (1984). Introduction to Plasma Physics and Controlled Fusion. New York, USA: Springer US, 2 edition.

[23] Chirikov, B. V. (1979). A universal instability of many-dimensional oscillator systems. Physics Reports, 52(5), 263–379.

[24] Chodura, R. & Schlüter, A. (1981). A 3d code for mhd equilibrium and stability. Journal of Computational Physics, 41(1), 68–88.

[25] Chu, M. S., Chan, V. S., Politzer, P. A., Brennan, D. P., Choi, M., Lao, L. L., John, H. E. S., & Turnbull, A. D. (2006). Kinetic Alfvén wave and associated current drive at the center of tokamaks. Physics of Plasmas, 13(11), 114501.

[26] Cook, J., Nuccitelli, D., Green, S. A., Richardson, M., Winkler, B., Painting, R., Way, R., Jacobs, P., & Skuce, A. (2013). Quantifying the consensus on anthropogenic global warming in the scientific literature. Environmental Research Letters, 8(2), 024024.

[27] Cook, J., Oreskes, N., Doran, P. T., Anderegg, W. R. L., Verheggen, B., Maibach, E. W., Carlton, J. S., Lewandowsky, S., Skuce, A. G., Green, S. A., Nuccitelli, D., Jacobs, P., Richardson, M., Winkler, B., Painting, R., & Rice, K. (2016). Consensus on consensus: a synthesis of consensus estimates on human-caused global warming. Environmental Research Letters, 11(4), 048002.

[28] Dewar, R. & Hudson, S. (1998). Stellarator symmetry. Physica D: Nonlinear Phenomena, 112(1), 275 – 280.

[29] Dolan, T. (2000). Fusion Research. Oxford, U.K.: Pergamon Press.

[30] Drevlak, M., Monticello, D., & Reiman, A. (2005). PIES free boundary stellarator equilibria with improved initial conditions. Nuclear Fusion, 45(7), 731.

[31] Evans, T. E. (2015). Resonant magnetic perturbations of edge-plasmas in toroidal confinement devices. Plasma Physics and Controlled Fusion, 57(12), 123001.

[32] Evans, T. E., Moyer, R. A., Thomas, P. R., Watkins, J. G., Osborne, T. H., Boedo, J. A., Doyle, E. J., Fenstermacher, M. E., Finken, K. H., Groebner, R. J., Groth, M., Harris, J. H., La Haye, R. J., Lasnier, C. J., Masuzaki, S., Ohyabu, N., Pretty, D. G., Rhodes, T. L., Reimerdes, H., Rudakov, D. L., Schaffer, M. J., Wang, G., & Zeng, L. (2004). Suppression of large edge-localized modes in high-confinement diii-d plasmas with a stochastic magnetic boundary. Physical Review Letters, 92, 235003.

[33] Feng, Y., Beidler, C., Geiger, J., Helander, P., Hölbe, H., Maassberg, H., Turkin, Y., Reiter, D., & Team, W.-X. (2016). On the w7-x divertor performance under detached conditions. Nuclear Fusion, 56(12), 126011.

[34] Feng, Y., Sardei, F., Grigull, P., McCormick, K., Kißlinger, J., & Reiter, D. (2006). Physics of island divertors as highlighted by the example of W7-AS. Nuclear Fusion, 46(8), 807.

[35] Fitzpatrick, R. & Hender, T. C. (1991). The interaction of resonant magnetic perturbations with rotating plasmas. Physics of Fluids B: Plasma Physics, 3(3), 644–673.

[36] Freidberg, J. P. (1987). Ideal Magnetohydrodynamics. New York, USA: Plenum Press.

[37] Galeev, A. (1971). Diffusion-electrical phenomena in a plasma confined in a tokamak machine. Journal of Experimental and Theoretical Physics, 32(4), 752–757.

[38] Garnaut, R. (2008). The Garnaut Climate Change Review. Port Melbourne, VIC 3207, Australia: Cambridge University Press.

[39] Garren, D. A. & Boozer, A. H. (1991). Existence of quasihelically symmetric stellarators. Physics of Fluids B: Plasma Physics, 3(10), 2822–2834.

[40] Geiger, J., Beidler, C., Drevlak, M., Maaßberg, H., Nührenberg, C., Suzuki, Y., & Turkin, Y. (2010). Effects of net currents on the magnetic configuration of w7-x. Contributions to Plasma Physics, 50(8), 770–774.

[41] Geiger, J., Beidler, C. D., Feng, Y., Maaßberg, H., Marushchenko, N. B., & Turkin, Y. (2015). Physics in the magnetic configuration space of w7-x. Plasma Physics and Controlled Fusion, 57(1), 014004.

[42] Goedbloed, J. & Poedts, S. (2004). Principles of Magnetohydrodynamics. Cambridge CB2 8RU, United Kingdom: Cambridge university Press.

[43] Goldston, R. & Rutherford, P. (1995). Introduction to Plasma Physics. Bristol, U.K.: IOP Publishing.

[44] Grad, H. (1949). On the kinetic theory of rarefied gases. Communications on Pure and Applied Mathematics, 2(4), 331–407.

[45] Grieger, G., Lotz, W., Merkel, P., Nührenberg, J., Sapper, J., Strumberger, E., Wobig, H., Burhenn, R., Erckmann, V., Gasparino, U., Giannone, L., Hartfuss, H. J., Jaenicke, R., Kühner, G., Ringler, H., Weller, A., Wagner, F., the W7-AX Team, & the W7-AS Team (1992). Physics optimization of stellarators. Physics of Fluids B: Plasma Physics, 4(7), 2081–2091.

[46] Hanson, J. D. (2015). The virtual-casing principle and helmholtzâ□□s theorem. Plasma Physics and Controlled Fusion, 57(11), 115006.

[47] Hanson, J. D. (2016). Surface current on the plasma-vacuum interface in mhd equilibria. In 58th Annual Meeting of the Division of Plasma Physics of the APS San José, CA, USA. Poster No. GP10.00064.

[48] Helander, P., Geiger, J., & Maaßberg, H. (2011). On the bootstrap current in stellarators and tokamaks. Physics of Plasmas, 18(9), 092505.

[49] Hinton, F. L. & Hazeltine, R. D. (1976). Theory of plasma transport in toroidal confinement systems. Rev. Mod. Phys., 48, 239–308.

[50] Hirshman, S. & Betancourt, O. (1991). Preconditioned descent algorithm for rapid calculations of magnetohydrodynamic equilibria. Journal of Computational Physics, 96(1), 99–109.

[51] Hirshman, S., Schwenn, U., & Nührenberg, J. (1990). Improved radial differencing for three-dimensional magnetohydrodynamic equilibrium calculations. Journal of Computational Physics, 87(2), 396–407.

[52] Hirshman, S., van RIJ, W., & Merkel, P. (1986). Three-dimensional free boundary calculations using a spectral green's function method. Computer Physics Communications, 43(1), 143–155.

[53] Hirshman, S. P. & Meier, H. K. (1985). Optimized fourier representations for three-dimensional magnetic surfaces. Phys. Fluids, 28(5), 1387–1391.

[54] Hirshman, S. P., Sanchez, R., & Cook, C. R. (2011). Siesta: A scalable iterative equilibrium solver for toroidal applications. Physics of Plasmas, 18(6), 062504.

[55] Hirshman, S. P., Shafer, M. W., Seal, S. K., & Canik, J. M. (2016). Investigation of island formation due to rmps in diii-d plasmas with the siesta resistive mhd equilibrium code. Journal of Plasma Physics, 82(2).

[56] Hirshman, S. P. & Whitson, J. C. (1983). Steepest-descent moment method for three-dimensional magnetohydrodynamic equilibria. Physics of Fluids, 26(12), 3553–3568.

[57] Hölbe, H., Pedersen, T. S., Geiger, J., Bozhenkov, S., König, R., Feng, Y., Lore, J., Lumsdaine, A., & the Wendelstein 7-X Team (2016). Access to edge scenarios for testing a scraper element in early operation phases of wendelstein 7-x. Nuclear Fusion, 56(2), 026015.

[58] Hudson, S. R., Dewar, R. L., Dennis, G., Hole, M. J., McGann, M., von Nessi, G., & Lazerson, S. (2012). Computation of multi-region relaxed magnetohydrodynamic equilibria. Physics of Plasmas, 19(11), 112502.

[59] Inagaki, S., Tamura, N., Ida, K., Nagayama, Y., Kawahata, K., Sudo, S., Morisaki, T., Tanaka, K., & Tokuzawa, T. (2004). Observation of reduced heat transport inside the magnetic island o point in the large helical device. Phys. Rev. Lett., 92, 055002.

[60] Itskov, M. (2015). Tensor Algebra and Tensor Analysis for Engineers. Switzerland: Springer International Publishing.

[61] Jones, L. (2017). Renewable Energy Integration. United States: Academic Press.

[62] Klinger, T., Alonso, A., Bozhenkov, S., Burhenn, R., Dinklage, A., Fuchert, G., Geiger, J., Grulke, O., Langenberg, A., Hirsch, M., Kocsis, G., Knauer, J., Krämer-Flecken, A., Laqua, H., Lazerson, S., Landreman, M., Maaßberg, H., Marsen, S., Otte, M., Pablant, N., Pasch, E.,

Rahbarnia, K., Stange, T., Szepesi, T., Thomsen, H., Traverso, P., Velasco, J. L., Wauters, T., Weir, G., Windisch, T., & Team, T. W. .-X. (2017). Performance and properties of the first plasmas of wendelstein 7-x. Plasma Physics and Controlled Fusion, 59(1), 014018.

[63] Kruskal, M. D. & Kulsrud, R. M. (1958). Equilibrium of a magnetically confined plasma in a toroid. The Physics of Fluids, 1(4), 265–274.

[64] Lawson, J. D. (1957). Some criteria for a power producing thermonuclear reactor. Proceedings of the Physical Society. Section B, 70(1), 6.

[65] Lazarus, E. A., Navratil, G. A., Greenfield, C. M., Strait, E. J., Austin, M. E., Burrell, K. H., Casper, T. A., Baker, D. R., DeBoo, J. C., Doyle, E. J., Durst, R., Ferron, J. R., Forest, C. B., Gohil, P., Groebner, R. J., Heidbrink, W. W., Hong, R.-M., Houlberg, W. A., Howald, A. W., Hsieh, C.-L., Hyatt, A. W., Jackson, G. L., Kim, J., Lao, L. L., Lasnier, C. J., Leonard, A. W., Lohr, J., La Haye, R. J., Maingi, R., Miller, R. L., Murakami, M., Osborne, T. H., Perkins, L. J., Petty, C. C., Rettig, C. L., Rhodes, T. L., Rice, B. W., Sabbagh, S. A., Schissel, D. P., Scoville, J. T., Snider, R. T., Staebler, G. M., Stallard, B. W., Stambaugh, R. D., St. John, H. E., Stockdale, R. E., Taylor, P. L., Thomas, D. M., Turnbull, A. D., Wade, M. R., Wood, R., & Whyte, D. (1996). Higher fusion power gain with current and pressure profile control in strongly shaped diii-d tokamak plasmas. Physical Review Letters, 77, 2714–2717.

[66] Lazerson, S. A., Otte, M., Bozhenkov, S., Biedermann, C., Pedersen, T. S., & the W7-X Team (2016). First measurements of error fields on w7-x using flux surface mapping. Nuclear Fusion, 56(10), 106005.

[67] Lee, D., Harris, J., Hirshman, S., & Neilson, G. (1988). Optimum fourier representations for stellarator magnetic flux surfaces. Nuclear Fusion, 28(8), 1351.

[68] Loizu, J., Hudson, S., Bhattacharjee, A., & Helander, P. (2015a). Magnetic islands and singular currents at rational surfaces in three-dimensional magnetohydrodynamic equilibria. Physics of Plasmas, 22(2), 022501.

[69] Loizu, J., Hudson, S. R., Bhattacharjee, A., Lazerson, S., & Helander, P. (2015b). Existence of three-dimensional ideal-magnetohydrodynamic equilibria with current sheets. Physics of Plasmas, 22(9), 090704.

[70] Maaßberg, H., Romé, M., Erckmann, V., Geiger, J., Laqua, H. P., Marushchenko, N. B., & the W7-AS Team (2005). Electron cyclotron current drive in the Wendelstein 7-AS stellarator. Plasma Physics and Controlled Fusion, 47(8), 1137.

[71] Marushchenko, N., Turkin, Y., & Maaßberg, H. (2014). Ray-tracing code TRAVIS for ECR heating, EC current drive and ECE diagnostic. Computer Physics Communications, 185(1), 165–176.

[72] Marushchenko, N. B., Beidler, C. D., Erckmann, V., Geiger, J., Helander, P., Laqua, H., Maaßberg, H., & Turkin, Y. (2012). ECRH and ECCD scenarios for W7-X. EPJ Web of Conferences, 32, 01004.

[73] Matsuda, S. & Yoshikawa, M. (1975). Magnetic island formation due to error field in the jft-2 tokamak. Japanese Journal of Applied Physics, 14(1), 87.

[74] Moses, E. & the NIC Collaborators (2013). The national ignition campaign: status and progress. Nuclear Fusion, 53(10), 104020.

[75] Mueller, I. & Ruggeri, T. (1998). Rational extended thermodynamics. New York, U.S.A.: Springer-Verlag New York.

[76] Nührenberg, J. & Zille, R. (1988). Quasi-helically symmetric toroidal stellarators. Physics Letters A, 129(2), 113–117.

[77] Ongena, J. & Ogawa, Y. (2016). Nuclear fusion: Status report and future prospects. Energy Policy, 96, 770–778.

[78] Oreskes, N. (2004). The scientific consensus on climate change. Science, 306(5702), 1686–1686.

[79] Peacock, A., Greuner, H., Hurd, F., Kißlinger, J., König, R., Mendelevitch, B., Stadler, R., Schauer, F., Tivey, R., Tretter, J., von Sehren, C., & Ye, M. (2009). Progress in the design and development of a test divertor unit (TDU) for the start of W7-X operation. Fusion Engineering and Design, 84(7-11), 1475–1478. Proceeding of the 25th Symposium on Fusion Technology(SOFT-25).

[80] Peraza-Rodriguez, H., Reynolds-Barredo, J. M., Sanchez, R., Geiger, J., & Tribaldos, V. (2017a). Bootstrap current control studies in the Wendelstein 7-X stellarator using the free-plasma-boundary version of the SIESTA MHD equilibrium code. Plasma Physics and Controlled Fusion, Submitted.

[81] Peraza-Rodriguez, H., Reynolds-Barredo, J. M., Sanchez, R., Geiger, J., Tribaldos, V., Hirshman, S. P., & Cianciosa, M. (2017b). Extension of the SIESTA MHD equilibrium code to free-plasma-boundary problems. Physics of Plasmas, 24(8), 082516.

[82] Qu, Q. (1995). A new theoretical model for fast sawtooth collapse. Nuclear Fusion, 35(8), 1012.

[83] Reiman, A. & Boozer, A. H. (1984). Island formation and destruction of flux surfaces in three-dimensional MHD equilibria. The Physics of Fluids, 27(10), 2446–2454.

[84] Reiman, A. & Greenside, H. (1986). Calculation of three-dimensional MHD equilibria with islands and stochastic regions. Computer Physics Communications, 43(1), 157–167.

[85] Reiman, A. & Greenside, H. (1990). Computation of zero-beta 3-dimensional equilibria with magnetic islands. Journal of Computational Physics, 87(2), 349–365.

[86] Renner, H., Boscary, J., Greuner, H., Grote, H., Hoffmann, F. W., Kißlinger, J., Strumberger, E., & Mendelevitch, B. (2002). Divertor concept for the W7-X stellarator and mode of operation. Plasma Physics and Controlled Fusion, 44(6), 1005.

[87] Shafranov, V. & Zakharov, L. (1972). Use of the virtual-casing principle in calculating the containing magnetic field in toroidal plasma systems. Nuclear Fusion, 12(5), 599.

[88] Spong, D., Hirshman, S., Lyon, J., Berry, L., & Strickler, D. (2005). Recent advances in quasi-poloidal stellarator physics issues. Nuclear Fusion, 45(8), 918.

[89] Stadler, R., Vorköper, A., Boscary, J., Cardella, A., Hurd, F., Li, C., Mendelevitch, B., Peacock, A., & Pirsch, H. (2009). The in-vessel components of the experiment Wendelstein

7-X. Fusion Engineering and Design, 84(2), 305–308. Proceeding of the 25th Symposium on Fusion Technology.

[90] Stocker, T. F., Qin, D., Plattner, G.-K., Tignor, M., Allen, S. K., Boschung, J., Nauels, A., Xia, Y., Bex, V., & Midgley, P. M. (2013). IPCC, 2013: Climate Change 2013: The Physical Science Basis. Contribution of Working Group I to the Fifth Assessment Report of the Intergovernmental Panel on Climate Change. Cambridge, United Kingdom and New York, NY, USA: Cambridge University Press.

[91] Sunn Pedersen, T., Otte, M., Lazerson, S., Helander, P., Bozhenkov, S., Biedermann, C., Klinger, T., Wolf, R., Bosch, H., & The Wendelstein 7-X Team (2016). Confirmation of the topology of the Wendelstein 7-X magnetic field to better than 1:100,000. Nature Communications, 7, 13493.

[92] Suzuki, Y., Nakajima, N., Watanabe, K., Nakamura, Y., & Hayashi, T. (2006). Development and application of HINT2 to helical system plasmas. Nuclear Fusion, 46(11), L19.

[93] Suzuki, Y., Nakamura, Y., Kondo, K., Hayashi, T., Lloyd, S. S., & Gardner, H. J. (2003). MHD equilibrium of a low-shear helical axis heliotron. Plasma Physics and Controlled Fusion, 45(6), 971.

[94] Svensson, J. & Werner, A. (2007). Large scale bayesian data analysis for nuclear fusion experiments. In 2007 IEEE International Symposium on Intelligent Signal Processing (pp. 1–6).

[95] Terranova, D., Gobbin, M., Boozer, A. H., Hirshman, S. P., Marrelli, L., Pomphrey, N., & the RFX-Mod Team (2010). Self-organized helical equilibria in the RFX-Mod reversed field

pinch. Contributions to Plasma Physics, 50(8), 775–779.

[96] Tillack, M., Turnbull, A., Kessel, C., Asakura, N., Garofalo, A., Holland, C., Koch, F., Linsmeier, C., Lisgo, S., Maingi, R., Majeski, R., Menard, J., Najmabadi, F., Nygren, R., Rognlien, T., Ryutov, D., Stambaugh, R., Stangeby, P., & Stotler, D. (2013). Summary of the ARIES town meeting: Edge plasma physics and plasma material interactions in the fusion power plant regime. Nuclear Fusion, 53(2), 027003.

[97] Torrilhon, M. (2010). Hyperbolic moment equations in kinetic gas theory based on multivariate pearson-iv-distributions. Communications Computational Physics, 7, 639–673.

[98] Turkin, Y., Beidler, C. D., Maaßberg, H., Murakami, S., Tribaldos, V., & Wakasa, A. (2011). Neoclassical transport simulations for stellarators. Physics of Plasmas, 18(2), 022505.

[99] Turkin, Y., Maaßberg, H., Beidler, C., Geiger, J., & Marushchenko, N. (2014). Transport modelling of operational scenation in w7-x. 41st EPS Conference on Plasma Physics.

[100] van Rij, W. I. & Hirshman, S. P. (1989). Variational bounds for transport coefficients in three-dimensional toroidal plasmas. Physics of Fluids B: Plasma Physics, 1(3), 563–569.

[101] von Goeler, S., Stodiek, W., & Sauthoff, N. (1974). Studies of internal disruptions and $m = 1$ oscillations in tokamak discharges with soft□x-ray tecniques. Phys. Rev. Lett., 33, 1201–1203.

[102] Waelbroeck, F. (2009). Theory and observations of magnetic islands. Nuclear Fusion, 49(10), 104025.

[103] Waldrop, M. (2014). Plasma physics: The fusion upstarts. Nature, 511, 398–400.

[104] Wanner, M., Feist, J.-H., Renner, H., Sapper, J., Schauer, F., Schneider, H., Erckmann, V., & Niedermeyer, H. (2001). Design and construction of Wendelstein 7-X. Fusion Engineering and Design, 56-57, 155–162.

[105] Wilson, R. (1986). Chernobyl: Assessing the accident. Issues in Science and Technology, 3(1), 21–29.

[106] Zakharov, L. E., Galkin, S. A., Gerasimov, S. N., & contributors, J.-E. (2012). Understanding disruptions in tokamaks. Physics of Plasmas, 19(5), 055703.

This thesis was typeset using LaTeX, originally developed by Leslie Lamport and based on Donald Knuth's TeX. The body text is set in 11 point Egenolff-Berner Garamond, a revival of Claude Garamont's humanist typeface. A template that can be used to format a PhD dissertation with this look & feel has been released under the permissive AGPL license, and can be found online at github.com/suchow/Dissertate or from its lead author, Jordan Suchow, at suchow@post.harvard.edu.